

Wideband Propagation Channel in Vehicular Communication Scenarios

vorgelegt von
M.Sc. M.A.
Kim Mahler
geb. in Freiburg i.Br.

von der Fakultät IV – Elektrotechnik und Informatik
der Technischen Universität Berlin
zur Erlangung des akademischen Grades

Doktor der Ingenieurwissenschaften
- Dr.-Ing. –

genehmigte Dissertation

Promotionsausschuss:

Vorsitzender: Prof. Slawomir Stanczak

Gutachter: Prof. Giuseppe Caire

Gutachter: Prof. Claude Oestges

Gutachter: Prof. Fredrik Tufvesson

Gutachter: Priv.-Doz. Dr. techn. Thomas Zemen

Tag der wissenschaftlichen Aussprache: 10. Oktober 2016

Berlin 2016

Chairman

Prof. Slawomir Stanczak

Network Information Theory Group, Technical University of Berlin, Germany

Examiner

Prof. Giuseppe Caire

Communications and Information Theory Group, Technical University of Berlin, Germany
Viterbi School of Engineering, University of Southern California, USA

Prof. Claude Oestges

Institute of Information and Communication Technologies, Electronics and Applied
Mathematics, Ecole Polytechnique de Louvain, Belgium

Prof. Fredrik Tufvesson

Department of Electrical and Information Technology, Lund University, Sweden

Priv.-Doz. Dr. techn. Thomas Zemen

Digital Safety and Security Department, AIT Austrian Institute of Technology, Austria

Abstract

Future vehicles will be equipped with increasing computational capabilities and various vehicular sensors, enabling intelligent vehicles to perceive their surroundings in a better way. Vehicle-to-vehicle (V2V) communication is envisioned as a complementary sensor with remarkable potential for safety-related applications. The reliability of the wireless communication link is crucial and directly related to the radio channel. Hence, a detailed understanding of the dynamic V2V propagation process is fundamental for the development of a suitable communication system. This thesis introduces insights related to the V2V radio channel and the communication performance in different vehicular scenarios. The work is based on an extensive set of wideband (1 GHz) channel sounding measurement data at 5.7 GHz and corresponding parameter estimation methods. The estimation results reveal statistical distributions for relevant wideband multipath parameters of the dynamic V2V propagation process in eight communication scenarios. The intersection scenario is of particular interest for safety-related applications and the propagation therefore examined in detail. A categorization of urban intersections and three corresponding communication models are provided. In addition, a measurement-based ray tracing method is developed and applied, in order to estimate and model the locations of the scattering objects at intersections. The derived results are beneficial to realistic channel modeling approaches, in particular geometry-based stochastic channel modeling, and enhance developments towards highly reliable V2V communication systems.

Zusammenfassung

Zukünftig werden intelligente Fahrzeuge durch umfangreiche Sensorik und entsprechender Computerkapazität in der Lage sein ihre Umgebung umfassend wahrzunehmen. Die Fahrzeug-zu-Fahrzeug-Kommunikation erweitert maßgeblich diese Wahrnehmung und birgt für sicherheitsrelevante Anwendungen enorme Potenziale. Die hohe Zuverlässigkeit der drahtlosen Kommunikation ist dafür kritisch und hängt unmittelbar mit den Eigenschaften des Funkkanals zusammen. Eine sorgfältige Auseinandersetzung mit der dynamischen Funkausbreitung ist daher fundamental wichtig für die Entwicklung geeigneter Kommunikationssysteme. Diese Dissertation stellt Erkenntnisse zum Funkkanal und zu Leistungspotentialen der Fahrzeug-zu-Fahrzeug-Kommunikation in relevanten Verkehrssituationen vor. Die Ergebnisse der Arbeit basieren auf breitbandigen (1 GHz) Funkkanalmessdaten bei einer Trägerfrequenz von 5,7 GHz und geeigneten Parameterschätzverfahren. Die extrahierten Ergebnisse beschreiben statistisch den breitbandigen und dynamischen Mehrwegeausbreitungsprozesses in acht Kommunikationsszenarien. Das Kreuzungsszenario ist für sicherheitsrelevante Anwendungen von besonderer Bedeutung. Daher wird die entsprechende Mehrwegeausbreitung eingehend beleuchtet und drei Kreuzungskategorien mit entsprechenden Kommunikationsmodellen vorgestellt. Schließlich wird durch Anwendung eines auf Messdaten basierenden Raytracing-Verfahrens die Position der Streuer an Kreuzungen identifiziert und modelliert. Diese Ergebnisse dienen der Parametrisierung geometriebasierter, stochastischer Funkkanalmodelle und unterstützen damit die Entwicklung hochzuverlässiger Fahrzeug-zu-Fahrzeug-Kommunikationssysteme.

Acknowledgements

Research is based on the efforts of many and I would like express my thankfulness to those who made the completion of this work possible.

All results in this thesis are based on data from the HHI channel sounder and I therefore want to thank Wilhelm Keusgen, Andreas Kortke and Michael Peter for starting this project several years ago. In this sense, special thanks to Panagiotis Paschalidis and Mike Wisotzki for developing this measurement device and for the great collaboration on collecting the channel data. My deep thankfulness is dedicated to Fredrik Tufvesson and Thomas Zemen for mentoring me in this research field. Their advice in numerous discussions was of immense value for shaping and sharpening my research contributions. Im thankful to Giuseppe Caire for supporting me on this doctoral thesis and the collaborative supervision of several Masters thesis. I would like to thank Slawomir Stanczak for his trust and the conditions permitting the finalization of this work. I would like to express my gratitude to Claude Oestges for his interest and the examination of this thesis. Overall, I would like to thank all my colleagues for a delightful working environment and fruitful collaborations.

Thank you!

Preface

After my M.Sc. degree in telecommunications engineering from the Technical University of Berlin, I joined Heinrich Hertz Institute and started my research in a group working on the realization of advanced wireless communication systems and channel measurement devices. By that time, the HHI channel sounder was in a primary working stage and we started with first vehicle-to-vehicle channel measurements. Due to a limited experience on vehicular channels, I reached out to find experienced researchers in the field and was lucky enough to establish a collaboration agreement with leading experts in Lund and Vienna. This external expertise and the valuable data from the highly capable HHI channel sounder paved the way of the doctoral research I followed. My main scientific contributions are:

Paper I

K. Mahler; W. Keusgen; F. Tufvesson; T. Zemen; G. Caire., Propagation Channel in a Rural Overtaking Scenario with Large Obstructing Vehicles, Vehicular Technology Conference (VTC Spring), 2016 IEEE 83rd, Nanjing, China, 2016.

Paper I studies the propagation channel in a rural overtaking scenario with large obstructing vehicles, a scenario of special interest for collision avoidance applications. Currently available vehicular sensors are unable to detect this potentially hazardous situation, due to the fact that the opponent vehicle is hidden behind the overtaken vehicle and therefore out of sight. V2V communication is envisioned to cope with this problem by exchanging awareness messages and warn the driver in case of an emergency. However, the superior capability of a vehicular sensor is only achievable if the radio channel in this scarce scattering environment exhibits favorable properties. Mainly, the channel gain has to be sufficiently high for a faultless reception of the warning message. Radio waves in the 1 GHz frequency band might possibly be able to travel through large vehicles, but waves in the targeted 6 GHz band can only diffract or bounce around these obstacles. Different antenna positions on the communicating vehicle might mitigate this disadvantageous fact. A comparison to antennas mounted inside the vehicle assesses the communication potentials of aftermarket transceivers. The main contribution of this paper is an analysis of channel measurements relevant to this scenario with five different types of large obstructing vehicles. We investigate the difference of these antenna positions in terms of channel gain and also emphasize the difference

of the propagation condition between the so-called curved road scenario and the straight road scenario. The results provide an indication on achievable channel gains and connectivity ranges for a rural overtaking warning application under the given conditions.

Paper II

K. Mahler; W. Keusgen; F. Tufvesson; T. Zemen; G. Caire, "Propagation of Multipath Components at an Urban Intersection," Vehicular Technology Conference (VTC Fall), 2015 IEEE 82nd, Boston, MA, 2015.

A second highly relevant scenario for safety-related applications is the case where two vehicles are driving on collision course at an urban intersection. Again, conventional vehicular sensors fail to detect the approaching vehicle due to the fact that buildings are obstructing the line-of-sight. Different from the rural scattering environment, urban intersections provide a rich scattering environment and therefore possess a more complex multipath propagation with single-bounce or multiple-bounce reflections. Walls, traffic signs and other scattering objects contribute to the channel gain and enable the exchange of awareness messages under non-line-of-sight condition. Paper II describes the results of a manually conducted propagation analysis at a distance critical to a collision avoidance system. Based on this analysis, hypothesis of the corresponding scattering objects are estimated. The main contribution of this paper is an association of MPCs to scattering objects at an urban intersection. The high time resolution of our delay estimates in combination with an exact positioning system and additional tools allow a reliable identification and localization of scattering objects. Additionally, the number and lifetime of multipath components (MPC) are characterized, based on a tracking method described in Paper III.

Paper III

K. Mahler; W. Keusgen; F. Tufvesson; T. Zemen; G. Caire, "Tracking of Wideband Multipath Components in a Vehicular Communication Scenario," in IEEE Transactions on Vehicular Technology, in press.

Accurate and automated estimation of temporal behavior of individual MPCs is performed based on a wideband MPC tracking method. The non-stationarity of the V2V channel poses a challenge to a suitable tracking method, in particular the appearance and disappearance of MPCs within two adjacent measurement time instances. The tracking algorithm has to cope with certain difficulties, but can also take advantage of the wideband properties. One of the benefits from wideband channel data is the fact that the recorded channel is sparse, which eases the require-

ments on the tracking algorithm. In addition, highly resolved MPC experience only negligible small-scale fading effects, due to the fact that they rarely consist of multiple so-called physical MPCs. Paper III presents a tracking method adapted to the requirements and advantages of wideband V2V channel data. The algorithm balances the trade-off between a needed accuracy and an acceptable complexity level. The performance of the tracking method is extensively evaluated and set in a comparison to the performance of a state-of-the-art tracking algorithm developed for radar application. The main contribution of this paper is a demonstration that MPCs from wideband V2V channel measurement with a bandwidth of 1 GHz can be tracked with high estimation accuracy and low tracking losses.

Paper IV

K. Mahler; W. Keusgen; F. Tufvesson; T. Zemen; G. Caire, "Measurement-Based Analysis of Dynamic Multipath Propagation in Vehicular Communication Scenarios," submitted to IEEE Transactions on Vehicular Technology.

The wideband MPC tracking algorithm described in Paper III is a key instrument for extracting valuable information from channel measurement data. The application of this method to a large data set permits investigations of the temporal behavior of individual MPCs and a characterization of the most relevant MPC parameters in the V2V channel. Insights on the number of received MPCs and their delays are therefore essential for a statistical description of any wideband multipath channel. Due to its time-variant nature, the V2V wideband multipath channel has further distinctive characteristics. The movement of the Tx, Rx and the scattering objects yield for each wideband MPC a different Doppler frequency shift, due to different path angles with respect to the directions of the movement. In addition, the rich scattering environment in V2V channels in combination with the low antenna height lead to fast-shadowing phenomena. These dynamics lead to the appearance and disappearance of MPCs and the endurance of this appearance, the so-called MPC lifetime. Paper IV investigates the dynamic wideband MPC characteristics in eight V2V communication scenarios, i.e. the number of, birth rate and lifetime of individual MPCs. Statistical characterizations of MPC delay and Doppler observations are also given. The analysis is based on 72 measurement runs in eight different vehicular communication scenarios. The results of this paper provide wide insights into the vehicular propagation channel and are beneficial for various modeling approaches.

Paper V

K. Mahler; W. Keusgen; F. Tufvesson; T. Zemen; G. Caire, "Scatterer at Urban Intersections," to be submitted to IEEE Transactions on Vehicular Technology.

This paper investigates in detail the propagation process at urban intersections. A long-term MPC tracking method is applied and various information is estimated from the wideband MIMO MPC tracks. The delay characteristic of wideband MPC tracks give a good indication on the properties of the corresponding scattering object. In order to estimate the location of the scattering objects, a measurement-based ray tracing method is applied. This method requires an exact representation of the geometrical circumstances during the measurement run. The ray tracing results and the estimated MPC tracks allow for a semi-automated detection method, which is based on a comparison of delay, Doppler, path angle and delay characteristic. The main contribution of this paper is a parametrized model for the locations of relevant scattering objects, as part of a V2V geometry-based stochastic channel model at urban intersections.

Paper VI

K. Mahler; P. Paschalidis; A. Kortke; M. Peter; W. Keusgen, "Realistic IEEE 802.11p Transmission Simulations Based on Channel Sounder Measurement Data," Vehicular Technology Conference (VTC Fall), 2013 IEEE 78th, Las Vegas, NV, 2013.

The final two papers leave the field of V2V channel characterization and focus instead on the performance evaluation of IEEE 802.11p transceivers in selected V2V communication scenarios. The evaluation method is based on an IEEE 802.11p physical layer implementation in MATLAB and the replay of channel sounding measurement runs. The respective outcomes of these studies are V2V communication models, i.e. packet delivery rates (PDRs) as a function of distance. The derived results imply statistical validity, since the method rests upon different measurement sites per scenario and repeated measurement runs. Paper VI focusses on the highway oncoming traffic scenario, a situation where the radio channel experiences a very large Doppler frequency shift for the line-of-sight path. This scenario highlights the time-variant nature of V2V channel and is therefore suitable for investigations of the time-selective sensitivity of packet reception success. Particularly larger packets suffer from these time-selective fading effects, due to the fact that the channel estimation at the beginning of a packet becomes invalid for longer time periods and the equalization consequently erroneous. This effect is clearly shown in this paper and constitutes the main contribution of this publication. Paper VI also reveals an interesting phenomenon at distances around 200 m, where the combination of large Doppler shifts and multipath propagation lead to significant drops of the packet detection rate.

Paper VII

K. Mahler; P. Paschalidis; M. Wisotzki; A. Kortke; W. Keusgen, "Evaluation of Vehicular Communication Performance at Street Intersections," Vehicular Technology Conference (VTC Fall), 2014 IEEE 80th, Vancouver, BC, 2014.

The evaluation method described in Paper VI is now used for investigations of the V2V communication performance at urban intersections. As mentioned earlier, this scenario is highly relevant for a collision avoidance applications and V2V communication is the only vehicular sensor with the potential to cope with this situation. The substantial assessment of the V2V capabilities in this scenario requires a large sample of channel measurement data and an extensive study of the communication performance under non-line-of-sight condition. The main contribution of this paper are empirical V2V communication models with a two-dimensional distance dependency and three main categories of urban intersections. The established categorization is based on the respective V2V communication performance results. The developed models can be used for a realistic simulation of collision avoidance applications relying on V2V communication.

Research conducted within my group and collaborations with other research groups lead to further publications:

Paper VIII

K. Mahler, P. Paschalidis, A. Kortke and W. Keusgen, "Modeling and simulation of small-scale fading for vehicle-to-vehicle communication," Vehicular Networking Conference (VNC), 2010 IEEE, Jersey City, NJ, 2010.

Paper IX

P. Paschalidis; J. Nuckelt; K. Mahler; M. Peter; A. Kortke; M. Wisotzki; W. Keusgen; T. Kuerner, "Investigation of MPC correlation and angular characteristics in the vehicular urban intersection channel using channel sounding and ray-tracing," in IEEE Transactions on Vehicular Technology, 2015.

Paper X

K. Nagalapur; F. Braennstroem; E. Stroem; F. Undi; K. Mahler, "An 802.11p Cross-Layered Pilot Scheme for Time- and Frequency-Varying Channels and Its Hardware Implementation", IEEE Transactions of Vehicular Technology, Connected Vehicles Series, vol. 65, no. 6, pp. 3917-3928, June 2016.

Paper XI

P. Paschalidis, A. Kortke, K. Mahler, M. Peter, M. Wisotzki and W. Keusgen, "Wideband Car-to-Car MIMO Radio Channel Measurements at 5.7 GHz in Typical Communication Scenarios," Vehicular Technology Conference Fall (VTC 2009-Fall), 2009 IEEE 70th, Anchorage, AK, 2009.

Paper XII

P. Paschalidis; K. Mahler; A. Kortke; M. Peter; M. Wisotzki; W. Keusgen, "Statistical evaluation and modeling of the wideband Car-to-Car channel at 5.7 GHz," Electromagnetic Theory (EMTS), 2010 URSI International Symposium on, Berlin, 2010.

Paper XIII

P. Paschalidis; K. Mahler; A. Kortke; M. Peter; M. Wisotzki; W. Keusgen, "Pathloss and Multipath Power Decay of the Wideband Car-to-Car Channel at 5.7 GHz," Vehicular Technology Conference (VTC Spring), 2011 IEEE 73rd, Yokohama, 2011.

Paper XIV

P. Paschalidis; K. Mahler; A. Kortke; M. Wisotzki, "Investigation and simulation of Car2X communication for cooperative road safety systems", 8th International Workshop on Intelligent Transportation, WIT 2011. Hamburg, Germany, March 22nd - 23rd, 2011.

Paper XV

P. Paschalidis; K. Mahler; A. Kortke; M. Peter; M. Wisotzki; W. Keusgen, "2 X 2 MIMO Measurements of the Wideband Car-to-Car Channel at 5.7 GHz on Urban Street Intersections," 2011 IEEE, San Francisco, Vehicular Technology Conference (VTC Fall), CA, 2011.

Paper XVI

P. Paschalidis; K. Mahler; A. Kortke; M. Peter; M. Wisotzki; W. Keusgen, "Statistical Evaluation of Multipath Component Lifetime in the Car-to-Car Channel at Urban Street Intersections Based on Geometrical Tracking," 2012 IEEE 75th, Vehicular Technology Conference (VTC Spring), Yokohama, 2012.

Paper XVII

R. Protzmann; K. Mahler; K. Oltmann; I. Radusch, "Extending the V2X simulation environment VSimRTI with advanced communication models," ITS Telecommunications (ITST), 2012 12th International Conference on, Taipei, 2012.

Paper XVIII

L. Koschel; K. Mahler; R. Felbecker; M. Frey, "RF-MIMO for smart metering communication under harsh conditions," 2014 IEEE Conference on Wireless Sensors (ICWiSE), Subang, 2014.

Paper XIX

Z. Xu; L. Bernado; M. Gan; M. Hofer; T. Abbas; V. Shivaldova; K. Mahler; D. Smely; T. Zemen, "Relaying for IEEE 802.11p at road intersection using a vehicular non-stationary channel model," 2014 IEEE 6th International Symposium on Wireless Vehicular Communications (WiVeC), 14-15 Sept. 2014

Paper XX

H.-A. Nguyen; K. Mahler; M. Peter; W. Keusgen; T. Eichler; H. Mellein, "Estimation of DoA Based on Large-scale Virtual Array Data", 10th European Conference on Antennas and Propagation (EuCAP), 2016 Davos.

List of Acronyms and Abbreviations

BB	Baseband
CAM	Cooperative Awareness Message
CDF	Cumulative Density Function
CIR	Channel Impulse Response
CLK	Clock
DMC	Diffuse Multipath Components
DSRC	Dedicated Short Range Communication
ESPRIT	Estimation of Signal Parameters via Rotational Invariance Techniques
ETSI	European Telecommunications Standards Institute
FFT	Fast Fourier Transform
GNSS	Global Navigation Satellite System
H2I	Highway-to-Infrastructure
HCT	Highway Convoy Traffic
HHI	Heinrich Hertz Institute
HOT	Highway Oncoming Traffic
IEEE	Institute of Electrical and Electronics Engineers
ITS	Intelligent Transport Systems
KS	Kolmogorov-Smirnov
LO	Local Oscillator
LOS	Line-of-Sight

MIMO	Multiple-Input Multiple-Output
MPC	Multipath Component
MSE	Mean Square Error
MUSIC	Multiple Signal Classification
NLOS	Non Line-of-Sight
OSI	Open Systems Interconnection
OV	Obstructing Vehicle
PER	Packet Error Rate
PHY	Physical Layer
PDR	Packet Delivery Rate
QPSK	Quadrature Phase-Shift Keying
RCT	Rural Convoy Traffic
RF	Radio Frequency
ROT	Rural Oncoming Traffic
RMS	Root Mean Square
RSU	Roadside Unit
Rx	Receiver
SAGE	Space-Alternating Generalized Expectation and Maximization
SNR	Signal-to-Noise Ratio
SV	Scattering Vehicle
STDEV	Standard Deviation
TCT	Tunnel Convoy Traffic
TDL	Tapped Delay Line
Tx	Transmitter
UCT	Urban Convoy Traffic
UOT	Urban Oncoming Traffic
UWB	Ultra-Wideband
V2V	Vehicle-to-Vehicle
WSS	Wide-Sense Stationary
WSSUS	Wide-Sense Stationary Uncorrelated Scattering

Contents

Abstract	iii
Zusammenfassung	v
Acknowledgements	vii
Preface	ix
List of Acronyms and Abbreviations	xvii
1 Introduction	1
2 Vehicular Communications	3
3 V2V Propagation Channel	5
4 V2V Wideband Channel Measurements	11
5 From Wideband Channel Data to Channel Modeling	17
5.1 Tracking of Wideband MPC Behavior	17
5.2 Estimation of Scattering Objects	18
5.3 Channel Modeling Approaches	19
5.4 V2V Channel Modeling	20
6 Estimation and Tracking of Wideband MPC	23
6.1 Detecting MPCs in a Channel Impulse Response	23
6.2 Tracking of MPCs over Time	26
6.3 Evaluation Based on an Artificial Channel	30
6.4 Evaluation Based on Channel Measurement Data	33
6.5 Interconnecting MPC Tracks (Type 2)	39
6.6 Joining Discontinued MPC Tracks (Type 1)	45
7 Statistical Characterization of Wideband MPC in V2V Channels	49
7.1 Measurement Environments and Setup	50
7.2 MPC Parameter Extraction Methods	52
7.3 Extracted Parameters	54

7.4	Number of MPCs	56
7.5	MPC Birth Rate	57
7.6	MPC Lifetime	58
7.7	Excess Delay of Newborn MPCs	60
7.8	Relative Doppler frequency of Newborn MPCs	62
8	Scatterers at Urban Intersections	67
8.1	Manual Localization of Scatterers	68
8.1.1	Measurement Setup and Data	68
8.1.2	Results for Manual Localization of Scatterer	69
8.2	Semi-automated Localization of Scatterers	69
8.2.1	Wideband Delay Characteristics and Scatterer Properties . .	69
8.2.2	Measurement-based Ray Tracing	73
9	Evaluation of V2V Communications Performance	77
9.1	Performance Evaluation based on Channel Emulator	77
9.2	Performance Evaluation based on Matlab Software	80
9.2.1	IEEE 802.11p PHY in Matlab	80
9.2.2	Preprocessing of Channel Sounder Measurement Data	82
9.2.3	Communication Models for Highway Oncoming Traffic Scenario	82
10	V2V Communication Models at Urban Intersections	89
10.1	Transmission Simulation based on Channel Sounder Data	90
10.2	Communication Models	97
11	V2V Communication in a Rural Overtaking Scenario	101
11.1	Measurement Setup and Environment	102
11.2	Curved road scenario	102
11.3	Straight road scenario	105
11.4	Delay and Doppler spread	108
11.5	Potentials for V2V Communication	109
12	Conclusions	113
	Bibliography	115

1 Introduction

Recent wireless communications advancements induced a strong impact on our daily life. The omnipresent availability of information helps individuals to access information, navigate and communicate with other persons. For the next generation wireless network, the personal communication network will be enhanced with a communication network of intelligent objects. This future communication system will complement the infrastructure-based network and use direct machine-to-machine communication instead. Latest vehicles are equipped with increasing computer capacities and numerous ways of perceiving its environment with vehicular sensors, for instance radar, video or laser sensors. Vehicle-to-vehicle (V2V) communication is foreseen as an additional vehicular sensor with the unique potential to detect other vehicles or vulnerable road users, even without a line-of-sight (LOS) between the road users. This capability enhances the perception of intelligent vehicles significantly and enables remarkable possibilities for collision avoidance systems in dangerous traffic scenarios.

Exchanging cooperative awareness messages (CAMs) with valuable information, for instance with knowledge gathered from the various other vehicular sensors allows informed decisions for safety-related applications in Intelligent Transport Systems (ITS). An effective safety-related V2V communication system is dependent on highly reliable wireless communication links. The availability and performance of these communication links are in turn directly related to the properties of the propagation channel, which are essentially the received power and the fading effects of the radio channel. Hence, a detailed understanding of the V2V propagation process is fundamentally important for the development of a reliable V2V communication system. Radio channel measurements are at the starting point of this understanding, together with a subsequent analysis and characterization of unrevealed V2V propagation phenomena. Based on this knowledge, appropriate channel models and suitable communication performance evaluation methods can be developed. My thesis contributes to this research field.

2 Vehicular Communications

Motorola's 1972 MODAT mobile data radio system allowed users in vehicles to transmit data directly to and from dispatch computers, which could be used by public safety officers to enter license plate information during traffic stops [1]. While vehicular communications at that time referred to humans exchanging information, modern vehicular communications refers to the automated exchange of information between vehicles. The envisioned communication network will serve three main purposes: comfort, efficiency and safety. Comfort refers to infotainment systems and applications serving the personal needs of the passengers. Efficiency relates to solutions for a better usage of the current road traffic systems, which are needed due to the fact that we face a growing number of vehicles and a road network with limited space for growth [2]. For example, future cooperative vehicular communication system could be able to control traffic lights dependent on current vehicle densities. Finally, safety-related applications are envisioned to reduce the number of traffic accidents. Vision Zero is a multi-national project that aims to achieve a road traffic safety system with no fatalities or serious injuries [3]. The United Nations called for a "Decade of Action for Road Safety", in order to significantly reduce the road traffic fatalities by 2020 [4]. Since road traffic crashes are a leading cause of death globally, and the main cause of death among those aged 15 to 29 years [5], we should hope that suitable countermeasure technologies will be developed and that the success of these systems in the industrial world will eventually spread worldwide.

V2V communication will take a vital role in future collision avoidance systems, due to its unique capability as a vehicular sensor. Currently available sensors already enable sensor fusion systems to establish a comprehensive perception of the vehicles' surrounding. However, V2V radio communication will allow the vehicle to detect and communicate with other traffic participants, even if they are out of sight. This means that the vehicle can perceive much more than the driver is able to see, for instance during risky overtaking maneuvers on a rural road or for collision avoidance systems at urban intersections. Generally speaking, scenarios under non-line-of-sight (NLOS) conditions are the most relevant vehicular communication scenarios for safety-related applications and are therefore predominantly studied in this thesis.

The envisioned collision avoidance systems are often based on CAMs that are transmitted by each vehicle at a certain rate, for example 10 times per second [6]. These messages contain information about position, speed and traveling direction

of the transmitting vehicle and inform all receiving vehicles of the same. If the surrounding vehicles are able to decode the message correctly, possible collisions can be predicted and prevented. Clearly, the key features of a suitable safety-related V2V communication system are a high reliability of the communication link and a low latency of the information exchange.

Developments towards the 5G wireless network are application-oriented and based on diverse wireless technologies to better fulfill the user needs within specific application scenarios. There are mainly two alternatives being discussed on what technology V2V communication should be based on. The first alternative, a derivative of the 4G-LTE, is named LTE D2D (or LTE-V) and currently the most advanced V2V technology with the possibility to be further amended by future improvements. Despite these arguments, communication systems based on the second technology alternative called IEEE 802.11p are closer to market launch. The US Department of Transportation has stated in his 2016 report to US Congress that dedicated short-range communications (DSRC) for connected vehicle technologies is ready for deployment [7]. Many observers expect that the US administration will make this technology mandatory, which would boost the V2V launch dramatically.

IEEE 802.11p was released in 2010 as the standard for wireless access in vehicular communication [8] and is based on IEEE 802.11a, a standard also known as WLAN or Wi-Fi [9]. Only minor modifications have been carried out compared to the 11a standard and involve mainly the reduced channel spacing from 20 MHz to 10 MHz. This adjustment accounts for the longer excess delays and higher Doppler frequencies in a vehicular communication environments. IEEE 802.11p packet frames consist of a preamble part of 40 μ s duration and a data part that lasts between 88-2016 μ s (for a payload of 50-1500 Bytes respectively). The long training symbols in the preamble part are used by the receiver signal processing to estimate the current channel state and subsequently equalize the data part. IEEE 802.11 was originally developed for fixed or low mobility wireless communication, hence a scenario with very slow channel changes. Vehicular communication on the contrary is characterized by its time-variance and fast-changing channel states, which can lead to an invalid channel estimation and erroneous equalization of the data part. Channel tracking techniques are able to cope with this problem. Data-aided channel estimation for an IEEE 802.11p standard conform receiver can lead to a sensitivity difference of less than 1 dB in comparison to the sensitivity of a hypothetical benchmark receiver with perfect channel knowledge, as simulations show in [10]. Multiple-input multiple-output (MIMO) techniques are relevant in vehicular communications, due to the fact that a vehicle is very large compared to the wavelength of the carrier frequency and the consequence that different antenna positions on the vehicle lead to a large space diversity, which can be exploited to increase the reliability of the communication link. Promising techniques are the simple selection-combining scheme and the well-established maximum ratio combining scheme [11].

3 V2V Propagation Channel

Knowledge on the radio channel is a key instrument for the design and the development of a new wireless communication system. The term wireless "propagation channel" describes the physical propagation process of electromagnetic waves from the transmitter (Tx) antenna to the receiver (Rx) antenna. The term "radio channel" on the other hand is defined as the propagation channel in combination with the characteristics of the antenna radiation patterns (see Fig. 6.1 in [12]). The theoretical case of ideal isotropic antennas leads to equality between propagation and radio channel. Due to the fact that the channel measurement data was collected with the aim to have omni-directional antennas, we use the term "channel" synonymously to propagation channel.

Typically, the wireless propagation channel involves multipath and time-variance effects, as depicted in Fig. 3.1. Each multipath component (MPC) undergoes free-space attenuation and at least one of the multipath effects: transmission, reflection, diffraction or scattering. Movements of the objects in the scattering environment lead to continuous changes of the geometry and induce Doppler frequencies to each MPC. The Doppler frequency shift reflects the temporal change of the path length and depends on the relative speed of Tx, Rx and the (mobile or static) scatterers. For a scattered MPC, the total Doppler frequency shift is a summation of multiple Doppler shifts, due to multiple path changes. For instance, the Doppler frequency of Scatterer 1 in Fig. 3.1 amounts to

$$f_D = \frac{f_c}{c_0} (v_{Tx} \cos \alpha_{Tx} + v_{Rx} \cos \alpha_{Rx}), \quad (3.1)$$

where f_c is the carrier frequency, c_0 is the speed of light, (v_{Tx}, v_{Rx}) and $(\alpha_{Tx}, \alpha_{Rx})$ denote the speed and relative angle of Tx and Rx respectively.

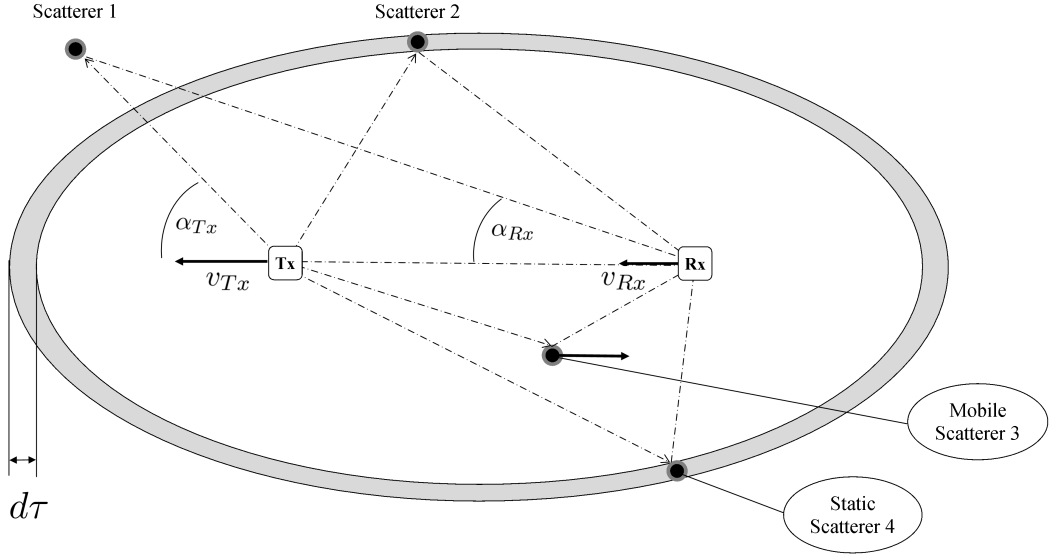


Figure 3.1: Schematic diagram of time-variant multipath propagation.

The power at the receiver antenna depends on the Tx-Rx-distance and additional fading effects, which are commonly separated into large-scale and small-scale. Large-scale fading is often modeled with the pathloss equation

$$PL(d) = \overline{PL}(d_0) + 10n \log \left(\frac{d}{d_0} \right) + X_\sigma, \quad (3.2)$$

where PL is the pathloss at distance d , n denotes the pathloss exponent dependent on the propagation environment and X_σ a Gaussian distribution modeling the (slow) shadowing effects from large objects [13].

The small-scale fading effect is due to constructive and destructive superposition of MPCs at the receiver antenna and leads to fluctuations of the signal envelope. The amplitude distribution of the superimposed signal is often modeled with a Rayleigh distribution for NLOS condition or with a Rician distribution for LOS conditions. These distributions are based on the central limit theorem and are therefore predominantly relevant for narrowband channels, where a sufficiently high number of MPCs can be found within a delay bin [14]. Larger bandwidths reduce the number of MPC per delay bin and lead to a different behavior of the signal envelope. A very high bandwidth can lead to a factual separation of the MPCs in the delay domain and result in a negligible small-scale fading. In Fig. 3.1, the width of the delay bin is represented by the ellipse width $d\tau$. Sufficiently large measurement bandwidths lead to slimmer ellipse widths and eventually to the resolution of scatterer 2 and 4 into separate ellipses.

When comparing V2V channels with the well-studied cellular channels, two main differences can be identified. The first difference is due to the lower antenna position of Tx and Rx antenna and the fact that both antennas are surrounded by scattering objects, which leads to an increased number of relevant scatterers. One model that accounts for this effect is the Double-Ring-Model [15]. Additionally, the low antenna positions in combination with impermeable objects add to the complexity of the multipath propagation with (short-term) MPC obstructions, which is often called fast-shadowing effect or mesoscale fading [16]. The low antenna position also leads to a stronger influence of ground reflection effects compared to cellular channels. The superposition of the ground reflections with the LOS path often leads to a power drop or a drop of the IEEE 802.11p packet success rate at distance of 200-300 m.

The second main difference is due to the movement of Tx, Rx and the scattering objects, which leads to a faster temporal fluctuation of the received signal. The vehicular channel is frequently labeled doubly-selective, since it contains severe frequency-selective fading due to the destructive superposition of strong MPCs and time-selective fading due to the Doppler frequency differences of these MPCs. These dynamics violate the wide-sense stationary (WSS) assumption and have to be incorporated into V2V channel models appropriately, for instance with smaller stationarity region of the channel statistics [17] [18].

The main principles of time-variant multipath propagation in vehicular scenarios are shown in Fig. 3.2. In addition to the LOS path, the Rx antenna receives reflections with two different time-variant effects. The first reflection at delay τ_2 experiences a Doppler frequency shift, due to the movement of Tx, Rx and the scattering vehicle (SV) driving in the opposite direction. Note that this Doppler shift is the sum of the Doppler shifts from the paths Tx-SV and SV-Rx, which explains why Doppler frequencies can be multiple times higher than one could expect based on the speed of one vehicle. The Doppler shift arises from the change of the path length over time and is therefore equivalent to the delay change over time. Reversely, the Doppler frequency of an MPC can be estimated from the delay change over time. Noteworthy, the assumption of a linear delay change as in Fig. 3.3 is only valid for a very short time period or for larger distances between the involved objects, where the negligible angle changes cause an approximately constant Doppler shift. The situation displayed in Fig. 3.2, where the SV passes by the Tx involves angle changes, hence a changing Doppler shift and yields a parabolic delay change.

The second time-variant effect in Fig. 3.2 is due to the instant obstruction of path 3 by the obstructing vehicle (OV), which leads to a path disappearance as displayed in Fig. 3.3. Although the effect of MPC appearance and disappearance is regularly called fast-shadowing, the real cause for the limited MPC lifetime is often not shadowing. Instead, a favorable geometrical constellation of the scattering environment typically determines the MPC lifetime, for instance a reflection on a

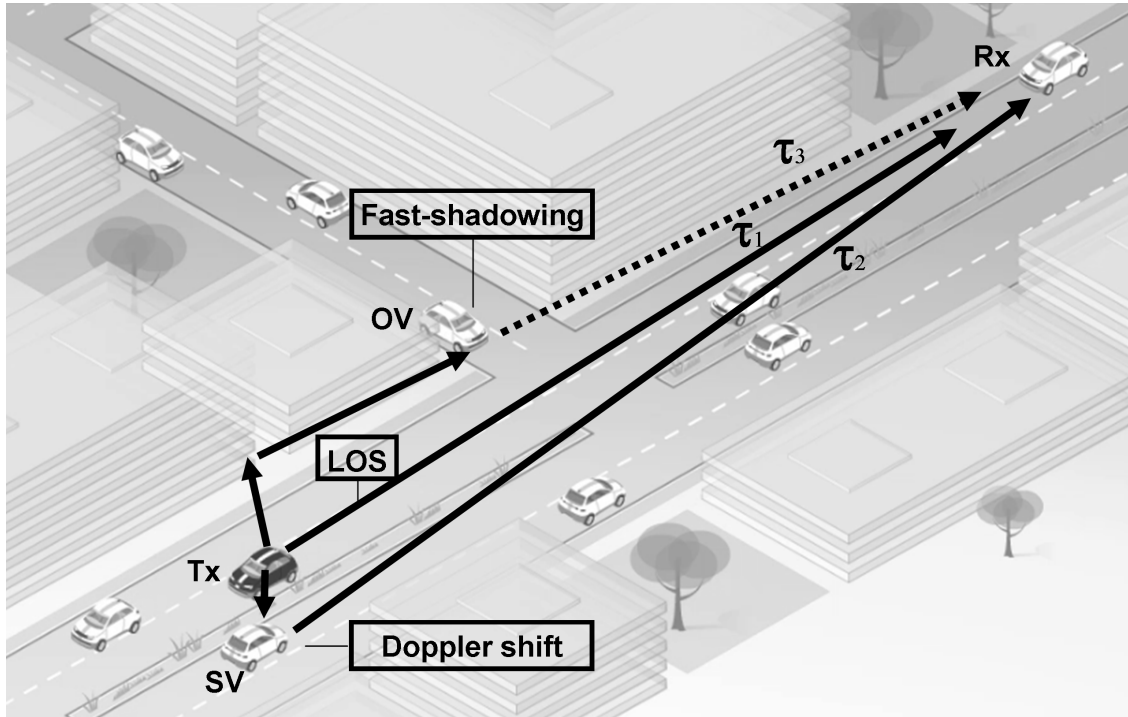


Figure 3.2: Time-variant multipath propagation in a vehicular environment.

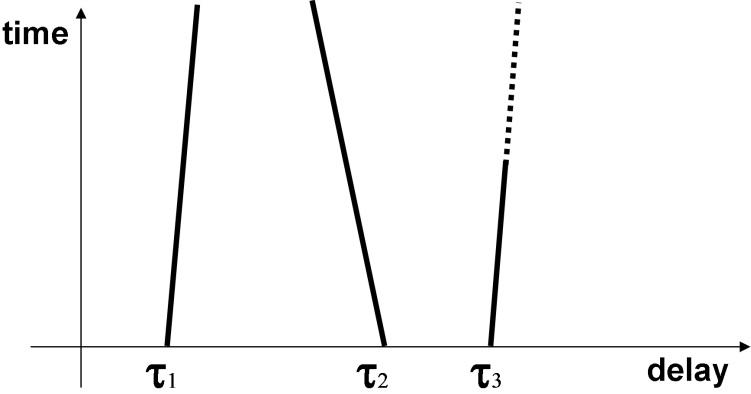


Figure 3.3: Change of delay over time and fast-shadowing of MPC.

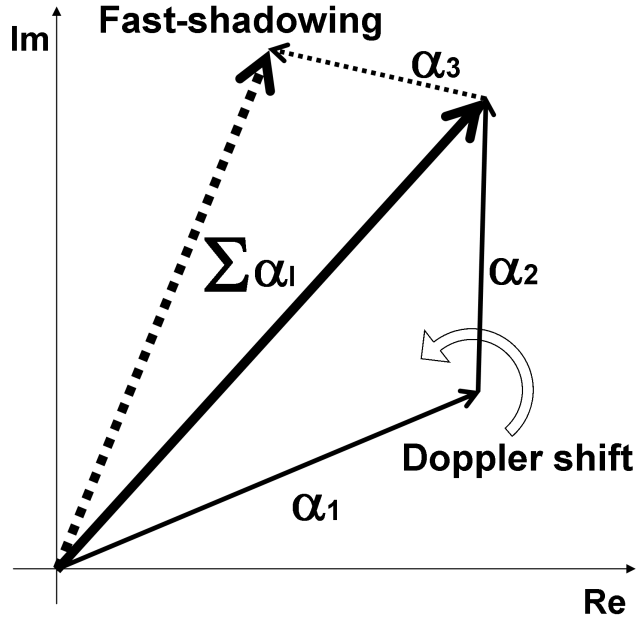


Figure 3.4: Superposition of time-variant multipath components at Rx antenna.

wall or a metallic surface.

Time-variant multipath propagation can also be regarded from the perspective of complex-valued MPC amplitudes α_1 , where the received multipath signal at the Rx antenna is a superposition of MPCs, as indicated in Fig. 3.4. In this perspective, the Doppler shift of path 2 is translated into a (faster) rotation of α_2 and leads to a destructive superposition effect on the received signal. Furthermore, the instant disappearance of α_3 leads to an immediate change of the overall signal.

The effects of the time-variant multipath channel are described by

$$h(t, \tau) = \sum_{k=1}^{P(t)} a_k(t) e^{j\varphi_k} w(\tau - \tau_k(t)), \quad (3.3)$$

where a_k is the amplitude, φ_k the phase, τ_k the delay of MPC k and $w(\tau)$ the isolated channel sounder pulse. $P(t)$ is the number of MPCs at time t .

Main properties of the channel are pathloss, shadowing, multipath propagation and Doppler frequency shifts. The first three properties are determined by the geometrical constellation of Tx, Rx and the surrounding environment, whereas the latter depends on the movement of the involved objects. Cars usually drive on streets and according to traffic rules within speed limits; geometry and movement are therefore well defined. In order to statistically examine and characterize the

vehicular channel, a categorization of the composite V2V communication into plausible communication scenarios is needed. A reasonable categorization is based on the different scattering environments, for example highway, intersection, urban or tunnel. The second dimension of a separation depends on the movement constellation and distinguishes for instance convoy traffic from oncoming traffic. In order to understand in detail the nature of propagation channels in different vehicular communication scenarios, appropriate wideband channel measurements have to be recorded, analyzed and characterized.

4 V2V Wideband Channel Measurements

Channel sounder devices measure the response of a propagation environment to a stimulating signal and are the sole method to quantify and eventually understand the propagation channel. In this context, the word "sounder" refers to the stimulation and sensing of the propagation environment by the measurement device. The output of a channel measurement is either a transfer function $H(f, t)$ in the frequency domain or a channel impulse response $h(\tau, t)$ in the time domain. Frequency-domain measurements are based on a multitone signal, for instance a chirp sequence. Time-domain measurements are based on transmitting pulses or pseudorandom sequences. This thesis is based on measurements conducted with the HHI channel sounder [19], a measurement device that operates in the time-domain with a pseudorandom sequence.

The principle functioning of the HHI channel sounder is depicted in Fig. 4.1. The sequence is generated and pulse-shaped with a D/A-converter in an arbitrary waveform generator (AWG) and then mixed with 5.7 GHz from the local oscillator (LO) from baseband (BB) to the radio frequency (RF). After interaction with the propagation environment and reception at the Rx antenna, the signal is filtered with a bandpass (BP) and sampled with an A/D-converter to retrieve the digital samples. Both parts of the system rely on highly accurate reference clocks (Clk), which are implemented based on a rubidium atomic clock. More details on the functioning of the HHI channel sounder can be found in [20].

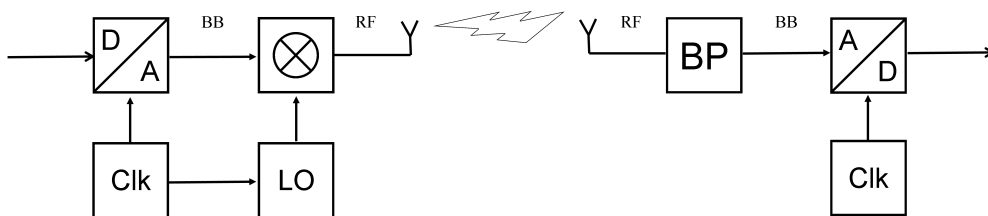


Figure 4.1: Principle functioning of the HHI channel sounder.

The pseudorandom transmit sequence has N elements and perfect periodic auto-correlation properties. The transmission time of the sequence is designed to be much smaller than the coherence time. The signal processing part of the Rx channel sounder correlates the received signal with the known sequence and obtains the channel impulse response at a certain time instance, the so-called snapshot. Recording of a time-variant channel requires an assumption on the largest occurring Doppler frequency value ν_{max} , in order to select the period between two adjacent snapshots in accordance with the Nyquist rate

$$f_{sample} \geq 2 \nu_{max}. \quad (4.1)$$

Also, the maximum excess delay has to be assumed, in order to prevent an echo overlap between adjacent snapshots. This leads to an upper bound of the snapshot period and, together with the lower bound from the Nyquist rate, has to be considered when selecting an appropriate snapshot period.

Groups of adjacent snapshots are named recording sets and capture the time-variant behavior of the channel. One measurement run with the HHI channel sounder consists of approximately 10,000 snapshots. In this thesis, two types of snapshot organizations are applied (see Table 4.1). The first kind of snapshot organization method called Type 1 is characterized by continuous recording up to a maximum recording set time of 1 s. There is a gap of around 100 ms between recording sets, which is needed for an adjustment of the automated gain control values. This snapshot organization allows for a full comprehension of the propagation process, but limits for an urban environment the total measurement time to around 7 s. The second snapshot organization alternative named Type 2 in Table 4.1 is a packet-oriented approach and is derived from the transmission timing of CAMs and the IEEE 802.11p packet length. Here, the set recording time is selected to be a little larger than the maximum packet on-air time and amounts to approximately 3 ms, with gaps of 10-100 ms between recording sets. This type of snapshot organization allows for longer measurement runs of up to 3 min and enables investigations of the long-term evolution of the channel. The snapshot organization is visualized in Fig. 4.2, containing the units: snapshot, set and recording.

Successful channel sounder campaigns for V2V communication scenarios require a careful selection of suitable measurement sites (see Section 7.1, 8.1.1, 10.1 and Chapter 11), an appropriate measurement timing setup (according to Table 4.1) and a synchronized coordination during the measurement execution. This measurement coordination is based on street maps and a detailed plan regarding the starting and terminal point for the measurement vehicles. A constant voice link between the drivers allows for the synchronization of the measurement run and permits instant adaptations to the current traffic situation.

Table 4.1: Organization of channel measurement into sets of snapshots.

	Type 1	Type 2
Snapshot recording time	16.3 μs	16.3 μs
Snapshot period	716 μs	200-716 μs
Number of snapshot per recording set	1397	6-13
Set recording time	999.5 ms	2.4-3.6 ms
Set period	1100 ms	10-100 ms
Number of sets per measurement	7	768-1666
Measurement duration	7.6 s	19.1-166.5 s

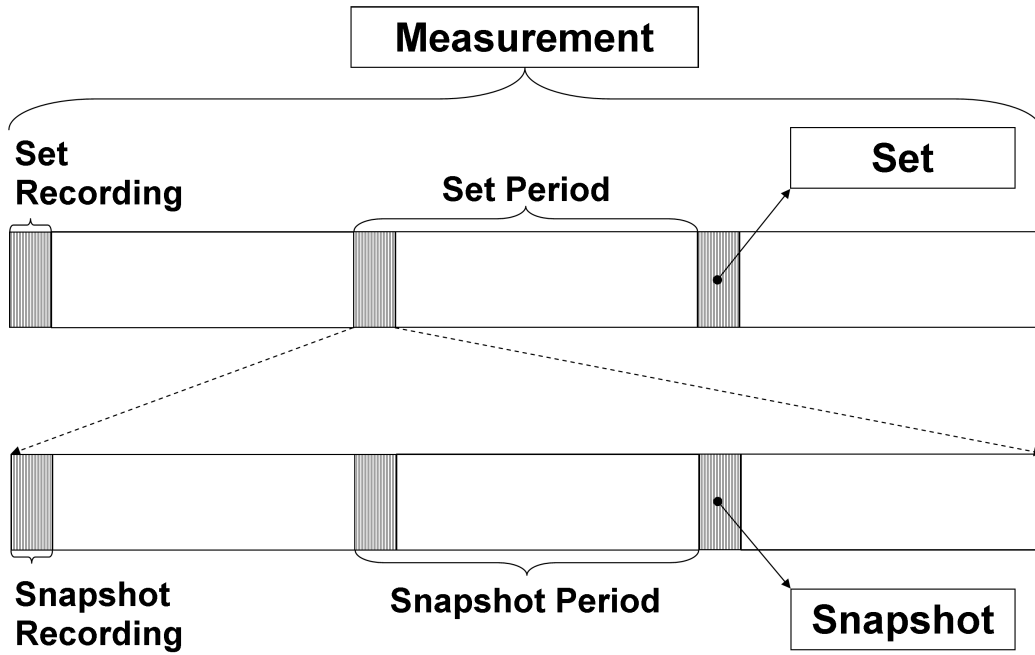


Figure 4.2: Organization of snapshots into recording sets.

Valuable measurement side information from video cameras and accurate positioning systems keep record of the environmental conditions during the run. We mounted in each vehicle a video camera facing towards the driving direction, the most relevant direction for V2V communication and its propagation channel. In order to capture all surrounding circumstances during the run, we mounted a 360° video camera on the roof of each vehicle. The positions of the measurement vehicles were recorded with a GeneSys ADMA-G device, a positioning system based on data fusion of GNSS positioning and data from inertial sensors. This positioning system is advantageous in tunnel scenarios or in deep street canyons, where coverage of GNSS satellites is reduced or absent.

The transmitter unit and receiver unit of the HHI channel sounder are shown in Fig. 4.3. The measurement device is installed in ordinary passenger vehicles and used in real traffic situations (Fig. 4.4). Simultaneously measured channels from antennas mounted at different positions on the roof of the vehicle permit investigations of exploiting antenna diversity in the range of several wavelengths, which is important for communication systems based on MIMO techniques. The antenna positions investigated in this thesis are depicted in Fig. 4.5: roof antennas and antennas inside the cabin. Channel investigations for antennas mounted inside the vehicle give an indication of the advantages and disadvantages of aftermarket transceivers, thus the installation of V2V communication systems in older vehicles.

Properties of the channel vary for different frequency bands and appropriate channel measurement should therefore be conducted at or close to the targeted communication frequency. The IEEE 802.11p standard operates at carrier frequencies of around 5.9 GHz and the HHI channel sounder was designed at a carrier frequency of 5.7 GHz. The corresponding measurement antennas are matched to the desired frequency range from 5.2 to 6.2 GHz and feature an approximately omnidirectional radiation pattern in the azimuth plane. This antenna characteristic probably differs slightly for the case that the antennas are mounted on a vehicle roof, but due to fact that the total length of the antenna is multiple wavelengths above the metallic roof surface, the deviation from the laboratory measurement is probably low.

The HHI channel sounder bandwidth of 1 GHz is 4-15 times larger than other V2V channel sounders [21] [22] and the most remarkable feature of this measurement device. The HHI channel sounder bandwidth leads to a multipath delay resolution of 1 ns and reveals reflections from scattering objects ranging in the size of 30 cm. This allows wide insight into the temporal behavior of individual MPCs and sets the fundamentals for a suitable wideband MPC tracking method. Furthermore, this feature enables the association of individual MPCs to physical objects in the surrounding scattering environment.



Figure 4.3: HHI channel sounder: receiver unit (left) and transmitter unit (right).



Figure 4.4: HHI channel sounder installed in measurement vehicles (left), placement of antennas on roof and at different locations inside the vehicle (right).

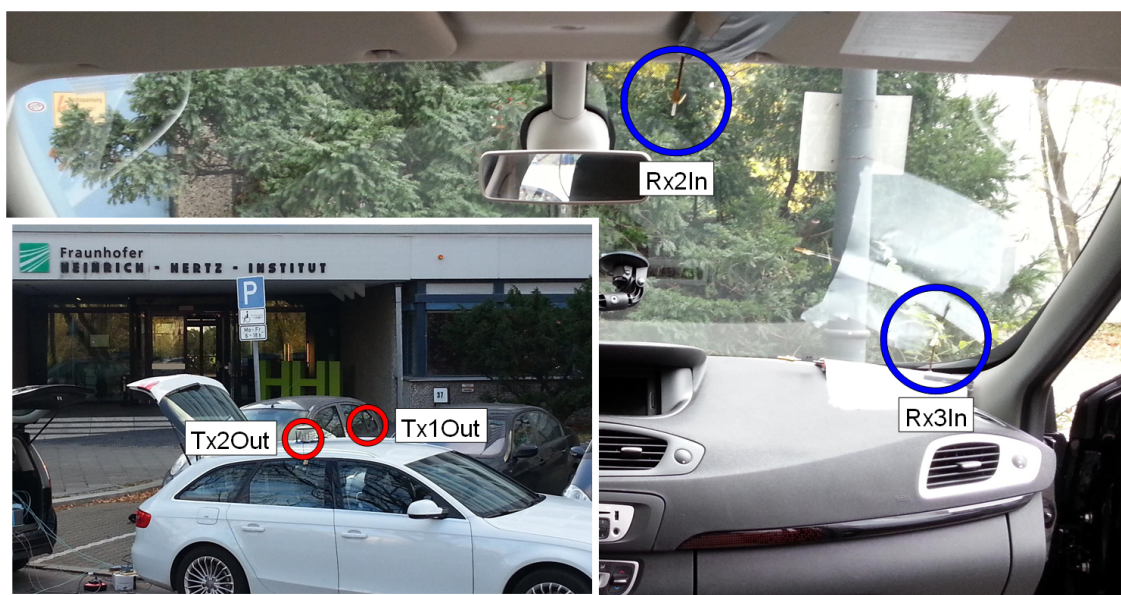


Figure 4.5: Position of antennas during measurement: two Tx and three Rx antennas (Rx1Out is in a similar position as Tx2Out).

5 From Wideband Channel Data to Channel Modeling

The design and development of a suitable wireless communication system for a new propagation environment or at a new frequency should be based on the fundamental understanding of the underlying propagation channel. This requires preceding research efforts, which can be partitioned into research steps as displayed in Fig. 5.1. This thesis examines multiple steps of this research chain for V2V communication. Extensive channel measurement data is collected and then processed with suitable parameter estimation methods, namely with several wideband MPC tracking algorithms and a measurement-based ray tracing method for localizing scattering objects. The next step covered by this thesis involves the analysis and statistical characterization of the estimation outcome, hence a modeling of individual channel parameters. Finally, numerous performance evaluation methods are discussed within this thesis. A comprehensive channel model or a communication system design are not scope of this thesis.

5.1 Tracking of Wideband MPC Behavior

In order to follow the temporal behavior of MPCs or extract other relevant channel parameters [18], complex estimation algorithms are required [23]. However, a sufficiently large channel measurement bandwidth leads to lower complexity requirements for a suitable MPC tracking algorithm. One of the reasons why a simpler tracking method can be applied if the delay time resolution is sufficiently fine, is due to the lower number of physical MPCs that make up a resolvable MPC [14] [24]. This means that there are fewer superimposed MPCs and hence a less

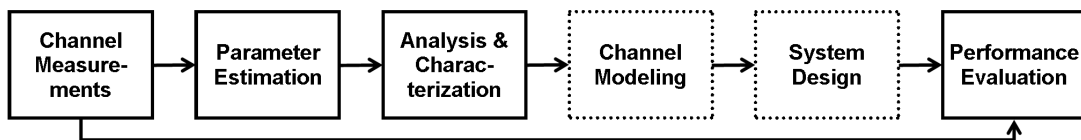


Figure 5.1: Research chain for a new wireless communication system.

severe amplitude fluctuation of the resolvable MPC. The absence of small-scale fading makes it significantly easier to follow the temporal evolution of resolvable MPCs. Furthermore, appropriate delay estimation techniques allow a sub-ns accuracy and make tracking of individual MPCs even easier. Another consequence from a large measurement bandwidth is the sparsity of the multipath channel. The high resolution clearly separates the MPCs and leads to a reduced interaction between neighboring MPCs, which again leads for a tracking method to a reduced likelihood of false positives. Another aspect that reduces the requirements for an MPC tracking algorithm is particularly related to V2V communication scenarios: vehicles drive predominantly in a very predictable manner, i.e. within clearly definable limits regarding their change of speed and change of direction. This means for the prediction of an MPC delay progression that a linear continuity assumption of the instantaneous delay progression is valid.

A distinctive characteristic of V2V communication channels is their time-variant behavior, due to the movement of transmitter, receiver and scattering objects. These dynamics lead to a smaller stationarity region of the channel statistics [18] and have to be incorporated in an appropriate manner. Our wideband channel data reveals appearing and disappearing MPCs from one snapshot to the next snapshot, hence non-stationary MPC behavior between adjacent snapshots. An appropriate tracking method has to be able to cope with this behavior. This is the reason why the tracking algorithm proposed in this thesis is not based on a local WSS time window as done in [25], but instead takes every snapshot as an independent processing step.

The outcome of comprehensive wideband MPC parameter estimation is the statistical characterization of number of, birth rate and lifetime of individual MPCs. Also, distributions for delay and Doppler frequency per wideband MPC can be obtained.

Although the proposed tracking algorithm performs well for short-term periods, additional tracking algorithms are needed in order to track MPCs over a longer period. Dependent on the organization of the snapshots and the corresponding length of the recording set as described above, different tracking method need to be applied.

5.2 Estimation of Scattering Objects

A benefit of wideband channel sounding measurements is the ability to detect individual MPCs and relate these to physical scattering objects. Information on wideband MPC tracks lead to further valuable channel information. Since measurements are recorded with two antennas mounted at the left and right edge of the roof, the path angle estimation principle with a two elements antenna array can be applied. The known distance between the roof antennas and the delay difference

detected at the antennas allow for an angle estimation. The functioning of this approach could be verified with an appropriate measurement constellation and the comparison of the delay difference in the measurement data to the expected delay difference, based on the antenna distances. Due to the fact that all antennas and RF-chains are essentially identical and the angle estimation involves the difference in delay only (MPC phase is ignored), this approach does not require an antenna array calibration.

A detailed understanding of wideband MPC dynamics facilitates also the potential to associate measured paths to corresponding scattering objects. This can be accomplished by applying the so-called measurement-based ray tracing method, which relates measured MPC estimates to rays from a ray tracing simulation of the real-world measurement run. The results from this scattering location method reveal the geometrical causation of the V2V multipath propagation process and can be used to enhance the development of geometry-based channel models.

5.3 Channel Modeling Approaches

Channel modeling pursues the establishment of an efficient and accurate channel representation. An appropriate channel model enables realistic simulations of the propagation process. The appropriateness of the model depends on the purpose of the simulation and is a balanced trade-off between accuracy and simplicity. The channel model should reflect the most relevant characteristics accurately and be simple enough to make an implementation as software simulation or within a channel emulator feasible. Physical channel modeling approaches can be roughly separated into deterministic, stochastic and hybrids involving both approaches.

Deterministic channel models aim for the exact reproduction of all relevant MPC and require demanding computational efforts. Ray tracing is a common deterministic modeling approach [26] [27], where transmitted rays interact with physical objects in a geometrical model and are then superimposed at the Rx antenna. This method can be useful for an evaluation of appropriate vehicle antenna positions or for propagation simulations at sites of particular interest, for instance at an urban intersection. Another deterministic method is based on replaying previously recorded channel data. The main advantage of this method is its high accuracy. Drawbacks of this method are the large amount of data required for simulations and a possibly narrow validity, if the focus remains on single measurement runs. Nevertheless, this method is a reasonable complement to stochastic channel models, since it covers particularly demanding channels not covered by the statistics.

Stochastic modeling approaches are based on the statistical distributions of channel parameters and usually more practicable. Stochastic models can be differentiated into wideband and narrowband: wideband models regard each MPC individually, whereas narrowband approaches essentially model the superimposed MPCs

within a delay bin. A common assumption in stochastic channel modeling is wide-sense stationarity uncorrelated scattering (WSSUS), which is a precondition of the simple and widely used tapped delay line (TDL) model. Wide-sense stationarity means that the channel statistics do not change over time, which implies that the Doppler frequencies remain constant. WSSUS does not hold in vehicular communication scenarios [18] and V2V modeling approaches have to incorporate this particular characteristic.

5.4 V2V Channel Modeling

Probably the two most distinctive characteristics of V2V channels are the low mounting height of both (Tx and Rx) antennas and the time-variant behavior, due to the movement of transmitter, receiver and scattering objects. These characteristics lead to, among others, fast MPC shadowing effects and diverse Doppler frequency distributions [18]. Hence, classical TDL models are enhanced with a "persistence process" [28] or with varying Doppler spectra models [29]. Different from these models, [25] proposes a dynamic wideband V2V channel model based on a local WSS time window and MPC statistics related to this time window.

Alternatively to deterministic and stochastic modeling, the geometry-based stochastic channel models (GSCM) follow a hybrid modeling approach based on statistical distributions of scattering objects and a simplified deterministic propagation simulation. The scatterers are distributed in a realistic and physically reasonable manner, which can only be accomplished if the scattering geometry is not arbitrary but predictable to some extent. This can be achieved in V2V communication scenarios. An important advantage of the GSCM method is the fact that the directional MPC information, i.e. angle-of-arrival (AOA) and angle-of-departure (AOD), are included in the channel model. This makes it possible to separate the propagation channel from the radio channel, which allows the inclusion of different antenna characteristic and enables realistic studies on directional antennas or other MIMO techniques (see [12] for details on directional channels). In general, the AOA and AOD in V2V channels are time-variant, which lead to time-variant Doppler frequencies and make the GSCM approach well-suited for non-stationary propagation environments.

An overview of current V2V channel modeling can be found in [30] [31]. Basically there are two major paths being followed: extensions and derivatives of the TDL model and, the GSCM. An interesting comparison of these two approaches can be found in [32]. Probably the most prominent TDL model was released by ETSI, where each communication scenarios is represented by a channel impulse response of 3-4 tap, with each tap being characterized by its power, delay and Doppler frequency. In order to cope with the fast MPC shadowing effects, other approaches enhance the classical TDL model with a so-called persistence process [28]. Different

from these narrowband approaches, work in [25] proposes a dynamic wideband V2V channel model, with a local WSS time window. Examples for work on V2V GSCM can be found in [33] [34], related work also in [35] [36].

6 Estimation and Tracking of Wideband MPC

6.1 Detecting MPCs in a Channel Impulse Response

Processing of channel sounder data is a multi-step process and starts with the detection of MPCs in the channel impulse response at a certain time instance. Superresolution channel parameter estimation schemes such as ESPRIT [37] and MUSIC [38] require a covariance matrix, hence multiple observations of a stationary process. Since the fading process of vehicular channels is non-stationary, [25] and [18] suggest to use a local WSS time window. Instead, we decided to use the smallest possible time window and take every measurement snapshot as an independent process step. This approach is reasonable for our wideband channel measurement data, since we observe non-stationary MPC behavior between snapshots, e.g. appearing/disappearing MPCs and a change of the MPC delay. Since our tracking method does not depend on any statistics and we are not aiming at any statistical channel parameters based on a local stationarity region, we disregard matters on appropriate stationarity window lengths.

We use a MPC detection algorithm that is based on work from [39], which has some similarities to the CLEAN [40] or UWB-SAGE [41] algorithms and can be summarized as follows: Find the strongest peak in the channel impulse response, subtract this dominant peak in the frequency domain and continue searching and subtracting strongest peaks respectively in the remaining impulse response. A detailed description of this search and subtract algorithm can be found in [42], an experimental verification of this algorithm is given in [39]. Here, we start with the time-variant channel impulse response as

$$h(t, \tau) = \sum_{l=1}^L \alpha_l(t) \delta(\tau - \tau_l(t)), \quad (6.1)$$

where L denotes the number of scatterers, α_l the complex gain and τ_l the delay of MPC l . The channel impulse response provided from a channel sounder with

measurement bandwidth B can be expressed as

$$h(t, \tau) = \sum_{l=1}^L \alpha_l(t) w(\tau - \tau_l(t)), \quad (6.2)$$

where $w(\tau)$ is the isolated pulse with duration T_p . The sampled channel data depends on the snapshot sampling period T_s and the delay resolution period $T_b = 1/B$. We therefore express the discretized form of the channel impulse response as

$$h(nT_s, uT_b) = \sum_{l=1}^L \alpha_l(nT_s) w(uT_b - \tau_l(nT_s)), \quad (6.3)$$

for $n = \{1, \dots, M\}$ and $u = \{1, \dots, U\}$, where M is the maximum number of available snapshots and U is the selected sounding sequence length (denoted N in [19]). As previously stated, we want to detect the MPCs at each single snapshot n and therefore define a channel impulse response as vector $\mathbf{h} \in \mathbb{C}^U$ with elements

$$h_u = h(uT_b) = \sum_{l=1}^L \alpha_l w(uT_b - \tau_l). \quad (6.4)$$

We furthermore define vector

$$\mathbf{w}(\tau) = [\mathbf{0}_{D_\tau}, \mathbf{w}_0, \mathbf{0}_{U-Z-D_\tau}]^T \in \mathbb{R}^U, \quad (6.5)$$

with D_τ being the discretized version of time delay τ , such that $\tau \simeq D_\tau \cdot T_b$ and with $\mathbf{w}_0 \in \mathbb{R}^Z$ of elements $w_u = w(uT_b)$, $u = \{1, \dots, Z\}$ such that $T_p = Z \cdot T_b$. The zero series $\mathbf{0}_{D_\tau}$ and $\mathbf{0}_{U-Z-D_\tau}$ consist of D_τ and $U - Z - D_\tau$ zero elements respectively and are used to shift \mathbf{w}_0 in $\mathbf{w}(\tau)$. Since we are using sparse wideband channel data, we assume that the delay components τ_l are separable, that is,

$$|\tau_i - \tau_j| \geq T_b \quad \forall i \neq j \quad (6.6)$$

and can therefore apply the maximum likelihood method to obtain the delay and complex amplitude estimates of the strongest peak [42]:

$$\hat{\tau}_l = \underset{\tau}{\operatorname{argmax}} |\mathbf{w}(\tau)^T \mathbf{h}_l|, \quad (6.7)$$

$$\hat{\alpha}_l = \frac{\mathbf{w}(\hat{\tau}_l)^T \mathbf{h}_l}{\mathbf{w}^T \mathbf{w}}, \quad (6.8)$$

where \mathbf{h}_l is the channel impulse response after l strongest peak detections. The strongest MPC is subtracted from the channel impulse response in the following way

$$\mathbf{h}_l = \begin{cases} \mathbf{h} & , l = 1 \\ \mathbf{h}_{l-1} - \hat{\alpha}_{l-1} \mathbf{w}^*(\hat{\tau}_{l-1}) & , l > 1, \end{cases} \quad (6.9)$$

the detected MPC $\theta_l = \{a_l, \tau_l\}$ is saved for further processing and the algorithm searches for the next strongest peak.

We augment the algorithm by windowing the measured transfer function before applying the detection algorithm. The windowing reduces the side lobes of the pulses in the channel impulse response and improves the overall detection performance. In order to select the best windowing method, the performance evaluation was executed for a Raised-Cosine roll-off window and a Kaiser window [43] with different corresponding window parameters. The shape of the Kaiser window in the frequency domain

$$z[u] = \begin{cases} \frac{I_0(\pi a \sqrt{1 - (\frac{2u}{U-1} - 1)^2})}{I_0(\pi a)}, & 0 \leq u \leq U - 1 \\ 0 & \text{otherwise,} \end{cases} \quad (6.10)$$

and therefore the trade-off between the width and the side lobes of the pulse is determined only by one parameter a . In (6.10), I_0 is the zeroth order of the modified Bessel function of the first kind, U is the window length (equal to the sounding sequence length) and a a non-negative real number. The best results showed the Kaiser window with a parameter value of $a = 6$.

After the subtraction of a peak, a delay range around the identified peak location is blocked for the following peak searches, with the purpose to prevent a re-detection at neighboring delay values. We set the width of this blocked delay range equal to the channel sounder pulse width at 10 dB below its peak magnitude, which is in our case 2.47 ns. The entire detection process for a channel impulse response involves the following steps:

1. Estimate the noise floor by estimating the power of a channel impulse response part where no MPCs occur (usually at larger delays), add 6 dB to obtain a noise floor threshold and set all values in the impulse response below this threshold to zero.
2. Apply windowing in the frequency domain using a Kaiser window with a parameter value of 6 (see (6.10) for the corresponding equation and [43] for more details).
3. Find the strongest peak outside blocked delay range(s) and save as a detected MPC.
4. Block the delay range surrounding the newly detected MPC.
5. Subtract the channel sounder pulse at the detected MPC delay position from the measured transfer function, as done in (6.9).
6. Repeat points 3 to 5 until no additional MPCs are detected.

Table 6.1: Parameters of the GM-PHD filter implementation used for tracking performance comparison

Symbol	Value	Explanation
σ_ν	$3 \cdot 10^{-1}$	Standard deviation of process noise in $\frac{m}{s^2}$
σ_ε	$3 \cdot 10^{-3}$	Standard deviation of measurement noise in m
p_S	0.99	Probability of target survival, see (19) in [44]
p_D	0.95	Probability of target detection, see (20) in [44]
T	$1 \cdot 10^{-2}$	Truncation threshold, see Table II in [44]
U	$1 \cdot 10^{-1}$	Merge threshold, see Table II in [44]
–	$2 \cdot 10^{-1}$	Minimum weight threshold, see Table III in [44]

6.2 Tracking of MPCs over Time

The large measurement bandwidth of 1 GHz makes MPC tracking of individual MPCs feasible. The goal of our MPC tracking method is to keep the algorithm complexity as low as possible and yet establish an effective tool with a good tracking performance. In order to evaluate our algorithm, we compare performance indicators with a state-of-the-art tracking algorithm called Gaussian mixture probability hypothesis density (GM-PHD) filter [44], which incorporates the widely used extended Kalman filter [45]. The GM-PHD filter is a recursive algorithm that models targets as random finite sets and propagates the posterior intensity in time. The implementation of this tracking approach is elaborate, requires substantial computational efforts and an adaption of least 10 algorithm parameters to the corresponding tracking problem. This includes seven core algorithm parameters and additional parameters with lower effect on the tracking results. In our implementation, we use three additional parameters for creating the so-called birth processes and four additional parameters to filter out tracks with unlikely delay/magnitude changes (similar to our maximum delay/magnitude change thresholds in (6.15)). In Table I we list the most relevant algorithm parameters matched to our measurement data.

Our proposed algorithm works with little computational effort and is based on the continuity of the delay and magnitude changes. Although proposed as a method for MPC tracking in [46], the phase change estimates are not used for tracking due to their high measurement noise and their 2π -ambiguity. Our algorithm is based on four parameters, which are estimated depending on the measurement data setup and quality as for (6.23) or directly from the underlying physical model as for (6.15).

The developed MPC tracking algorithm is based on the following assumptions:

1. The same MPC is detected in three consecutive snapshots.
2. Splitting or combining of MPC tracks does not occur.
3. The second derivatives of delay and magnitude are below the estimated maximum search tolerances in (6.23).

The main idea behind our MPC tracking approach is similar to the tracking approach described in [33], but in addition to delay estimates we also use magnitude estimates as a measure for tracking. The MPC tracking steps are depicted in Fig. 6.1 and can be summarized as follows:

1. Start in the first snapshot with the strongest peak and search in the second snapshot for neighboring peaks in terms of delay and magnitude distance to the starting peak.
2. Use the observed delay change and magnitude change (dotted lines in step 1 in Fig. 6.1) to predict the peak location in the third snapshot, as shown in step 2 in Fig. 6.1. Based on the predicted location and the pre-defined search tolerances, define a two-dimensional search range (brackets in step 2 in Fig. 6.1). If a peak is found within the search ranges, a MPC track has been identified.
3. In case more than one peak is found within the defined search ranges, choose the peak with smallest distance to the predicted delay location.
4. Use the latest delay change and magnitude change to get the next search ranges accordingly (step 3 in Fig. 6.1). Continue searching peaks along the MPC track, until no peak within the current search ranges is found.
5. Start with the second strongest peak in the first snapshot until the MPC track ends. Only consider peaks that are not yet linked to a MPC track.
6. Continue searching tracks for all other peaks in the first snapshot and then continue searching for tracks in later snapshots that are not yet linked to a MPC track.

Stating the MPC tracking algorithm with mathematical expressions, we have to keep in mind that $h(nT_s, uT_b) = h[n, u]$, with T_s being the channel acquisition period and T_b being the delay resolution. The output from the detection algorithm at time instance n are the MPC gain a_l , the delay τ_l and the phase ϕ_l

$$\theta_l = \{a_l, \tau_l, \phi_l\} \quad (6.11)$$

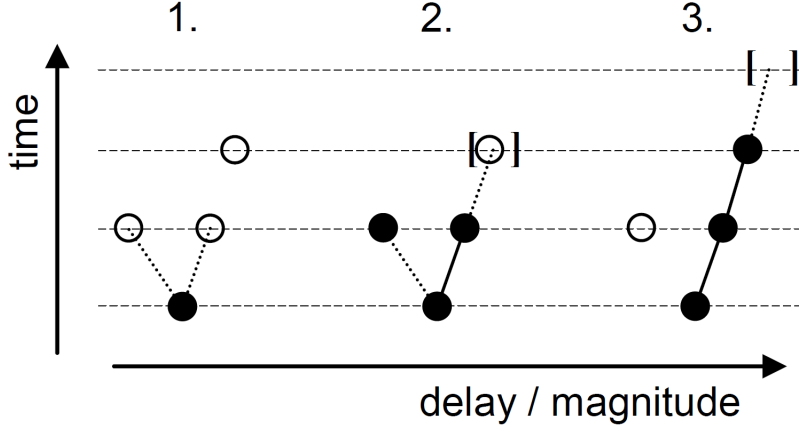


Figure 6.1: Schematic diagram of the MPC tracking steps.

with $l \in \{1 \dots L_n\}$ and L_n being the number of detected MPCs at time n . For the MPC tracking algorithm, we use a subset of the estimated parameters

$$\mathbf{s}_l[n] = \begin{pmatrix} a_l[n] \\ \tau_l[n] \end{pmatrix}. \quad (6.12)$$

We start in $n = n_k^{start} = 1$ searching for MPC track $k = 1$ with the strongest MPC $\hat{\mathbf{s}}[n]$ and its neighbors in the next time instance

$$x_l^c = \begin{cases} 1, & \text{if } d\left(\hat{\mathbf{s}}[n], \{\mathbf{s}_l[n+1]\}_{l=1}^{L_{n+1}}\right) \leq \boldsymbol{\xi}_s \\ 0 & \text{otherwise,} \end{cases} \quad (6.13)$$

where $d(\cdot, \cdot)$ is the distance defined as

$$d\left(\hat{\mathbf{s}}[n], \{\mathbf{s}_l[n+1]\}_{l=1}^{L_{n+1}}\right) = \left| \begin{pmatrix} \hat{a}[n] - \{a_l[n+1]\}_{l=1}^{L_{n+1}} \\ \hat{\tau}[n] - \{\tau_l[n+1]\}_{l=1}^{L_{n+1}} \end{pmatrix} \right|, \quad (6.14)$$

and

$$\boldsymbol{\xi}_s = \begin{pmatrix} \xi_a \\ \xi_\tau \end{pmatrix} \quad (6.15)$$

is the maximum magnitude change and delay change, based on considerations on the physical limits of the moving objects. The resulting C initial track direction candidates

$$x_l^c \{\mathbf{s}_c[n+1]\}_{c=1}^C = \{\mathbf{s}_1^1[n+1], \mathbf{s}_1^2[n+1], \dots, \mathbf{s}_l^C[n+1]\} \quad (6.16)$$

are used for an identification of track k by predicting $\tilde{\mathbf{s}}_k[n+1]$ with the linear prediction model H . We start with the first initial direction candidate and set

$s_l[m] = s_l^1[n + 1]$ in

$$\tilde{\mathbf{s}}_k[m + 1] = H(\mathbf{s}_l[m]) = \begin{pmatrix} a_l[m] + \Delta a_l[m] \\ \tau_l[m] + \Delta \tau_l[m] \end{pmatrix}, \quad (6.17)$$

with

$$\Delta a_l[m] = a_l[m] - a_l[m - 1] \quad (6.18)$$

$$\Delta \tau_l[m] = \tau_l[m] - \tau_l[m - 1]. \quad (6.19)$$

Based on the prediction $\tilde{\mathbf{s}}_k^1[n + 2] = \tilde{\mathbf{s}}_k[m + 1]$, we can look for MPCs in the defined search ranges \mathbf{r}_{min} and \mathbf{r}_{max}

$$x_{kl}^m = \begin{cases} 1, & \text{if } \mathbf{r}_{min} \leq \{\mathbf{s}_l[m + 1]\}_{l=1}^{L_{m+1}} \leq \mathbf{r}_{max} \\ 0 & \text{otherwise,} \end{cases} \quad (6.20)$$

where

$$\mathbf{r}_{min} = \tilde{\mathbf{s}}_k[m + 1] - \boldsymbol{\epsilon}_s \quad (6.21)$$

$$\mathbf{r}_{max} = \tilde{\mathbf{s}}_k[m + 1] + \boldsymbol{\epsilon}_s. \quad (6.22)$$

The values of the maximum allowed search tolerances

$$\boldsymbol{\epsilon}_s = \begin{pmatrix} \epsilon_a \\ \epsilon_\tau \end{pmatrix} \quad (6.23)$$

depend on the time interval between two snapshots, the dynamics of the propagation channel and the quality of the measurement device. An evaluation of the algorithm results has to be performed in order to estimate appropriate search tolerance values.

Then, we check the outcome of the binary variable x_{kl}^m with

$$\sum_{l=1}^{L_m} x_{kl}^m = X. \quad (6.24)$$

In case $X = 0$, no track is found and the algorithm continues with the next *initial candidates* $\{s_l^c[n + 1]\}$. In case $X = 1$, only one *track candidate* is found and consequently a track is identified; while in case $X > 1$, more than one track candidate is found. In order to select from multiple track candidates, we use

$$\underset{x_{kl}}{\operatorname{argmin}} \sum_{l=1}^{L_{m+1}} d(\tilde{\tau}_k[m + 1], \tau_l[m + 1]) x_{kl} \quad (6.25)$$

so that $X = 1$ holds in (6.24). Now, as an MPC track is identified by three adjacent MPCs, we save

$$x_{kl}^n = x_{kl}^{n+1} = x_{kl}^{n+2} = 1 \quad (6.26)$$

and continue searching along track $k = 1$ with the linear prediction model in (6.17), for $m = \{n_k^{start} + 3, \dots, N\}$ or until the end of track k at N_k is found. We save the estimated MPC parameters of track k in

$$\mathbf{s}_k[n] = \mathbf{s}_l[n]x_{kl}^n. \quad (6.27)$$

Next, we continue in $n = n_k^{start} = 1$ with the next strongest MPC $\hat{\mathbf{s}}[n]$ not yet part of a track

$$\hat{\mathbf{s}}[n] \notin \{\mathbf{s}_k[n]\}_{k=1}^{K_n}, \quad (6.28)$$

where K_n is the number of tracked MPCs at time n . Based on $\hat{\mathbf{s}}[n]$, we start again identifying initial track direction candidates in (6.13). After L_n starting MPCs $\hat{\mathbf{s}}[n]$ are considered, we continue with $n = n_k^{start} = 2$ and look for MPCs that fulfill (6.28) to start again from (6.13). The result of the tracking algorithm is the set

$$\mathbf{S}_k = \{\mathbf{s}_k[n]\}_{n=n_k^{start}}^{N_k}. \quad (6.29)$$

The lifetime of track k is $\psi_k = N_k - n_k^{start}$. In order to obtain a Doppler frequency estimate per track k , we first retrieve m_k with linear regression

$$y + m_k x = \frac{\Delta\{\tau_k[n]\}_{n=n_k^{start}}^{N_k}}{\Delta n T_s} \quad (6.30)$$

and calculate the Doppler frequency

$$\nu_k = -m_k f_c \quad (6.31)$$

where f_c is the carrier frequency. The final outcome of the short-term MPC tracking are the following estimates

$$\theta_k = \{a_k[n], \tau_k[n], \psi_k, \nu_k\}_{n=n_k^{start}}^{N_k}. \quad (6.32)$$

6.3 Evaluation Based on an Artificial Channel

In order to evaluate the performance of the detection algorithm and both tracking algorithms, two different kinds of evaluation methods are applied. The first evaluation method is based on an artificial channel, which is created using a channel sounder pulse. This pulse is extracted from a channel sounder measurement via an RF cable and reflects the characteristics of the measurement device. The artificial channel used for the performance evaluation consists of two MPCs tracks with identical power levels, decreasing delay distances and an added noise floor with a power level at -140 dB, as shown in Fig. 6.2. This artificial channel can be regarded as a worst-case tracking scenario when considering two MPCs, since

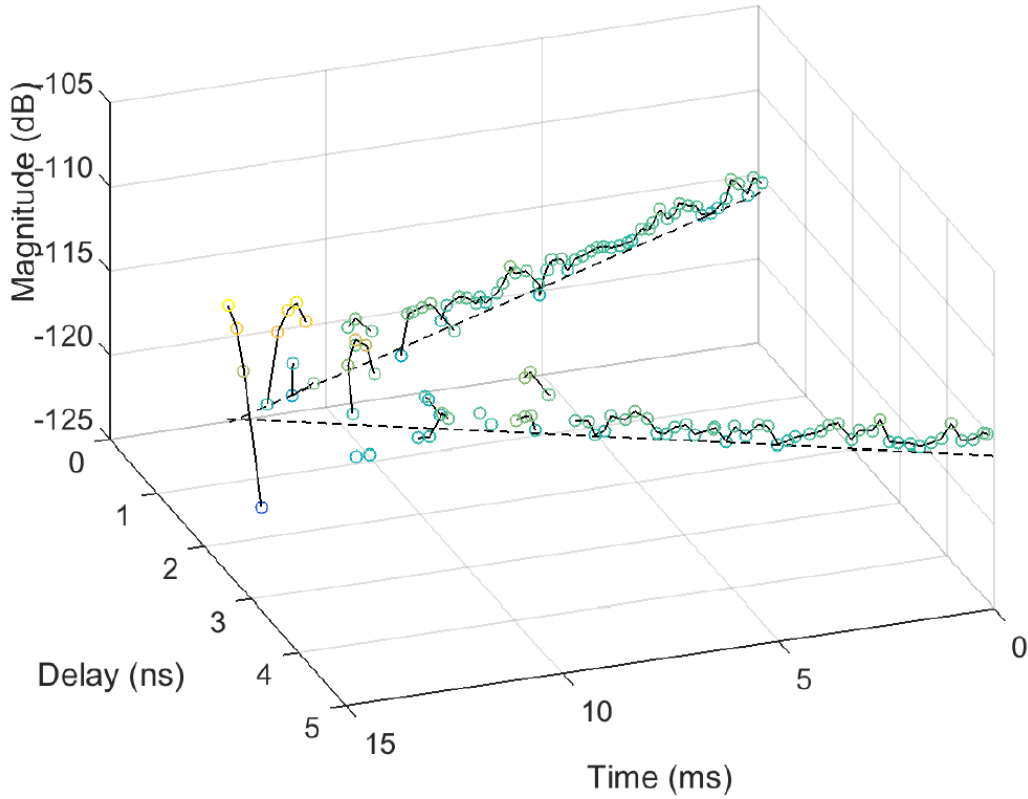


Figure 6.2: Result from proposed MPC tracking algorithm for an artificial channel created with a measured channel sounder pulse.

a greater power difference between the MPCs would lead to the dominance of one MPC and a better overall result. Since we are mainly interested in the separation of two MPC tracks that are close in terms of delay distance, we use this simple artificial channel to assess the tracking performance.

The example in Fig. 6.2 shows an artificial channel with MPC powers of -116 dB. We found that up to a delay distance of around 2.5 ns, the mean delay estimation error is below 0.03 ns with flawless tracking results, as shown for large MPC powers in Fig. 6.3 and Fig. 6.4. The malfunction of the detection algorithm at delay distances below 2.5 ns can be explained with the width of the channel sounder pulse and the effects of two superimposing pulses [47]. The decreasing distance of two complex pulses with finite bandwidth leads to constructive or destructive superposition and consequently to fluctuations of the resulting pulse, as shown in Fig. 6.2. In order to find the limits of the applied algorithms, the power level of the MPCs is reduced and the tracking results up to a distance of 2.5 ns between the approaching MPC tracks are compared to ground truth.

We compare the tracking performance of the proposed algorithm and the GM-

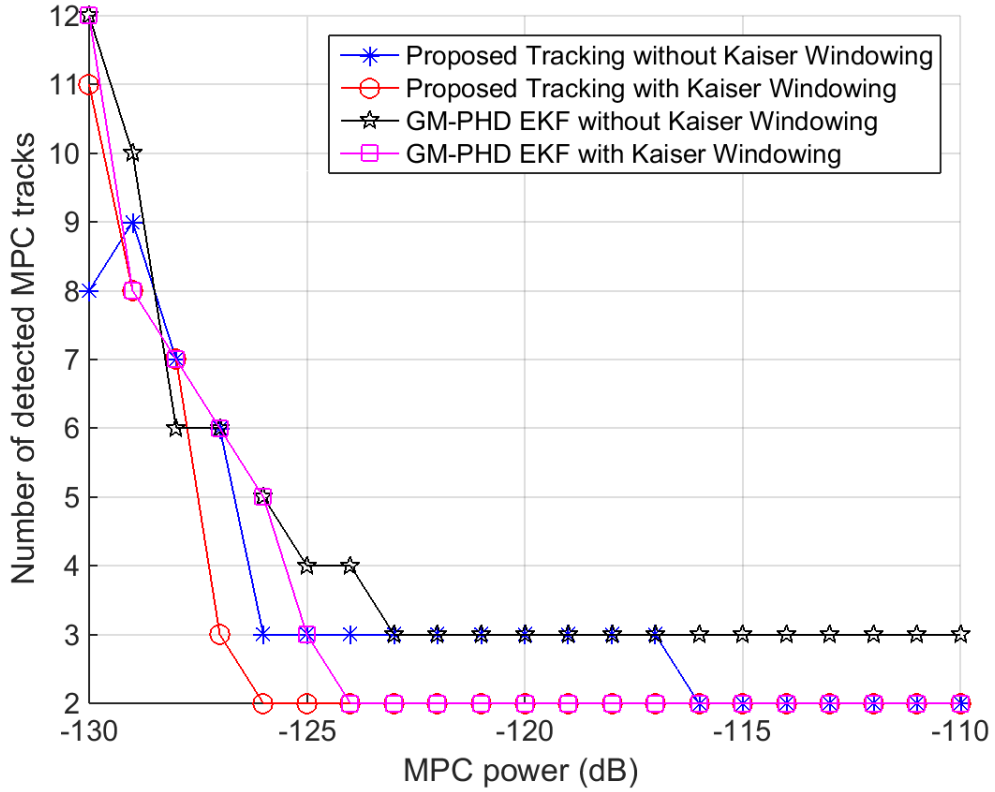


Figure 6.3: Number of detected tracks as a MPC tracking performance indicator, based on an artificial channel and delay distances above 2.5 ns.

PHD filter in Fig. 6.3 and Fig. 6.4, both with and without prior windowing. As we can observe in Fig. 6.3 and Fig. 6.4, prior Kaiser windowing results in more accurate number of tracks and lower mean delay estimation errors. The third appearing "track" without Kaiser windowing in Fig. 6.3 is due to the fact that the superimposing pulses generate a third pulse in some successive snapshots, which are misinterpreted as a track. Also, we find in Fig. 6.3 that the detected MPC tracks start to split into more than the actual two tracks at a MPC power of -124 dB for the GM-PHD filter and at a MPC power of -126 dB for the proposed algorithm. As can be found in Fig. 6.4, the mean delay estimation error at these power values is below 0.07 ns and in terms of delay estimation, the proposed tracking algorithm has a better performance than the GM-PHD filter.

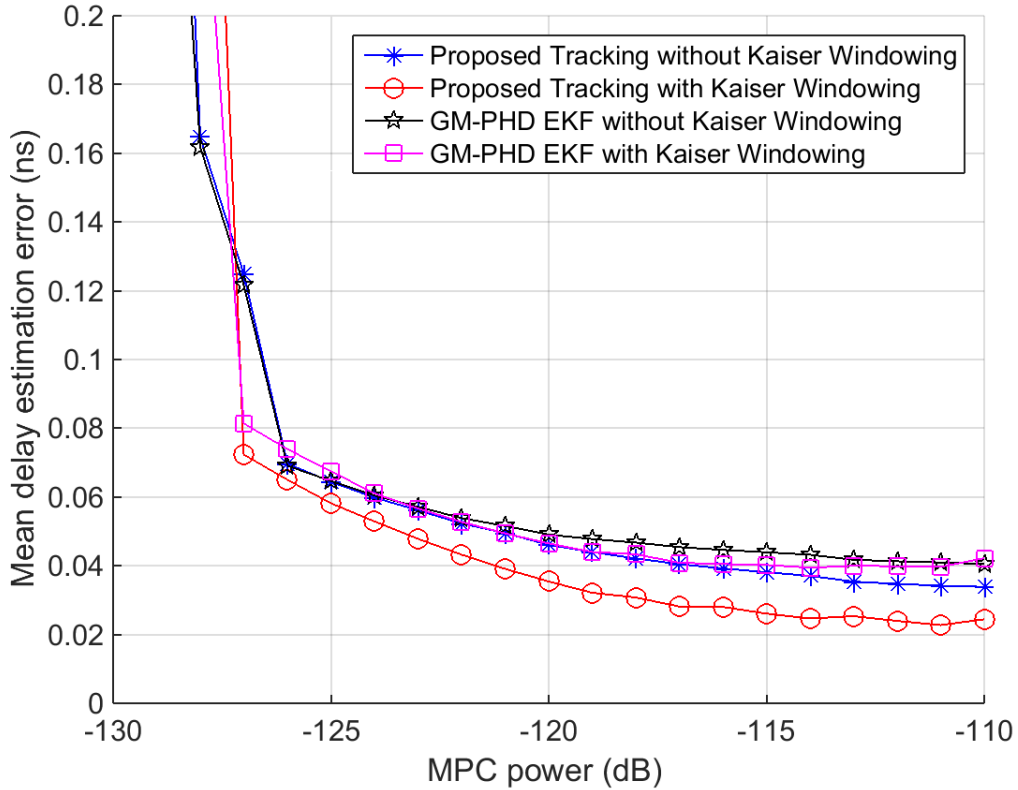


Figure 6.4: Mean delay estimation error as a MPC tracking performance indicator, based on an artificial channel and delay distances above 2.5 ns.

6.4 Evaluation Based on Channel Measurement Data

The second performance evaluation is based on visual inspection of tracking results from actual channel measurement data. The goal of this evaluation is to identify false positives and false negatives, i.e. tracking mistakes and missed tracks.

The tracking algorithms are applied to channel data from a measurement run in the so-called Tiergartentunnel in Berlin. The measurement vehicles are driving southbound in a convoy with speeds between 42 km/h and 52 km/h at distances between 75 m and 110 m, with the above mentioned uncertainty of around 20 m. The shape of the tunnel is curved and the traffic density during measurement was low, as can be seen in Fig. 11.7. One measurement run of the HHI channel sounder contains 10,000 snapshots, which are organized into sets of snapshots. In this measurement run, a set consists of six snapshots with a time interval of 0.717 ms between the snapshots, which results in a set recording time of around 3.6 ms. The

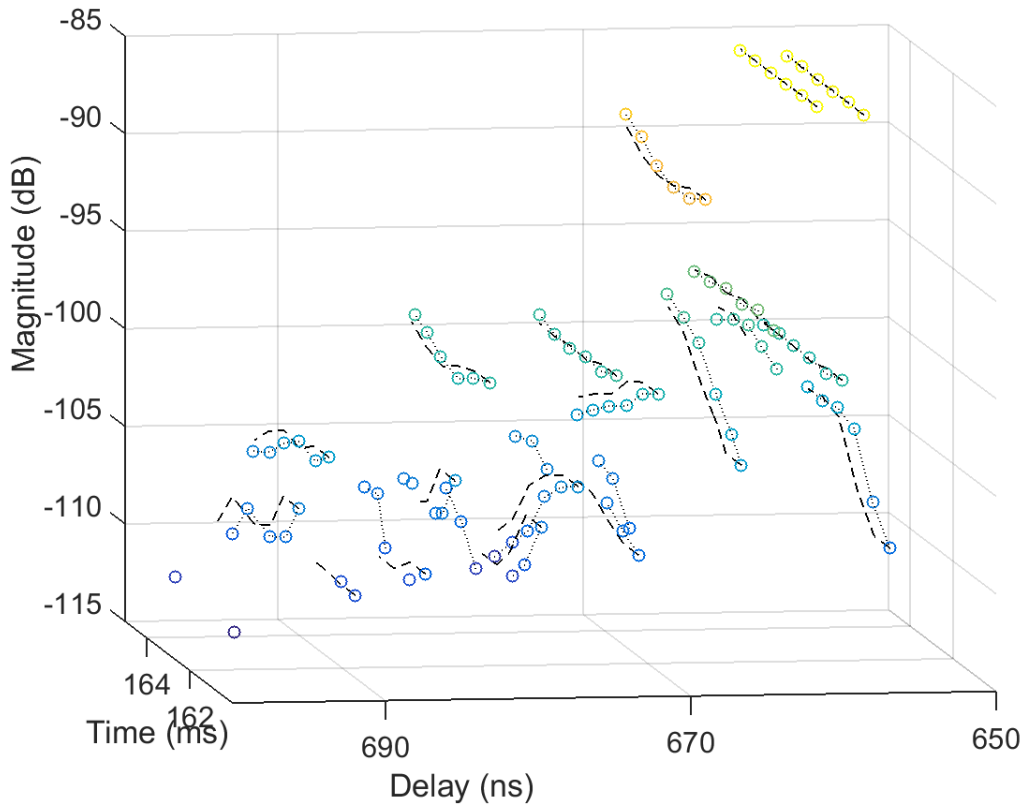


Figure 6.5: MPC tracking results for a recorded channel measurement set in a tunnel convoy traffic communication scenario. The dashed lines result from the GM-PHD filter with EKF, whereas the dotted lines result from the proposed tracking algorithm.

time interval between the starting of two sets is 10 ms. We recorded 1666 sets, which amounts to a total measurement time of around 16.7 s. This measurement set-up enables longer measurement runs compared to continuous recording and in addition reflects the packet on-air times of CAMs based on IEEE 802.11p. One of the most relevant challenges in vehicular communication is a reliable frame detection, which corresponds to the time-variant behavior of the channel while a transmission packet is on the air. Therefore, we selected the length of the set recording time to account for the maximum IEEE 802.11p frame duration of 2 ms, considering the maximum allowed payload of 1500 Bytes.

In order to evaluate the tracking algorithms on demanding MPC tracks, we use the described measurement run from a convoy traffic tunnel scenario with dense multipath inter-arrival times. Based on the results, we tuned the parameters of the tracking algorithm empirically and found that with a snapshot time interval

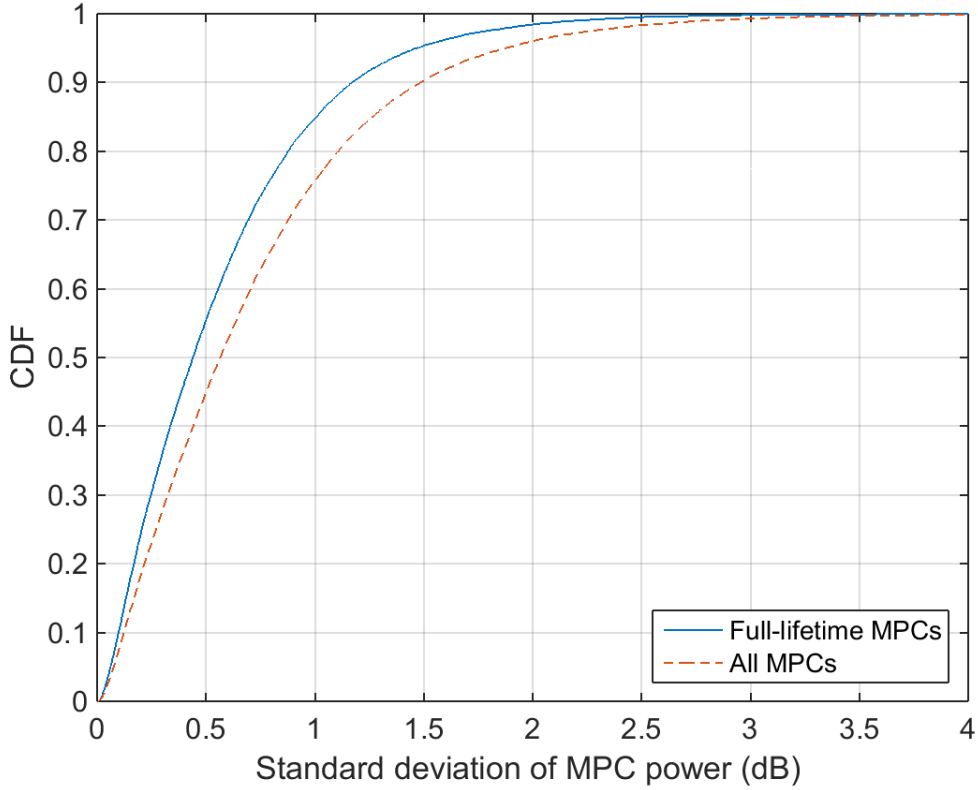


Figure 6.6: Standard deviation of tracked wideband multipath components power for entire measurement run.

of $T_s = 0.7$ ms, a delay search tolerance value of $\epsilon_\tau = 0.5$ ns and a magnitude search tolerance value of $\epsilon_a = 10$ dB is suitable. These high search tolerance values have been selected since they leave enough space for deviations from the instantaneously observed delay/magnitude change without, due to the sparsity of the channel, leading to additional false positives. In particular weak MPCs undergo significant fluctuations and require larger search tolerances. These search tolerance values are most likely also adequate for other V2V scenarios, if applied on measurement data with similar snapshot time intervals and similar measurement bandwidth. This assumption is based on the fact that these values were also appropriate for a highway measurement run we processed and analyzed.

Fig. 6.5 shows the time-variant channel impulse response of a tunnel scenario measurement, where circles indicate the detected MPC peaks, the dotted lines show the outcome of the proposed tracking algorithm and the dashed lines show the results from the GM-PHD filter. In Fig. 6.5, we can observe that, compared to the GM-PHD filter tracks, the tracks from the proposed algorithm are more

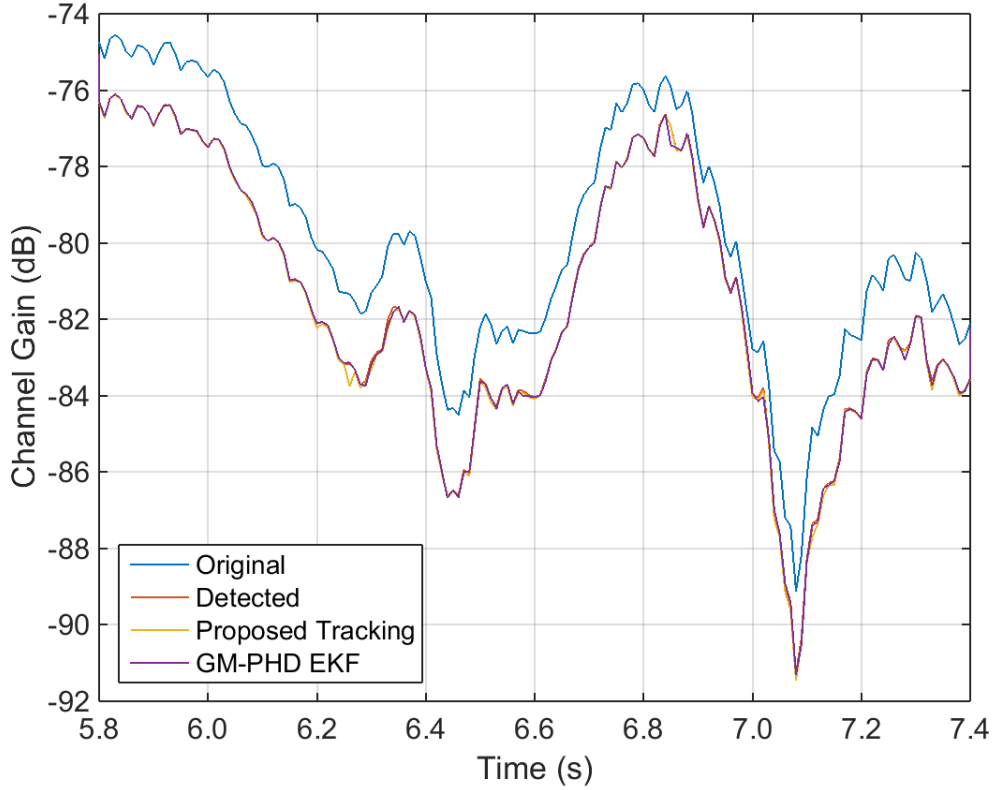


Figure 6.7: Comparison between the original channel gain after Kaiser windowing and the captured channel gain after the detection, the proposed tracking algorithm and the GM-PHD filter with EKF.

reactive to the dynamic MPC behavior. Also, we can observe that some diffuse multipath components (DMC) peaks are not linked to any MPC track and result in a loss of the captured channel gain. Fig. 6.7 shows for a part of our measurement run the original channel gain after the mentioned Kaiser windowing, the detected channel gain and the tracked channel gain of both tracking approaches, which are defined at time instance n by $\sum_{j=1}^J |a_j|^2$, $\sum_{l=1}^{L_n} |a_l|^2$ and $\sum_{k=1}^{K_n} |a_k|^2$ respectively. It can be observed that all processed channel gain curves, the detected and the two tracked curves, are below the original channel gain curve and follow the original curve progression very well with a certain distance.

Fig. 6.8 displays the power losses due to the applied algorithms, where it becomes clear that the main loss is due to the detection algorithm. Also, we can observe in Fig. 6.8 that the loss decreases for a larger channel gain, which can be explained with DMCs being beyond the limited dynamic range of the channel sounder when receiving stronger MPCs. When comparing the two tracking approaches in Fig. 6.8,

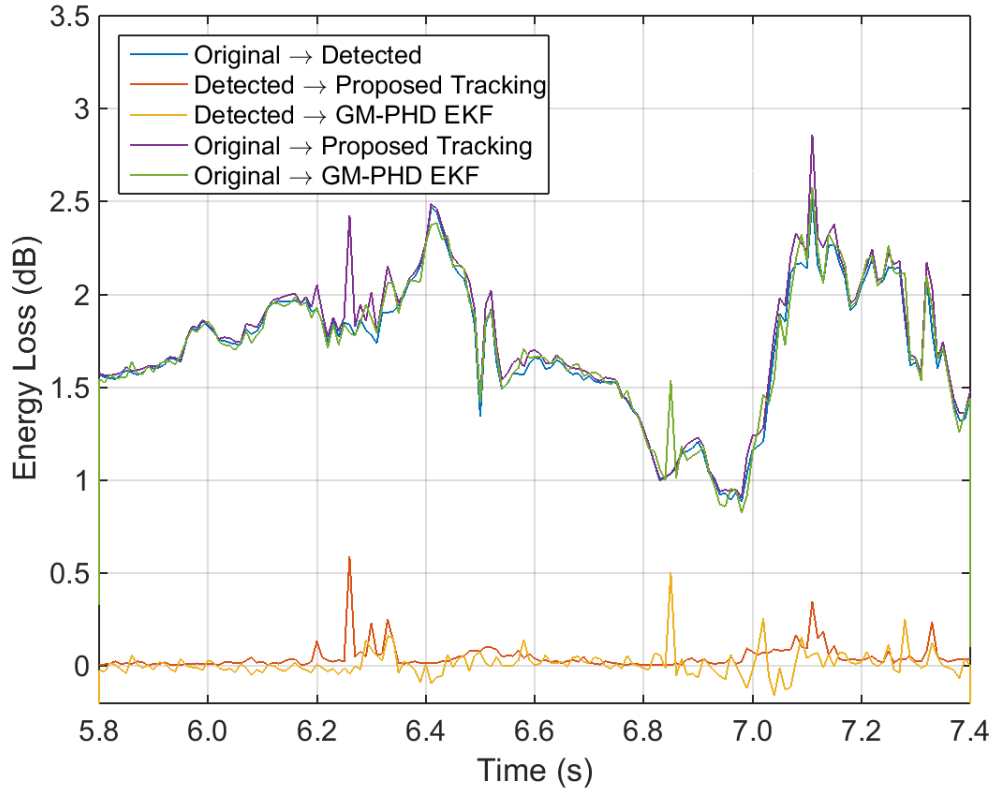


Figure 6.8: Power losses due to the detection, the proposed tracking algorithm and the GM-PHD filter with EKF.

we can observe that each algorithm has tracking difficulties at different parts of the measurement run (the proposed algorithm at 6.25 s and the GM-PHD filter at 6.85 s). Furthermore, we can observe that the energy loss of the GM-PHD filter is sometimes below zero. This can be explained with the set-up of this algorithm and the "survival" of a track, even without any measurement data supporting this track. In contrast, the proposed algorithm simply connects detected MPCs and therefore never results in a negative loss. The mean square error of the energy loss compared to the detected channel gain is 0.0065 dB for the proposed algorithm and 0.005 dB for the GM-PHD filter. For the entire measurement run, we observed an average total energy loss of around 2 dB for both tracking approaches, with a standard deviation of around 0.4 dB.

The main advantage of our proposed algorithm is its comparatively low computational effort. The performance of our tracking method is comparable to the GM-PHD filter, but its numerical complexity is strongly reduced. The proposed algorithm has a linear time complexity, due to the fact that it processes on a snap-



Figure 6.9: Video snapshot of conducted measurement run in a tunnel scenario, taken from the rear measurement vehicle.

shot basis every MPC track separately. In contrast, the GM-PHD filter predicts and processes multiple targets simultaneously, which leads to a linear complexity in the number of targets and a cubic complexity in the number of snapshots [48]. In order to limit the computational effort of a corresponding implementation, several thresholds are used to reduce the number of targets (e.g. the last three variables in Table 6.1). However, strongly “optimized” threshold values come at the expense of a reduced tracking accuracy.

We estimate a time complexity reduction factor of up to 10, based on the fact that processing 100 measurement snapshots with our algorithm take around 95 s on a standard computer, whereas processing with our GM-PHD filter implementation requires 911 s.

In addition, our algorithm leads to more accurate delay estimates if applied on measurement data with low measurement noise, as can be found in Fig. 6.4. This is due to the fact that our approach interrelates detected peaks instead of generating processes that approximate tracks, as done in the GM-PHD filter. In other words, the GM-PHD filter usually lags a little behind the measured dynamics. Furthermore, since the resulting track is not directly linked to the detected peaks, a track might be found where there is actually no track. Finally, due to the high number of algorithm parameters, finding the proper parameter value set is a challenging task. We do not claim that our algorithm is applicable for any tracking problem, but it showed that this approach is a better solution for our measurement data compared

to the GM-PHD filter. One disadvantage of our proposed algorithm is that it fails to track if multiple peaks in adjacent snapshots are missing. This shortage could be overcome by continuously searching for peaks along the observed delay (and magnitude) change, as done in [33]. On the other hand, bridging a track across multiple snapshots might result in less reliable tracking results and furthermore does not reflect what has been measured.

From Fig. 6.5, we can observe that the power of strong MPCs stay nearly constant within a measurement set, whereas smaller MPC tracks show larger power fluctuations and shorter lifetimes. The large measurement bandwidth decreases the number of physical MPC in a superimposed MPC and consequently decreases the amplitude fluctuations. A CDF of the MPC power standard deviation over the entire measurement run is shown in Fig. 6.6, based on the proposed tracking results of 34,000 MPC tracks and 23,000 full-lifetime MPC tracks respectively. We can observe in Fig. 6.6 that 90% the MPCs have a power standard deviation of less than 1.5 dB. The long-term MPC tracking algorithm described in the next section only takes full-lifetime MPCs into consideration, where 85% of the MPCs show a power standard deviation of less than 1 dB over the set recording period of around 3.6 ms.

6.5 Interconnecting MPC Tracks (Type 2)

In order to investigate the large-scale evolution of MPC tracks measured with a snapshot organization Type 2 according to Table 4.1, the so-called inter-tracking algorithm is applied. This additional tracking method is needed to interrelate MPC tracks across adjacent recording sets, which are separated by gaps of around 6.4 ms. For this algorithm, only full-lifetime MPCs are considered, i.e. MPC tracks with a lifetime equal to the duration of the recording set. Excluding non-full-lifetime MPC tracks is based on the observation that tracks appearing or disappearing within the set recording time of 3.6 ms rarely lead to a MPC survival of 10 ms or more. Disregarding these MPC tracks results in an additional power loss of around 5%, but increases the reliability of the long-term tracking.

Our inter-tracking approach is similar to the tracking approaches described in [25] and [49]. However, other than in these publications, our approach is not applied on direction-resolved measurement data, but calculates the multipath distance based on delay, power and Doppler frequencies estimates of individual MPCs. The main idea behind the algorithm is simple and can be best explained with Fig. 6.10, where the circles indicate the averaged powers and delays of time-variant MPCs of the current set, and the crosses indicate the corresponding MPCs of the next recording set. As the channel is quite sparse, it is straightforward to relate the MPCs of different sets. The algorithm starts with the strongest MPC track in the current set, defines a two-dimensional search range and searches in the next set for

possible candidates. In the next step of the algorithm, the delay change (Doppler frequency) of the current MPC track is used to predict the delay location of the MPC track in the next set. The same is done in the opposite direction; the delay change of the MPC track in the next set is used to predict the delay location of the MPC track in the current set. This additional prediction in the opposite direction increases the reliability of the tracking outcomes and is similar to the "two-way-matching" described in [25]. The deviation between the actual delay value and the predicted delay value is compared to different threshold values, again for both directions. Two MPC tracks are found to be related, if both deviations are below this threshold.

For the mathematical description of the inter-tracking algorithm, we have to note that $h(nT_r, uT_b) = h[n, u]$, where T_r is the recording set period. We take the average MPC gain \bar{a}_k and $\bar{\tau}_k$ from (6.31) and define the estimation parameters for the inter-tracking algorithm

$$\Theta_k = \{\bar{a}_k, \bar{\tau}_k, \psi_k, \nu_k\} \quad (6.33)$$

with $k \in \{1 \dots K_i\}$ and K_i being the number of tracks at time instance i . Long-term time instances are denoted as i , in order to be clearly distinguishable from short-term time n . We only consider full-lifetime MPCs $\psi_k \stackrel{!}{=} n_{snap}$, with n_{snap} being the number of snapshots per set and define a subset

$$\mathbf{q}_k[i] = \begin{pmatrix} \bar{a}_k[i] \\ \bar{\tau}_k[i] \\ \nu_k[i] \end{pmatrix}. \quad (6.34)$$

We start again with the strongest MPC $\hat{q}[i]$ in $i = i_k^{start} = 1$ and search for candidates using

$$x_k^c = \begin{cases} 1, & \text{if } d(\hat{\mathbf{q}}[i], \{\mathbf{q}_k[i+1]\}_{k=1}^{K_{i+1}}) \leq \boldsymbol{\xi}_q \\ 0 & \text{otherwise,} \end{cases} \quad (6.35)$$

where $d(\cdot, \cdot)$ is defined as in (6.14) and $\boldsymbol{\xi}_q$ is set empirically to a maximum delay change value of $\xi_\tau = 1$ ns and a maximum magnitude change value $\xi_a = 5$ dB. The identified candidates

$$x_r^c \{\mathbf{q}_c[i+1]\}_{c=1}^C = \{\mathbf{q}_r^1[i+1], \mathbf{q}_r^2[i+1], \dots, \mathbf{q}_r^C[i+1]\} \quad (6.36)$$

are used together with the linear prediction $\tilde{\tau}_r[i+1]$ from model G in

$$\tilde{\tau}_r[i+1] = G(\bar{\tau}_k[i], \nu_k[i]) = \bar{\tau}_k[i] - \nu_k[i] f_c T_r \quad (6.37)$$

to find the closest candidate in terms of delay change prediction

$$\eta = \underset{c}{\operatorname{argmin}} d(\tilde{\tau}_r[i+1], x_r^c \{\bar{\tau}_c[i+1]\}_{c=1}^C). \quad (6.38)$$

Now, we use the selected candidate η to predict the delay in the opposite direction

$$\tilde{\tau}_k[i] = \bar{\tau}_r^\eta[i+1] + \nu_r^\eta[i+1]f_cT_r \quad (6.39)$$

and check the condition

$$x_{rk}^i = \begin{cases} 1, & \text{if } d_r \leq \chi \wedge d_k \leq \chi \\ 0 & \text{otherwise,} \end{cases} \quad (6.40)$$

where

$$d_r = d(\tilde{\tau}_r[i+1], \tau_r^\eta[i+1]) \quad (6.41)$$

$$d_k = d(\tilde{\tau}_k[i], \tau_k[i]) \quad (6.42)$$

The final output of the long-term tracking is

$$\mathbf{q}_r[i+1] = \mathbf{q}_k[i]x_{rk}^i. \quad (6.43)$$

The different threshold values for χ are coded in Fig. 6.10 and Fig. 6.11, where the solid red line indicates a delay prediction error below 0.1 ns, the dashed magenta line an error below 0.2 ns, the dash-dotted blue line below 0.5 ns and the dotted black line below 1.0 ns. The developed algorithm also makes it feasible to relate MPC tracks across different MIMO channels. In the following, we analyze the results from the antennas mounted on the left edge of the vehicle roofs.

The MPC inter-tracking result for a small part of the measurement run is shown in Fig. 6.11, where each time instance represents the mean MPC powers of a time-variant channel impulse response as shown Fig. 6.5. Likewise, the MPCs in Fig. 6.5 can be related to the MPC powers at 250 ms and 260 ms in Fig. 6.11. As previously mentioned, only full-lifetime MPC tracks are considered for the long-term tracking algorithm. The example in Fig. 6.11 shows that most of the full lifetime MPC tracks can be related to adjacent MPC tracks, yet with different levels of trustworthiness as indicated by the different colors and line styles. Strong MPC tracks can be connected with higher reliability (solid red line), whereas weaker MPC tracks can only be related with higher tolerances. For this measurement run, only 5% of the power of all (full lifetime) MPCs could not be related to adjacent MPC tracks. The lowest delay prediction error below 0.1 ns holds still for 72% of the power of all connected MPC tracks.

From Fig. 6.11, several observations regarding the long-term evolution of MPCs can be made. The strongest 2-3 MPC tracks show a parallel and wave-like power fluctuation behavior. Another MPC track at around -90 dB is comparatively constant and shows also a (reversed) wave-like power fluctuation after 400 ms. Starting at 200 ms, a MPC track at -97.5 dB gains power and becomes the strongest MPC at 320 ms. Several weaker MPC tracks appear, reach a small power level and disappear within a short period, for instance the track between 350 and 400 ms. Very

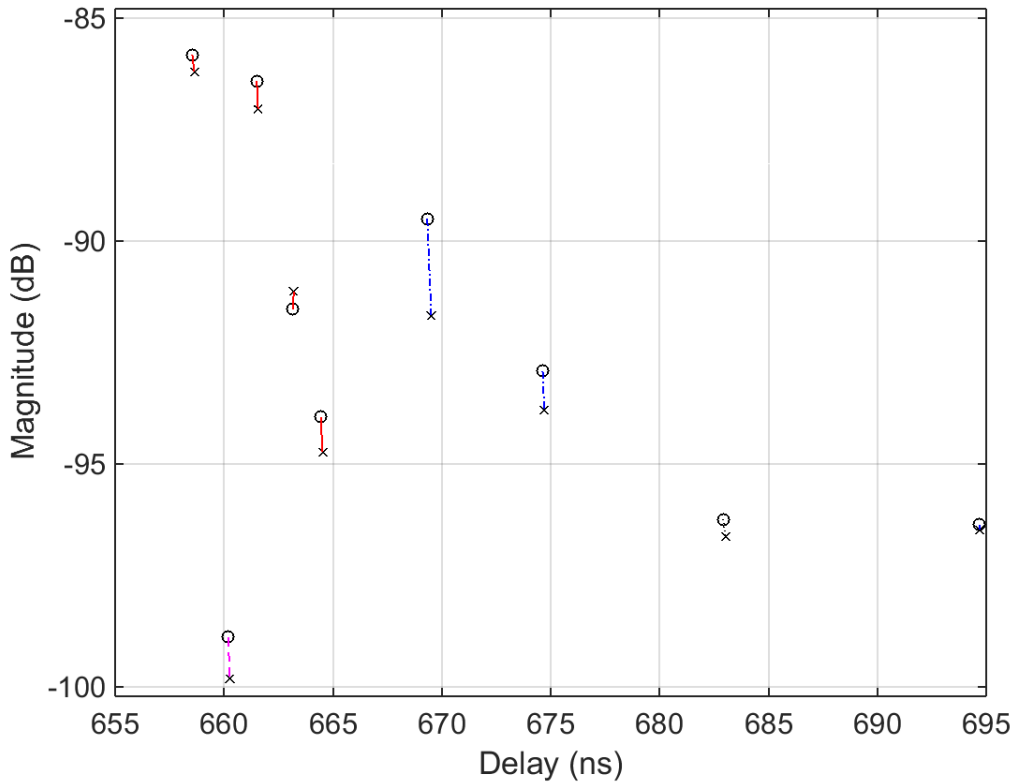


Figure 6.10: Relating MPCs of current set (circles, 250 ms in Fig. 6.11) to MPCs of next set (crosses, 260 ms in Fig. 6.11).

rarely (full-lifetime) MPC tracks appear in one set only, i.e. circles without any connecting line.

Summing up the power losses of all processing steps, 2 dB power loss due to DMCs in the short-term MPC tracking, around 5% power loss due to the neglect of non-full-lifetime MPCs and again 5% power loss due to losses in the inter-tracking, the total tracking power loss is 2.4 dB. This means that the final long-term results and the drawn statistical conclusions reflect around 57% of the measured channel power. The remaining power can be assigned to diffuse or other non-trackable MPCs, which have a minor impact on fading effects compared to specular MPCs. We therefore consider the temporal behavior of MPCs in the measured propagation channel well represented with our tracking results.

The wideband measurement data and the applied algorithms allow an extraction of all relevant MPC parameters. Here, we focus on the long-term MPC statistic results for the number of MPCs and the birth/death rate of MPCs. The tunnel measurement run with 1666 sets results in a distribution of the number of MPCs

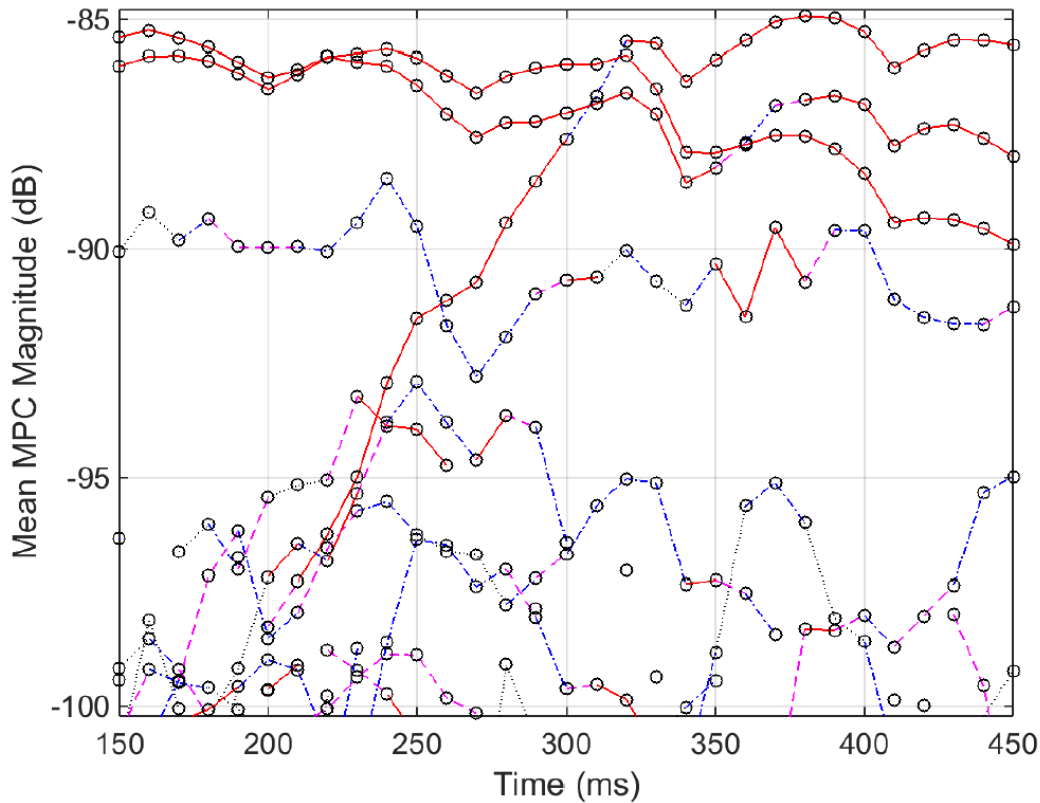


Figure 6.11: Long-term tracking of MPC powers in the tunnel scenario. At the beginning two strong MPC tracks can be observed, whereas three dominant tracks can be found at the end of the diagram. The two-way delay prediction errors obtained from (6.37) and (6.17) are displayed as solid red line with errors $\chi \leq 0.1$ ns, dashed magenta $\chi \leq 0.2$ ns, dash-dotted blue line $\chi \leq 0.5$ ns and dotted black line $\chi \leq 1.0$ ns.

as depicted in Fig. 6.12. The smooth shape of the CDF indicates a sufficiently large sample. Fig. 6.13 shows the CDF of the birth and death rate of MPCs per meter travelled, i.e. the number of MPCs appearing or disappearing per cumulative distance of both vehicles.

One conclusion from this chapter is the observation that channel sounder measurements at 5.7 GHz with a bandwidth of 1 GHz lead to a sparse channel impulse response with favorable properties. The wide bandwidth makes highly accurate MPCs estimation and tracking of individual MPCs feasible. Our proposed detection and tracking algorithms follow very well the progression of the channel gain fluctuations, with a power loss of only 2.5 dB. Compared to the GM-PHD filter, the proposed tracking algorithm has a comparable or better tracking performance

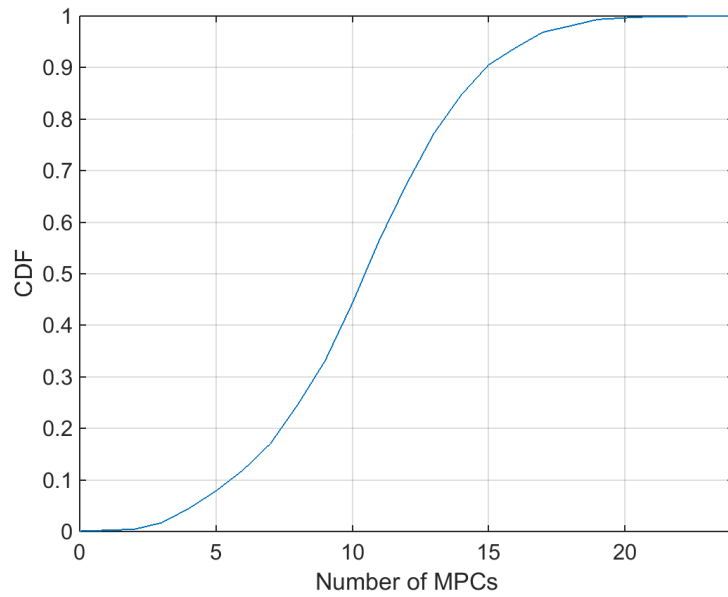


Figure 6.12: Statistical distribution of number of MPCs in tunnel scenario.

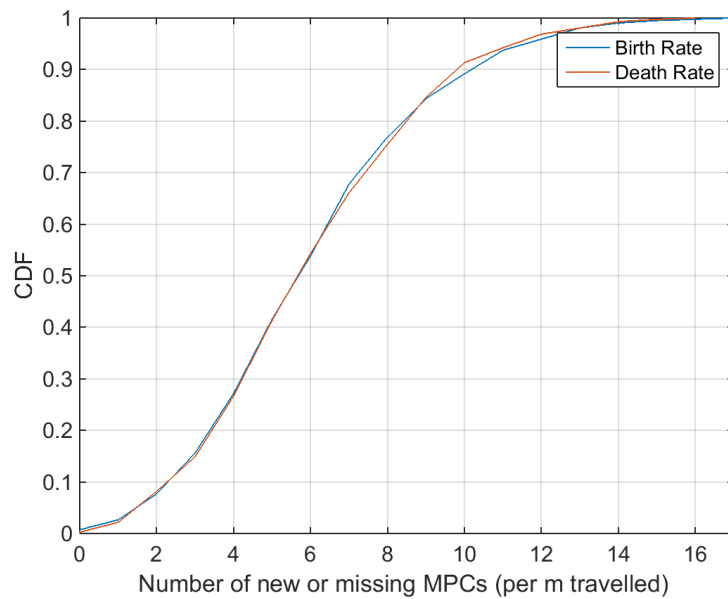


Figure 6.13: Statistical distribution of birth/death rate of MPCs in tunnel scenario.

and a significantly lower complexity. The proposed tracking method works flawless down to an SNR of 14 dB with a delay estimation error of 0.07 ns. In order to track the long-term evolution of MPC and relate tracks across measurement gaps

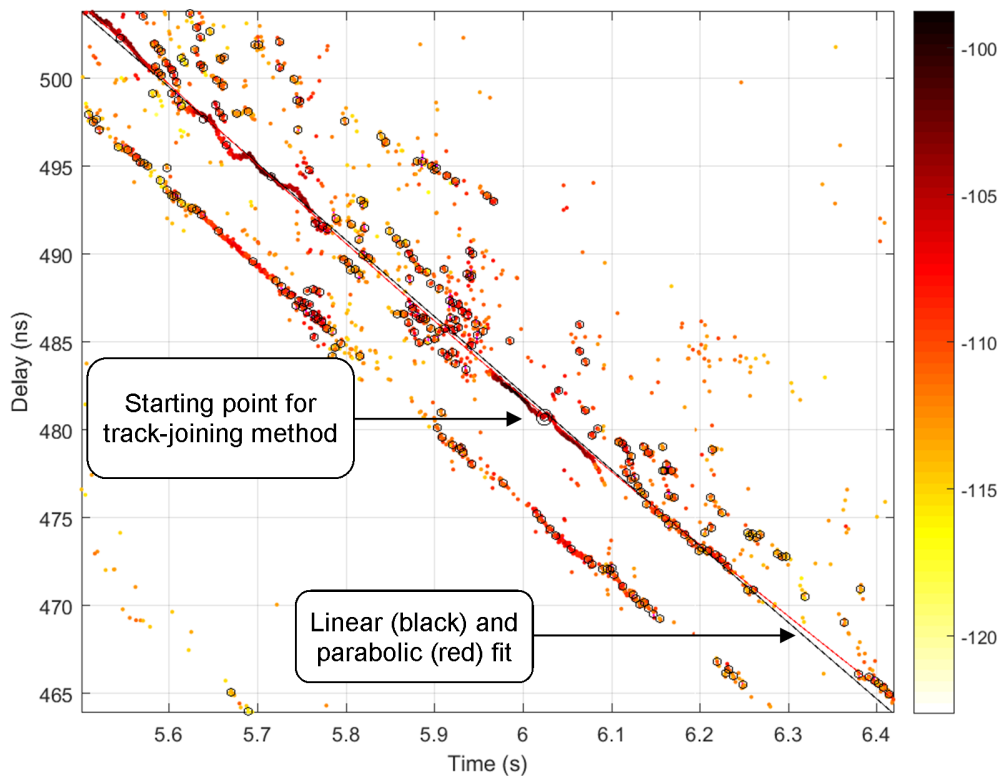


Figure 6.14: Discontinued MPC tracks and results from a track-joining method.

of 6.4 ms, an inter-tracking method is applied. Based on these results, statistical distributions on the number of MPCs and the birth/death rate are drawn.

6.6 Joining Discontinued MPC Tracks (Type 1)

The previous section covers an interconnection method across adjacent recording sets for short-term MPC tracks, which were recorded according to the snapshot organization Type 2 in Table 4.1. The tracking method in Section 6.2 performs well for short-term periods, but measurement data recorded with longer recording sets according to Type 1 (Table 4.1) can lead to discontinuous MPC tracks, as can be seen in Fig. 6.14. This is often due to fast shadowing effects and the disappearance of the MPC power. Therefore, the long-term analysis of MPC tracks recorded with Type 1 requires an adequate method. The purpose of this so-called track-joining

method is the identification of MPC tracks that are related to the same scattering object and a subsequent joining of these tracks.

The outcome from the tracking method described in Section 6.2 outputs in 6.32 a set of K tracks

$$\Theta = \{\theta_k\}_{k=1}^K, \quad (6.44)$$

with its elements

$$\theta_k = \{a_k[n], \tau_k[n], \psi_k, \nu_k\}_{n=n_k^{start}}^{N_k}, \quad (6.45)$$

where $a_k[n]$ is the power, $\tau_k[n]$ the delay, ψ_k the lifetime and ν_k the Doppler of MPC k at time instance n .

The MPC lifetime ψ_k gives a good indication on the dependability of the initial track estimates. Hence, we start our track-joining algorithm with the longest track. We apply a linear regression to its delay values to obtain the initial so-called reference line

$$\tau_w^r[n] = y_w^r + m_w^r n. \quad (6.46)$$

The parameters y_w^r and m_w^r describe the initial ($r = 1$) line estimates of the first ($w = 1$) joined track. In order to relate the remaining tracks to this reference line, we introduce a simplification of the tracks and let tracks be represented by its core coordinates. We define the track core as the center of its lifetime

$$\bar{n}_k = n_k^{start} + \frac{N_k - n_k^{start}}{2}, \quad (6.47)$$

and the average delay $\bar{\tau}_k$ during its lifetime. Based on the reference line estimates and the time instances \bar{n}_k of the track cores, we compute the corresponding delay values of the reference line

$$\hat{\tau}_w^r[k] = y_w^r + m_w^r \bar{n}_k. \quad (6.48)$$

Now, we can identify the track cores and therefore the tracks, that are close to the reference line by checking the following condition for all tracks $k \in \mathbb{K} = \{1 \dots K\}$

$$u_w^r = \begin{cases} k, & \text{if } |\hat{\tau}_w^r[k] - \bar{\tau}_k| < \epsilon_\tau \\ \emptyset & \text{otherwise,} \end{cases} \quad (6.49)$$

where the maximum delay difference ϵ_τ is set to be 1 ns. We obtain a set $\mathbb{U}_w^r = \{u_1^r\} \subseteq \mathbb{K}$ of U_w^r tracks. The current tracks related to joint-track w is

$$\Theta_w^r = \{\theta_k \mid k \in \mathbb{U}_w^r\} \subseteq \Theta. \quad (6.50)$$

We use all available delay values of subset Θ_w^r to obtain a new ($r = 2$) reference line with updated line estimates in (6.46), the corresponding track core delay values $\hat{\tau}_w^r[k]$ in (6.48) and finally a new subset \mathbb{U}_w^r by applying (6.49). The algorithm terminates, if no additional tracks close to the reference line are found, i.e.

$U_w^r = U_w^{r-1} = U_w$. The final set \mathbb{U}_w of joint-track w is subtracted from the data, leaving $K - U_w$ remaining tracks for the further processing and the corresponding joint-tracks.

The final reference line of joint-track w

$$\tau_w[n] = y_w + m_w n \quad (6.51)$$

not only joins tracks related to the same scattering object, but also allows the inclusion of the MPC power not tracked by the preceding short-term tracking, as indicated in Fig. 6.14.

The MPCs of a channel sounder data set, the colored dots in Fig. 6.14, can be described with $\mathbf{O} = \{o_v\}_{v=1}^V$ and its elements $o_v = \{a_v, \tau_v, n_v\}$, where V is the number of all detected MPCs, with $v \in \mathbb{V} = \{1, \dots, V\}$. We identify MPCs that are close to the final reference line in (6.51) by checking the condition

$$z_w = \begin{cases} v, & \text{if } |\tau_v - \tau_w[n_v]| < \epsilon_\tau \\ \emptyset & \text{otherwise,} \end{cases} \quad (6.52)$$

The obtained set $\mathbb{Z}_w = \{z_w\} \subseteq \mathbb{V}$ yields the Z_w MPCs related to joint-track w

$$\mathbf{O}_w = \{o_v \mid v \in \mathbb{Z}_w\} \subseteq \mathbf{O}. \quad (6.53)$$

Since the reference line $\tau_w[n]$ is unbounded, we have to define the starting point and the terminal point of the joint-track. In order to do so, we regard the MPC density in set \mathbf{O}_w per time interval Δn . Let $\tilde{z}_w[i]$ be the number of MPCs within the interval $[(i-1)\Delta n + 1, i\Delta n)$, then the sliding window average density is

$$d_w[i] = \frac{\tilde{z}_w[i]}{\Delta n}. \quad (6.54)$$

The mean density of MPCs detected in \mathbf{O}_w is $\bar{d}_w = \frac{Z_w}{N}$. We define the starting point and terminal point of the joint-track w to be the first and the last time instance where $d_w[i] \geq \bar{d}_w$ holds respectively.

Finally, the delay values of o_v are changed to the values of the reference line

$$\hat{o}_v = \{a_v, \tau_w[n_v], n_v\} \quad (6.55)$$

and we obtain the final (linear) joint-track

$$\hat{\mathbf{O}}_w = \{\hat{o}_v \mid v \in \mathbb{Z}_w\} \subseteq \mathbf{O}. \quad (6.56)$$

In addition, we apply a polynomial curve fitting of second order to the MPC set \mathbf{O}_w , where the delay values are forced to the parabolic reference line (red line in Fig. 6.14).

Due to the longer lifetime of a joint-track compared to individual short-term tracks, the track-joining method allows better estimation of the delay slope, i.e. the Doppler estimate. The accuracy of this estimate is critical for a reliable association of the MPC track to the scattering objects as described in Section 8.2.2. Furthermore, the track-joining method enables the *true* lifetime estimation of a long-term MPC with short-term discontinuities.

7 Statistical Characterization of Wideband MPC in V2V Channels

Realistic propagation modeling requires a detailed understanding and characterization of the radio channel properties. This chapter presents statistical models for the number of, birth rate, lifetime, excess delay and relative Doppler frequency of individual MPCs. Our findings are concluded from 72 measurement runs in eight relevant vehicular communication scenarios and reveal wide insights into the dynamic propagation process in vehicular communication scenarios.

For our measurements we use an Audi A4 Avant as transmitter and a Renault Scenic as receiver vehicle. The transmitter vehicle is equipped with two omnidirectional and vertically polarized antennas mounted on the roof at the left and right edges of the vehicle (Tx1Out and Tx2Out in Fig. 4.5). The receiver vehicle is also equipped with the same kind of antenna on the roof at the left edge of the vehicle (Rx1Out). In addition to this outside antenna, we installed two vertically polarized antennas at different locations inside the receiver vehicle as shown in Fig. 4.5.

Each vehicular communication scenario requires a suitable and beneficial setup of measurement timing (see Type 2 in Table 4.1). One measurement run of the HHI channel sounder contains 10,000 snapshots. Instead of using all snapshots consecutively for a single continuous recording, we organize the available snapshots into sets of 6-13 snapshots. The time interval between the snapshots is 0.2-0.7 ms, which results in a set recording time of 2.4-3.6 ms. The time interval between the first snapshot of two consecutive sets is 10-100 ms. We recorded 769-1666 sets, which amounts to a total measurement time of 16-124 s per run. This measurement setup with gaps between recording sets permits longer measurement runs and in addition reflects the packet on-air time of CAMs based on IEEE 802.11p. The length of the set recording time accounts for the maximum IEEE 802.11p frame duration of 2 ms for the maximum allowed payload of 1500 Bytes.

Summing up all 72 measurement runs, the performed analysis is based on 108 min of total measurement time. The total pure recording time without gaps between sets amounts to 240 s. Since we conducted measurements with two Tx antennas and three Rx antennas, the effective total measurement time increases by a factor six (antenna pairs) and adds up to a total of almost 11 h of measurement time or to a

total of 24 min of pure recording time.

7.1 Measurement Environments and Setup

We investigate eight relevant vehicular communication scenarios and selected corresponding measurement sites in or around Berlin, accordingly. During measurements, each vehicle was equipped with a video camera and a highly accurate GNSS system for positioning. The histograms in Fig. 7.1 give an overview of the distances between Tx and Rx during the measurement runs, whereas Fig. 7.2 displays the corresponding relative (Tx+Rx) speed. The measured scenarios and corresponding sites are:

H2I - Highway-to-Infrastructure: 12 measurement runs. The stationary infrastructure antenna was located near a former custom office called Zollamt Dreilinden. The antenna was mounted at 3.50 m height on the west side of highway, around 5 m away from the highway guardrail and 6 m from the custom office building. During the measurements, we observed a medium-range traffic density and several large vehicles. The distance between the Tx and Rx antennas is evenly distributed up to 500 m, with relative speeds between 80 and 120 km/h as indicated in Fig. 7.1 and 7.2.

HCT - Highway Convoy Traffic: 12 measurement runs. One measurement run was conducted northbound on the highway A100 between Spandauer Damm and Siemensdamm, with dense traffic and several large vehicles. The remaining 11 measurement runs were conducted clockwise on the highway A10, starting from the highway junction Kreuz Oranienburg to the junction Dreieck Spreeau. Some parts of the highway were under construction and therefore had a speed limit of 60 km/h. The traffic density was low to high range and included large vehicles. The distance between the measurement vehicles reached 500 m, but was mostly around 50 m or around 230 m, with relative (Tx+Rx) speeds between 100 and 400 km/h as indicated in Fig. 7.1 and 7.2.

HOT - Highway Oncoming Traffic: 10 measurement runs. The measurement vehicles drove in a medium range traffic density with many large vehicles on the highway A10 between the exit Birkenwerder and the exit Muehlenbeck. The distance between vehicles was evenly distributed up to 570 m, with relative speeds between 250 and 330 km/h, as indicated in Fig. 7.1 and 7.2.

RCT - Rural Convoy Traffic: 7 measurement runs. The measurement vehicles drove on several roads west of Berlin: westbound on the road B5 between Staaken and Elstal (2 runs), southbound on the road L863 between Nauen and Ketzin (3 runs) and eastbound on the road L92/B273 between Paretz and Marquardt (2 runs). The traffic density was medium-range dense and during 4 of the measured runs, a large vehicle drove between the measurement vehicles and blocked the line-of-sight. The distance between the vehicles was mostly in the range 50-200 m, with

speeds between 80 and 200 km/h, as indicated in Fig. 7.1 and 7.2.

ROT - Rural Oncoming Traffic: 7 measurement runs. The measurement vehicles drove in a low range traffic density on the road L20 between Gross Glienicke and Seeburg. One of the measurement vehicles was driving at a distance of 5-20 m behind one of these large obstructing vehicles: large goods vehicle, coaches, large caravan, site vehicles of type Mercedes-Benz Actros 4146 and a van of type Volkswagen Type 2. The distance between vehicles was evenly distributed up to 550 m, with relative speeds mostly between 150 and 180 km/h, as indicated in Fig. 7.1 and 7.2. A detailed description of this scenario can be found in Chapter 11.

TCT - Tunnel Convoy Traffic: 4 runs in 3 different tunnels. Two of the measurement runs took place southbound in the so-called Tiergartentunnel, one measurement run took place northbound on the highway A111 below Gorkistr. and one measurement run northbound on the highway A111 next to the crossing Ruppiner Chaussee / Im Waldwinkel. We observed a medium to high range traffic density with several large vehicles. The measurements were conducted at several distances with emphasis on the ranges below 50 m, 150-250 m and around 420 m with relative speeds between 80 and 150 km/h, as indicated in Fig. 7.1 and 7.2.

UCT - Urban Convoy Traffic: 8 runs at 5 different measurement sites. One run took place eastbound on Skalitzerstr. between Kottbusser Tor and Wrangelstr. with a high traffic density and few large vehicles, one run northbound on Warschauerstr. between Oberbaumbruecke and Gruenbergerstr. with high traffic density and few large vehicles, one run westbound on Otto-Braun-Str. between Alexanderstr. and Niederwallstr. with low to high range traffic density and few large vehicles, two runs westbound on Leipzigerstr. between Axel-Springer-Str. and Mauerstr. with low to high range traffic density in driving direction and high traffic density in opposite driving direction and three runs westbound Buelowstr./Kleiststr. between Zietenstr. and Passauerstr. with medium to high range traffic including numerous large buses. Note that some runs were conducted next to elevated railways with numerous large metallic pillars at the height of the measurement antennas, which result in a rich and dynamic propagation environment. The distance between vehicles was usually 50 and 200 m, with relative speeds mostly between 60 and 80 km/h, as indicated in Fig. 7.1 and 7.2.

UOT - Urban Oncoming Traffic: 12 runs at 7 different measurement sites. One run took place on Strasse des 17. Juni between Ernst-Reuter-Platz and Kloppstr. with low to medium range traffic density and very few large vehicles, two runs on Knobelsdorffstr. between Sophie-Charlotte-Str. and Schloßstr. with low to medium range traffic density, two runs on Danckelmannstr. between Seelingstr. and Kaiserdamm with low traffic density and few large vehicles standing, two runs on Wilmersdorferstr. between Otto-Suhr-Allee and Bismarckstr. with low to medium range traffic density and several large vehicles standing, two runs on Schillerstr. between Leibnizstr. and Wilmersdorferstr. with low to medium range traffic density and few large vehicles, one run on Bleibtreustr. between Mommsenstr. and

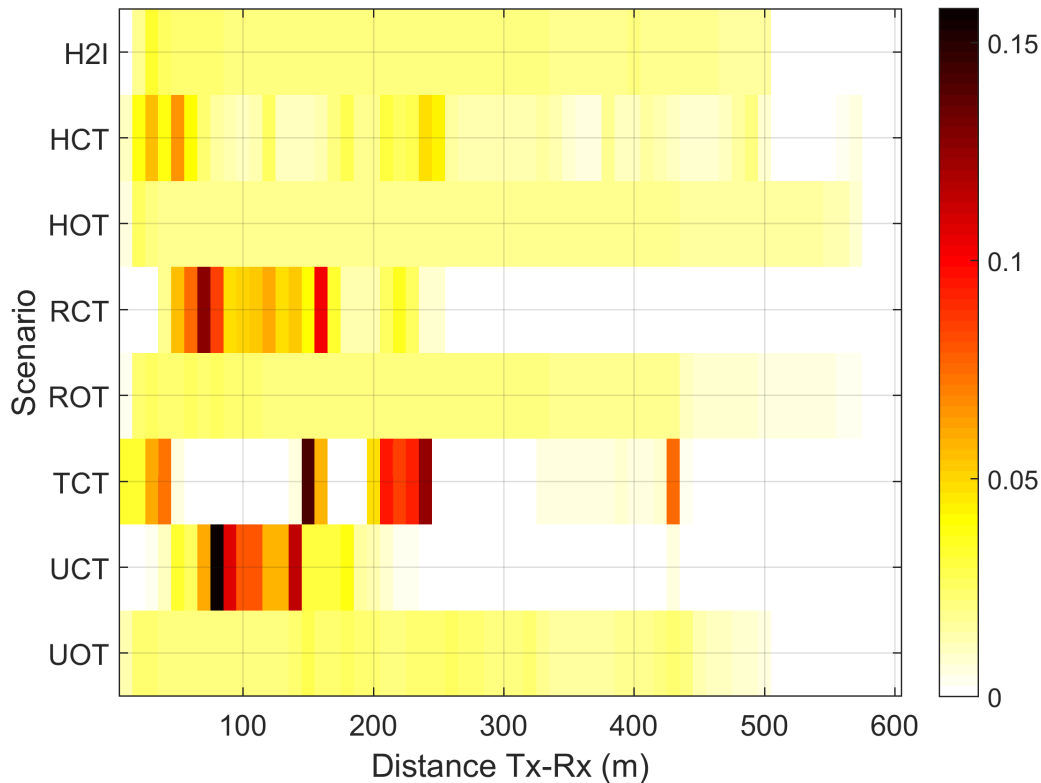


Figure 7.1: Histogram of distance between measurement vehicles during channel recording sets.

Pestalozzistr. with medium range traffic density and two runs on Hardenbergstr. between Joachimsthalerstr. and Ernst-Reuter-Platz with medium range traffic density and few large vehicles. The distance between vehicles was evenly distributed up to 500 m, with relative speeds between 5-100 km/h but mostly around 50 km/h, as indicated in Fig. 7.1 and 7.2.

7.2 MPC Parameter Extraction Methods

Processing of channel sounder data is a multi-step process and starts with an MPC detection, followed by a short-term MPC tracking and finally a long-term MPC tracking method. Here, the inter-tracking method (Section 6.5) is applied, due to the fact that the channel data is recorded according to the Type 2 in Table 4.1. This long-term tracking method interrelates MPC tracks across adjacent recording sets and gaps of 10-100 ms, as described in Section 6.5. For this algorithm, only full-lifetime MPCs are considered, i.e. MPC tracks with a lifetime equal to the

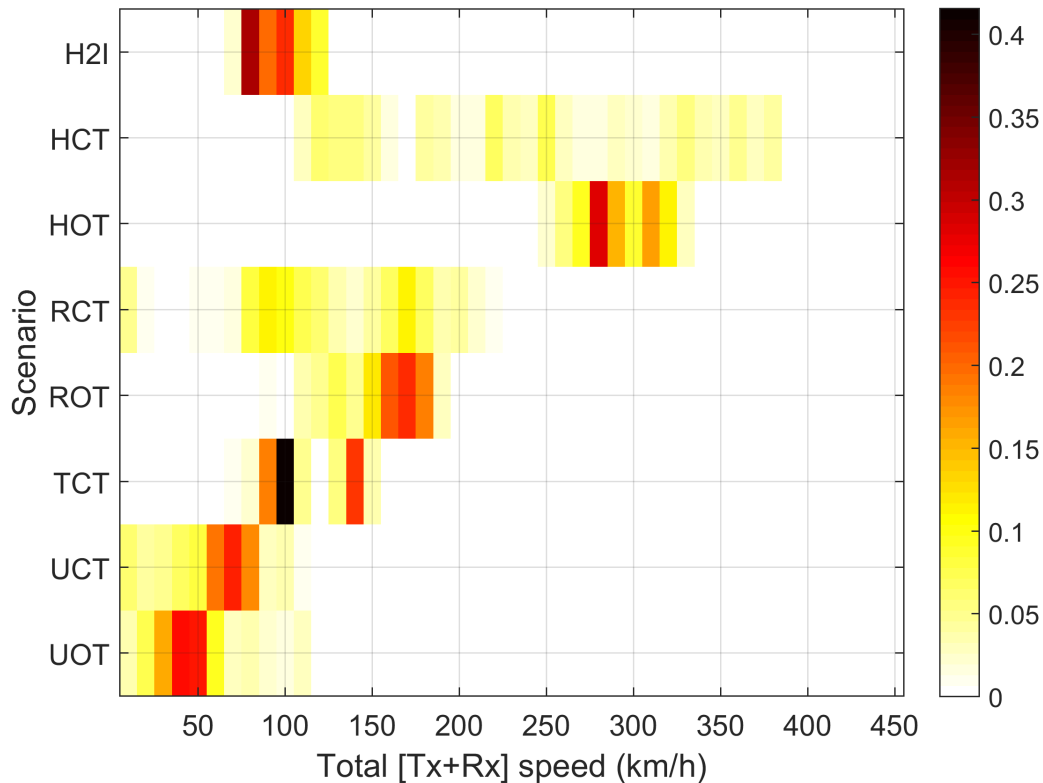


Figure 7.2: Histogram of relative vehicle speed during channel recording sets.

duration of the recording set. Excluding non-full-lifetime MPC tracks is based on the observation that tracks appearing or disappearing within the set recording time of 2.4-3.6 ms rarely lead to a MPC survival of 10 ms or more. Disregarding non-full-lifetime MPC tracks results in a power loss, but increases the reliability of the inter-tracking method.

The tracking parameters in Section 6.2 are matched to channel data from a TCT scenario with dense multipath inter-arrival times and a gap of 10 ms between adjacent recording sets. Here, we analyze channel data from various scenarios, where usually less dense multipath inter-arrival times occur and the set period intervals are in the range 10-100 ms. In order to apply the tracking algorithms on diverse scenarios, we doubled the delay threshold to $\chi = 2$ ns.

The applied short-term tracking method does not capture diffuse parts of the propagation channel, which leads to a certain power loss, as explained in Section 6.2. In addition, disregarding non-full-lifetime MPCs leads to a further power loss. For the channel data analyzed in this chapter we observe an average power loss of 2.2 dB due to the detection method and the short-term tracking, with values

ranging from 2.1 dB for ROT to 2.5 dB for UCT. The power loss due to the long-term tracking is on average 1.3 dB, ranging from 0.8 dB for TCT to 1.8 dB for RCT. The total power loss due to all processing steps is on average 3.5 dB, ranging from 2.9 dB for TCT to 3.9 dB for RCT.

7.3 Extracted Parameters

For a description of the five extracted and analyzed channel parameters, we start with the time-variant channel impulse response obtained from a wideband channel sounder

$$h(t, \tau) = \sum_{k=1}^{P(t)} a_k(t) e^{j\varphi_k} w(\tau - \tau_k(t)), \quad (7.1)$$

where a_k is the amplitude, φ_k the phase, τ_k the delay of MPC k and $w(\tau)$ the isolated channel sounder pulse. $P(t)$ is the number of MPCs at time t . Our channel data is discretized and we therefore translate the continuous form $h(t, \tau)$ to $h(iT_r, uT_b) = h[i, u]$, where T_r is the recording set period, $T_b = 1/B$ is the delay resolution period and B the measurement bandwidth of the channel sounder. More explanations on this discretization can be found in Section 6.1.

Now, similar to definitions in [25], we define three sets of MPCs:

- \mathcal{L}_i is the set of all MPCs that exist at time instance i and $P[i]$ is the number of MPCs at time instance i .
- $\mathcal{L}_{i \rightarrow i}$ is the set of MPCs that are firstly observed at time instance i , whose index of path is $k_{i \rightarrow i} = 1, 2, \dots, P_b[i]$. Hence, $P_b[i]$ is the number of newly observed MPCs at time instance i .
- $\mathcal{L}_{\Delta i}$ is the set of MPCs that are firstly observed during the time period $\Delta i = b - i$ and we designate $R[i]$ to be the total number of newly observed MPCs within this time period.

In order to obtain $R[i]$, we define

$$\Delta i \simeq \frac{\Delta s}{T_r(v_{Tx} + v_{Rx})}, \quad (7.2)$$

where $v_{Tx} + v_{Rx}$ is the current relative speed of the measurement vehicles and Δs is the traveled distance, set to be 1 m. Note that in order to maintain consistency among the scenarios, we exclude all data where the speed of one the measurement vehicles is below 5 km/h. Without this exclusion, we would obtain very high counts of newborn MPCs (newly observed MPCs) in case the vehicles are very slow

or standing. The total number of newborn MPCs within 1 m distance traveled is then found by

$$R[i] = P_b[i - b] + P_b[i - b + 1] + \dots + P_b[i] = \sum_{c=i-b}^i P_b[c]. \quad (7.3)$$

The inter-tracking method in Section 6.5 yields

$$\mathbf{q}_k[i] = \begin{pmatrix} \bar{a}_k[i] \\ \bar{\tau}_k[i] \\ \nu_k[i] \end{pmatrix}, \quad (7.4)$$

where $\bar{a}_k[i]$ is the mean amplitude, $\bar{\tau}_k[i]$ the mean delay and $\nu_k[i]$ the Doppler frequency of path k during the recording set at time instance i . Based on this result we define the set

$$\mathbf{Q}_k = \{\mathbf{q}_k[i]\}_{i=i_k^{start}}^{I_k}, \quad (7.5)$$

with i_k^{start} as the time instance where path k appears for the first time and I_k being the last time instance of this path. The lifetime of path k is $\Psi_k = I_k - i_k^{start}$. For a better geometrical relevancy, we translate the lifetime to distance with

$$Y_k = \Psi_k T_r (v_{Tx} + v_{Rx}). \quad (7.6)$$

The mean delay of a newborn MPC is $\bar{\tau}_b[i]$ with $b = 1, 2, \dots, P_b[i]$ and the excess delay of newborn MPCs therefore

$$\tau_b^x[i] = \bar{\tau}_b[i] - \tau_{LOS}[i], \quad (7.7)$$

where $\tau_{LOS}[i]$ is the delay of the line-of-sight path at time i .

The Doppler frequency ν_k is based on the delay change and estimated for each MPC track, as done in 6.30 and 6.31. Based on the Doppler frequency of newborn MPCs $\nu_b[i]$ with $b = \{1, 2, \dots, P_b[i]\}$, we define

$$\nu_b^n[i] = \frac{\nu_b[i]}{\frac{f_c}{c_o} (v_{Tx} + v_{Rx})} \quad (7.8)$$

as the relative Doppler frequency of newborn MPCs, where f_c is the carrier frequency and c_o is the speed of light. The relativization accounts for different speeds of the measurement vehicles and makes it feasible to merge measurement data with different speeds for an ensemble characterization per scenario. Again, we exclude data where the speed of any measurement vehicle drops below 5 km/h.

7.4 Number of MPCs

The number of MPCs $P[i]$ is an essential channel parameter and often modeled with the Poisson distribution

$$f(x|\lambda) = \frac{\lambda^x}{x!} e^{-\lambda}, x = 0, 1, 2, \dots, \infty, \quad (7.9)$$

where the single parameter λ influences both the mean and the variance of the distribution curve. We fit the cumulative density function (CDF) of the Poisson distribution to the measured data, together with a discretized Normal distribution fit for comparison. Both plots in Fig. 7.3 are from the same measurement run in an UOT scenario. The plot on the left-hand side was measured at a Tx-Rx distance of 450 m, whereas the plot on the right-hand side was measured at a distance of 80 m. In order to grasp this apparent distance dependency, we grouped the data into distance bins of 10 m width, computed the mean and the variance per bin and fitted a polynomial function

$$\lambda(d) = p_0 + p_1 d + p_2 d^2, \quad (7.10)$$

with d being the distance between Tx and Rx in meters. Note that $\lambda(d)$ becomes a line if p_2 is set to zero. As can be found in the left plot in Fig. 7.4, the UOT scenario exhibits a strong distance dependency. The mean standard deviation (STDEV) for this scenario is 1.82 and the mean square error (MSE) of the fitted line to the mean values is on average 0.604, as listed in Table 7.1. Most other scenarios show the same behavior with similar values and can be modeled with a linear characteristic of $\lambda(d)$. The strongest parabolic characteristics was found in the H2I scenario with a p_2 value of around 4. A rather exceptional behavior is found for scenario TCT on the right-hand side of Fig. 7.4, where the waveguiding effect of tunnels lead to a distance-*independent* Poisson parameter. The exceptionally high MSE values of the UCT scenario are due to high variances at distances below 200 m.

We conducted the goodness-of-fit χ^2 -test and an MSE estimation for both distribution functions. Due to the distance dependency, this was done per 10 m distance bin. The χ^2 -tests result in a null hypothesis rejection rate of 13.74% for the Poisson distribution and a rejection rate of 20.60% for the Normal distribution (5% significance level). The average MSE_N of the Poisson distribution fitting is $9.8 \cdot 10^{-3}$, ranging from $2.9 \cdot 10^{-3}$ for TCT to $13.9 \cdot 10^{-3}$ for HOT (see Table 7.4). The average MSE of the Normal distribution fit per distance bin is $1.41 \cdot 10^{-2}$, ranging from $0.31 \cdot 10^{-2}$ for TCT to $2.86 \cdot 10^{-2}$ for HOT. Hence, the Poisson distribution is a better choice both in terms of goodness-of-fit and accuracy.

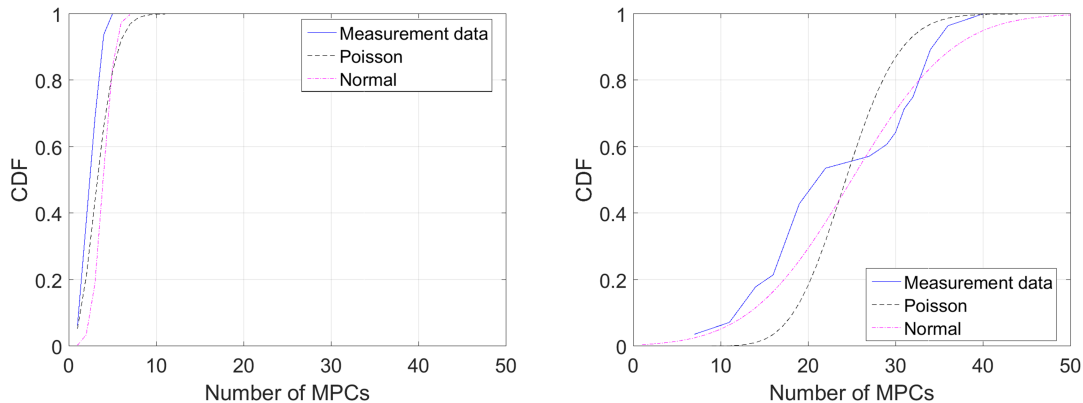


Figure 7.3: Comparison of number of MPCs distributions for an UOT measurement run at Tx-Rx distances of 450 m (left) and 80 m (right).

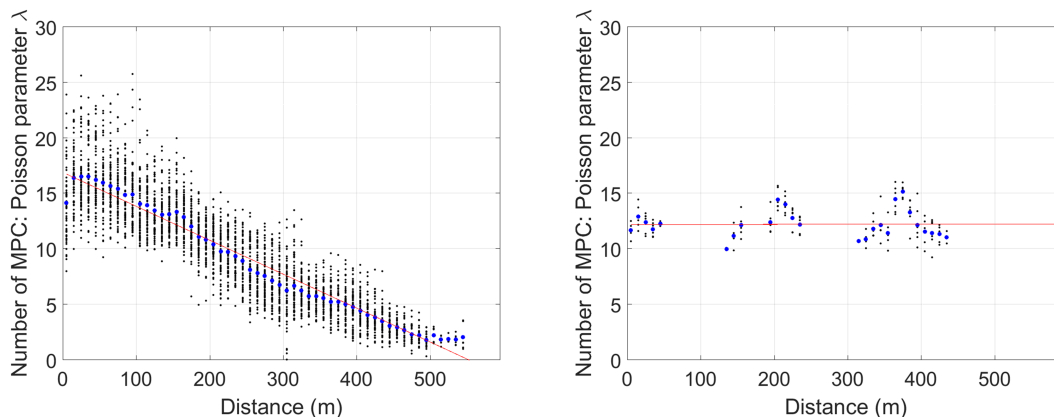


Figure 7.4: Distance dependence of the Poisson parameter λ for the number of MPCs in the UOT (left) and TCT (right) scenarios.

7.5 MPC Birth Rate

The birth rate $R[i]$ defined in (7.3) is the number of newborn MPCs per meter traveled and was found to have a similar distance dependency as $P[i]$. Consequently, we model $R[i]$ also with (7.9) and (7.10) and most scenarios exhibit a linear $\lambda(d)$ progression (see Table 7.2). Exceptional behavior is found again for the H2I scenario with a parabolic progression. The data for the TCT scenario is limited and the corresponding plot therefore sparse. Based on visual inspection, a constant value of approximately $\lambda = 7.5$ could also be appropriate for the TCT scenario, i.e. $p_0 = 7.5$ and $p_1 = p_2 = 0$.

The discretized Gamma distribution yields a good fit and was therefore included for comparison. The results from an UOT measurement run in Fig. 7.5 display

Table 7.1: Number of MPCs parameters.

Scenario	STDEV	p_0	p_1	p_2	MSE
H2I	2.08	18.9	$-5.37 \cdot 10^{-2}$	3.99	1.101
HCT	1.63	10.2	$-1.62 \cdot 10^{-2}$	0	0.587
HOT	0.92	7.97	$-2.14 \cdot 10^{-2}$	$1.54 \cdot 10^{-5}$	0.197
RCT	1.38	9.73	$-1.70 \cdot 10^{-2}$	0	0.443
ROT	1.62	7.11	$-0.95 \cdot 10^{-2}$	0	0.196
TCT	0.87	12.2	0	0	1.612
UCT	1.69	14.5	$-2.61 \cdot 10^{-2}$	0	6.281
UOT	1.82	16.9	$-3.05 \cdot 10^{-2}$	0	0.604

a significant difference between the two empirical CDFs, which were recorded at distances of 290 m and 270 m. The example shows that the birth rate behavior in this scenario has a large variance and can change rapidly. We merge data from 12 runs at seven different measurement sites and see in the right-hand plot in Fig. 7.6 that the birth rate in the UOT scenario has a two-fold behavior. Similar to other scenarios, the progression above 300 m decreases with increased distance. However, the behavior is reversed for distances below 300 m. We compared each single UOT measurement run and observe this increasing-decreasing nature in all runs, however with varying widths and location of the maximum value.

The χ^2 -tests and MSE estimations were again performed per 10 m distance bin. The χ^2 -tests result in a null hypothesis rejection rate of 8.82% for the Poisson distribution and a rejection rate of 16.15% for the Gamma distribution. The average MSE_B of the Poisson distribution fitting is $7.2 \cdot 10^{-3}$, ranging from $1.4 \cdot 10^{-3}$ for TCT to $13.5 \cdot 10^{-3}$ for H2I (see Table 7.4). The average MSE of the Gamma distribution fitting per distance bin is $2.94 \cdot 10^{-2}$, ranging from $0.24 \cdot 10^{-2}$ for TCT to $11.9 \cdot 10^{-2}$ for HOT. Hence, the Poisson distribution is again a better choice both in terms of goodness-of-fit and accuracy.

7.6 MPC Lifetime

Finding a suitable distribution function for the MPC lifetime Y_k defined in (7.6) appears to be problematic. We did not observe a distance dependency or any significant indications on a mixture distribution, i.e. a separation of shorter lifetime from longer lifetime MPCs with different thresholds did not improve the results. We fitted the Gamma, log-normal, Weibull and Inverse Gaussian distribution, but

Table 7.2: Birth rate parameters.

Scenario	STDEV	p_0	p_1	p_2	MSE
H2I	1.59	15.8	$-5.45 \cdot 10^{-2}$	5.21	0.579
HCT	1.18	7.26	$-1.25 \cdot 10^{-2}$	0	0.344
HOT	0.58	5.26	$-1.77 \cdot 10^{-2}$	$1.58 \cdot 10^{-5}$	0.0745
RCT	1.06	6.90	$-1.25 \cdot 10^{-2}$	0	0.231
ROT	1.22	3.49	$-0.34 \cdot 10^{-2}$	0	0.258
TCT	0.61	9.82	$-0.61 \cdot 10^{-2}$	0	2.54
UCT	2.40	13.8	$-2.86 \cdot 10^{-2}$	0	12.78
UOTA	4.90	41.1	$-6.93 \cdot 10^{-2}$	0	2.004
UOTB	8.24	$9.01 \cdot 10^{-1}$	$6.13 \cdot 10^{-2}$	0	2.878

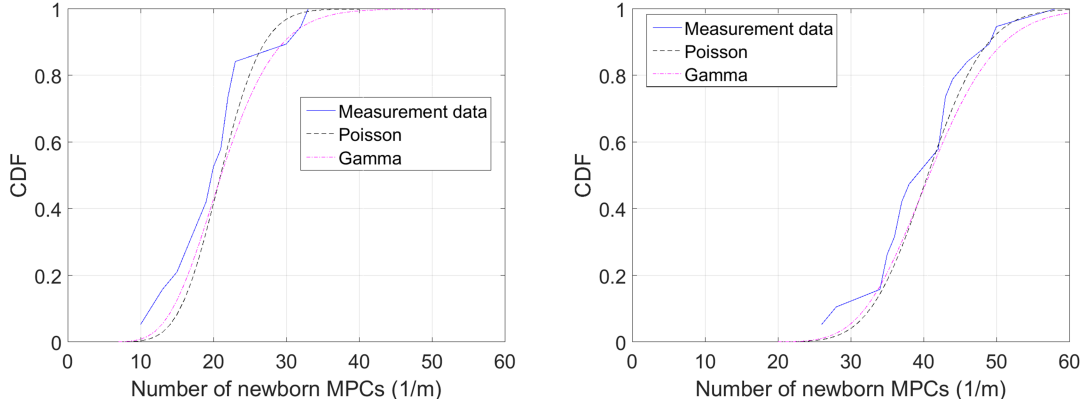


Figure 7.5: Comparison of birth rate distributions for an UOT measurement run at Tx-Rx distances of 290 m (left) and 270 m (right).

finally selected the Birnbaum-Saunders distribution

$$\begin{aligned}
 f(x|\eta, \gamma) &= \frac{1}{\sqrt{2\pi}} \left(\frac{\left(\sqrt{x/\eta} - \sqrt{\eta/x} \right)}{2\gamma x} \right) \\
 &\cdot \exp \left\{ -\frac{\left(\sqrt{x/\eta} - \sqrt{\eta/x} \right)^2}{2\gamma^2} \right\}, x > 0
 \end{aligned} \tag{7.11}$$

as the best choice, where η affects the scale and γ the shape of the curve. We identify the log-normal distribution as the best alternative and compare the fitting results. The left plot in Fig. 7.7 shows the *worst* encountered fitting results for an HCT measurement run, where the fitting errors are predominantly found for

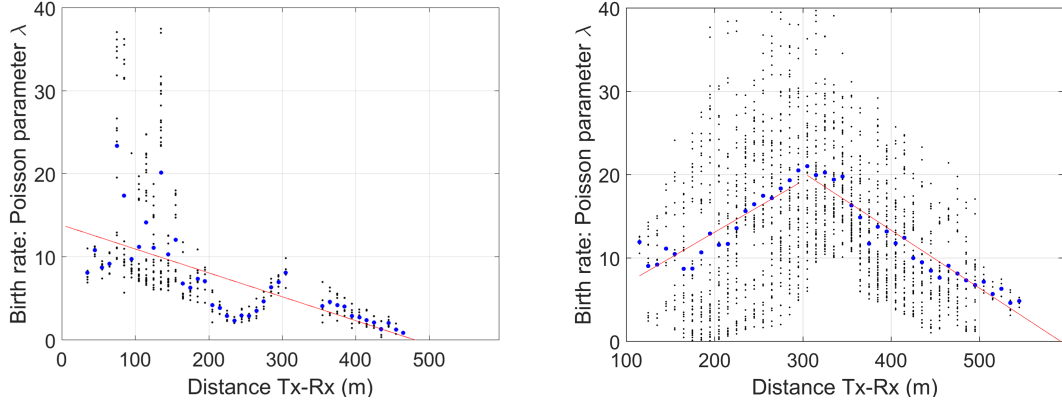


Figure 7.6: Distance dependent progression of Poisson parameter λ for birth rate distributions in UCT (left) and UOT (right) scenarios.

larger values. The fitting result improves if applied on an entire scenario data set, as shown for the HOT in the right-hand plot in Fig. 7.7. Nevertheless, the fitted distribution still deviates significantly from the empirical curve, whereas it captures the essential behavior. Consequently, the χ^2 -tests yield a rejection rate of 99.31% for the Birnbaum-Saunders distribution and a rejection rate of 100% for the log-normal distribution. The average MSE_L of the Birnbaum-Saunders distribution fitting per measurement is $2.0 \cdot 10^{-3}$, ranging from $0.95 \cdot 10^{-3}$ for TCT to $2.7 \cdot 10^{-3}$ for H2I (see Table 7.4). The average MSE of the Lognormal distribution fitting per measurement is $1.5 \cdot 10^{-3}$, ranging from $0.5 \cdot 10^{-3}$ for TCT to $2.8 \cdot 10^{-3}$ for HOT. The average MSE of the Birnbaum-Saunders distribution fitting per scenario is $0.87 \cdot 10^{-3}$, ranging from $0.40 \cdot 10^{-3}$ for TCT to $1.4 \cdot 10^{-3}$ for HCT. The average MSE of the Lognormal distribution fitting per scenario is $5.96 \cdot 10^{-4}$, ranging from $0.77 \cdot 10^{-4}$ for TCT to $16 \cdot 10^{-4}$ for HCT. The distribution of all estimated Birnbaum-Saunders parameters is displayed in Fig. 7.8, where large markers indicate the parameters of the overall fit per scenario. We observe the shortest lifetime in urban or tunnel scenarios and the longest lifetime convoy traffic scenarios, in particular the HCT scenario. The parameter values for all scenarios can be found in Table 7.3.

7.7 Excess Delay of Newborn MPCs

The excess delay $\tau_b^x[i]$, defined in (7.7), was found to be non-distance-dependent and is modeled with the log-normal distribution

$$f(x|\psi, \rho) = \frac{1}{x\rho\sqrt{2\pi}} \exp\left\{-\frac{(\ln x - \psi)^2}{2\rho^2}\right\}, x > 0. \quad (7.12)$$

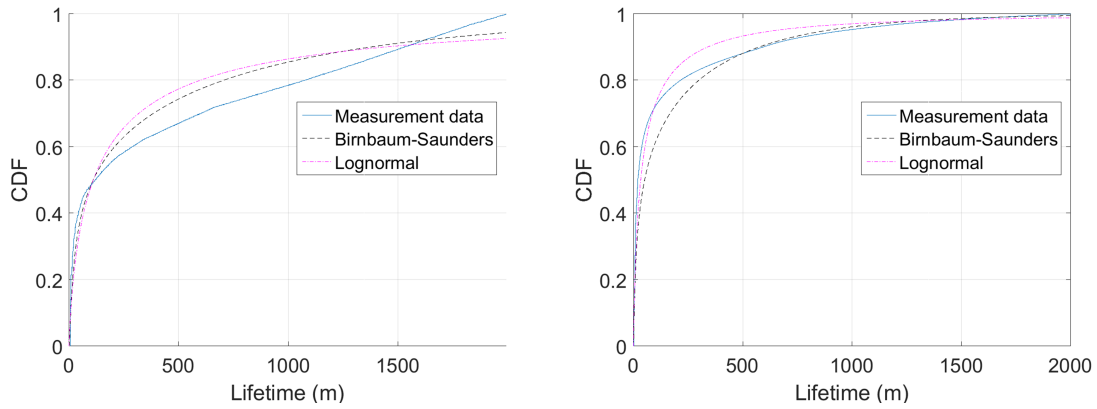


Figure 7.7: Comparison of lifetime distributions based on a single HCT measurement run (left) and all data within HOT scenario (right).

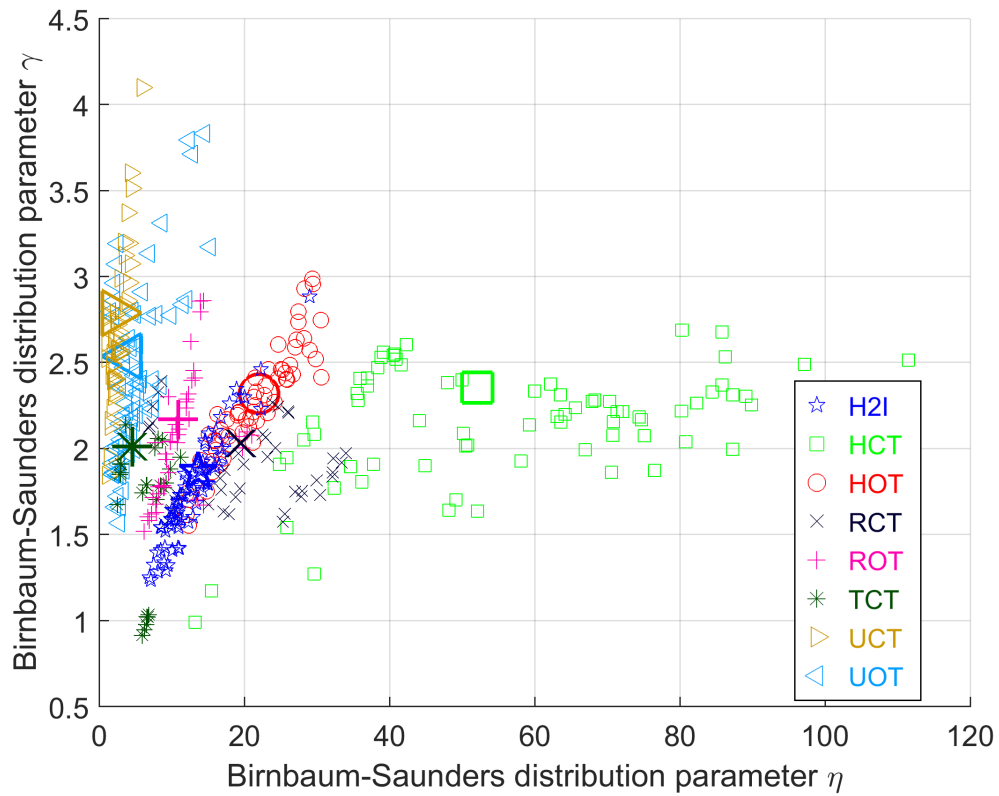


Figure 7.8: Distribution of Birbaum-Saunders parameters for lifetime occurrences per measurement (small marker) and per scenario (large marker).

The parameter ψ defines the peak location, whereas the parameter ρ scales the curve. This distribution function yields a comparatively good fit, except for the scenario H2I. The large MSE value of $32 \cdot 10^{-4}$ in Table 7.4 is due to the fact that most runs in this scenario revealed two cores of excess delay occurrences. While most observed delay values are close to 0 ns, 5-30% of the delays occurred at values of 300-350 ns. This is probably due to scattering at the buildings surrounding the infrastructure antenna and could be modeled with a mixture distribution. Since this issue of near and distant delay occurrences was only observed in the H2I scenario and a few urban measurement runs, we decided for simpler two-parameter distribution functions for the modeling.

In addition to the log-normal distribution, we fitted an exponential distribution and found that the χ^2 -tests per measurement run result in a null hypothesis rejection rate of 80.56% for the log-normal distribution and a rejection rate of 79.17% for the exponential distribution. We also conducted a Kolmogorov-Smirnov test (KS) and found that the rejection rates of the log-normal and exponential distributions are 87.27% and 98.38%, respectively. The average MSE_E of the log-normal distribution fitting per measurement is $1.1 \cdot 10^{-3}$, ranging from $0.36 \cdot 10^{-3}$ for UOT to $32 \cdot 10^{-3}$ for H2I (see Table 7.4). The average MSE of the exponential distribution fitting per measurement is $5.3 \cdot 10^{-3}$, ranging from $2.2 \cdot 10^{-3}$ for UCT to $10.7 \cdot 10^{-2}$ for H2I. The average MSE of the log-normal distribution fitting per scenario is $7.05 \cdot 10^{-4}$, ranging from $0.73 \cdot 10^{-4}$ for UCT to $32 \cdot 10^{-4}$ for H2I. The average MSE of the exponential distribution fitting per scenario is $4.2 \cdot 10^{-3}$, ranging from $1.0 \cdot 10^{-3}$ for UCT to $10.4 \cdot 10^{-3}$ for H2I.

The goodness-of-fit test rates suggest slightly an advantage for the log-normal distribution, but essentially suggest a rejection of both distribution hypothesis. The exponential distribution is better in terms of convergence of the CDF towards 1 within the observed value range, which prevents the model from generating undesired very long excess delays. The fitting per measurement is more accurate with log-normal distributions, whereas the fitting per scenario is a little more accurate with exponential distributions, mainly due to better fits in the H2I scenario. The selection of log-normal is based on a better overall accuracy and slightly better goodness-of-fit test results. The distribution of the observed log-normal parameters in Fig. 7.9 indicate larger excess delays in the urban scenarios and smaller excess delays in rural scenarios (see also Table 7.3).

7.8 Relative Doppler frequency of Newborn MPCs

The relative Doppler frequency of newborn MPCs $\nu_b^n[i]$ defined in (7.8) is modeled with the Weibull distribution

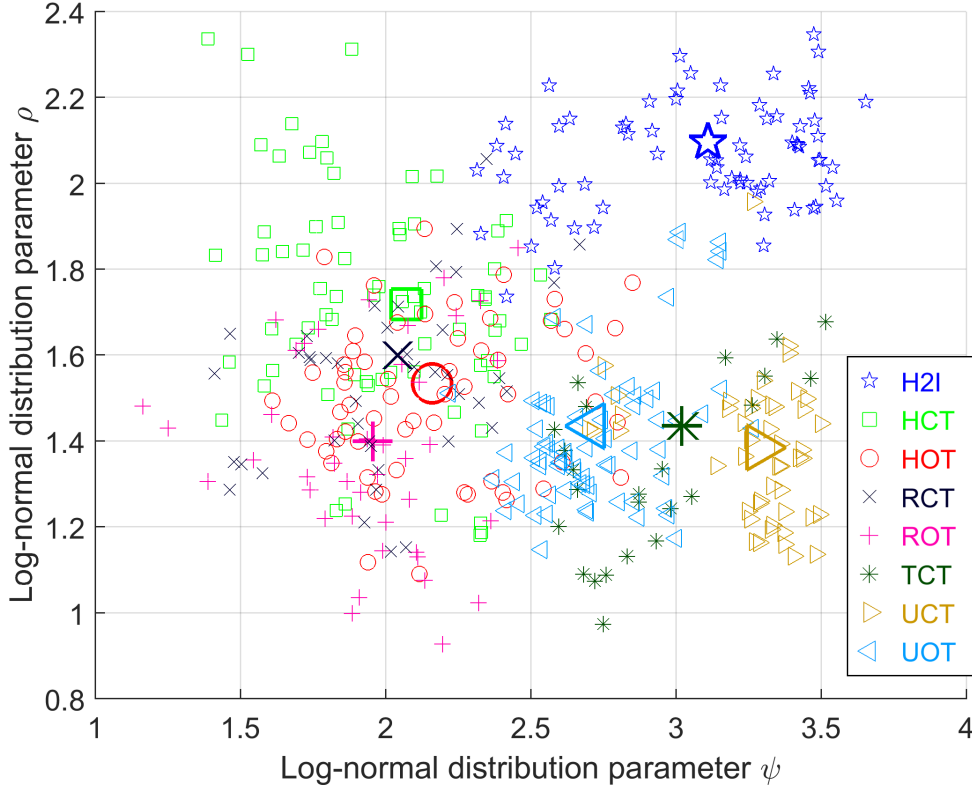


Figure 7.9: Distribution of log-normal parameters for excess delay occurrences per measurement (small marker) and per scenario (large marker).

$$f(x|\zeta, \kappa) = \frac{\kappa}{\zeta} \left(\frac{x}{\zeta}\right)^{\kappa-1} \exp\left\{-\left(\frac{x}{\zeta}\right)^{\kappa}\right\}, x > 0. \quad (7.13)$$

The parameter ζ determines the scale and the parameter κ the shape of the curve. For the HOT measurement run in the left plot in Fig. 7.10, the Weibull distribution has a slightly better fit than the alternative Gamma distribution. Both distributions fit very well in an UOT scenario, as can be seen in the right plot in Fig. 7.10. The measurement runs in Fig. 7.10 were selected as examples for fitting results, because they show that the Weibull distribution is suitable even for extreme values found within the parameter distribution in Fig. 7.11, i.e. the HOT run is fitted with $\zeta = 1.01$ and $\kappa = 5.42$, whereas UOT is fitted with $\zeta = 1.55$ and $\kappa = 1.31$.

The χ^2 -tests result in a null hypothesis rejection rate of 91.67% for the Weibull distribution and a rejection rate of 86.34% for the Gamma distribution. The KS-tests revealed rejection rates of 62.50% and 76.62% for the Weibull and Gamma distributions respectively. The average Weibull MSE_D is $8.2 \cdot 10^{-4}$, ranging from

Table 7.3: Parameters of lifetime, excess delay and relative Doppler.

Scenario	η	γ	ψ	ρ	ζ	κ
H2I	13.62	1.867	3.110	2.096	1.041	2.679
HCT	52.07	1.355	2.071	1.718	0.152	0.910
HOT	22.01	2.319	2.160	1.534	0.993	3.517
RCT	19.52	2.031	2.041	1.600	0.289	0.862
ROT	10.87	2.169	1.955	1.399	1.061	2.650
TCT	4.554	2.011	3.021	1.435	0.414	1.013
UCT	2.248	2.789	3.288	1.385	1.134	1.051
UOT	3.999	2.539	2.709	1.435	1.317	1.306

$0.95 \cdot 10^{-4}$ for UCT to $20 \cdot 10^{-4}$ for HOT (see Table 7.4). The average Gamma MSE is $2.1 \cdot 10^{-3}$, ranging from $0.12 \cdot 10^{-3}$ for UCT to $7.2 \cdot 10^{-3}$ for HOT. The Weibull MSE per scenario is $5.80 \cdot 10^{-4}$, ranging from $0.03 \cdot 10^{-3}$ for UCT to $1.6 \cdot 10^{-3}$ for HOT. The Gamma MSE per scenario is $1.6 \cdot 10^{-3}$, ranging from $0.03 \cdot 10^{-3}$ for UCT and $6.2 \cdot 10^{-3}$ for HOT.

The distribution of the Weibull parameters in Fig. 7.11 reveals a distinctive characteristic and encourages the definition of three groups (see Table 7.3):

1. the urban traffic group (UCT, UOT) in the lower right corner in Fig. 7.11 is characterized by a curved CDF-shape and relative Doppler frequency values of up to 5 (right plot in Fig. 7.10)
2. the convoy traffic group (HCT, RCT, TCT) in the lower left corner in Fig. 7.11 is also characterized by a curved CDF-shape, however with lower values up to 2
3. the oncoming traffic group (H2I, HOT, ROT) in the upper part in Fig. 7.11 is characterized by a s-shaped CDF curve around the value 1 (left plot in Fig. 7.10)

For accurate modeling of channel properties in vehicular communication scenarios it is important to understand the behavior of MPCs. In this chapter, we have modeled the number of MPCs and the birth rate of MPCs with a distant-dependent Poisson distribution and we found exceptional behavior for the tunnel and urban scenarios. The statistical characterization of MPC lifetime appears still unclear, while the distribution of excess delay and relative Doppler frequency of individual MPCs are modeled accurately. The obtained statistical distributions can be used for a parametrization of suitable channel models and lead ultimately to a more accurate reproduction in V2V channel simulations.

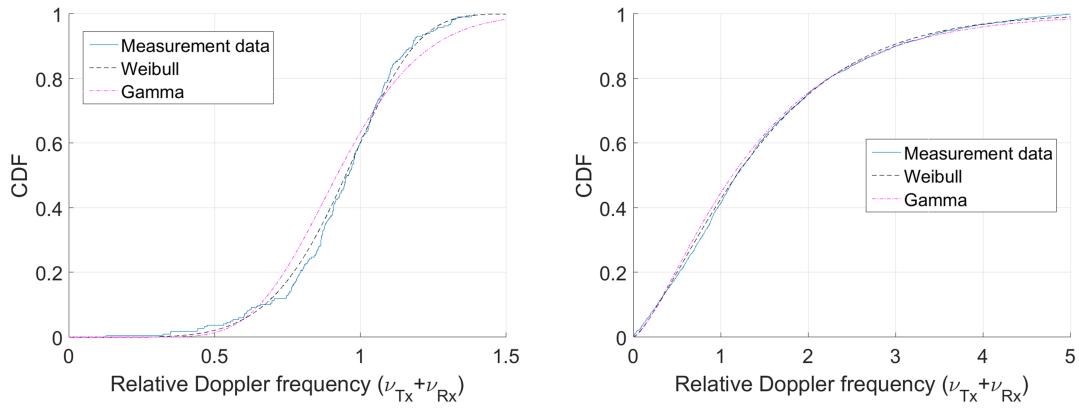


Figure 7.10: Comparison of relative Doppler distributions for measurement runs in scenarios HOT (left) and UOT (right).

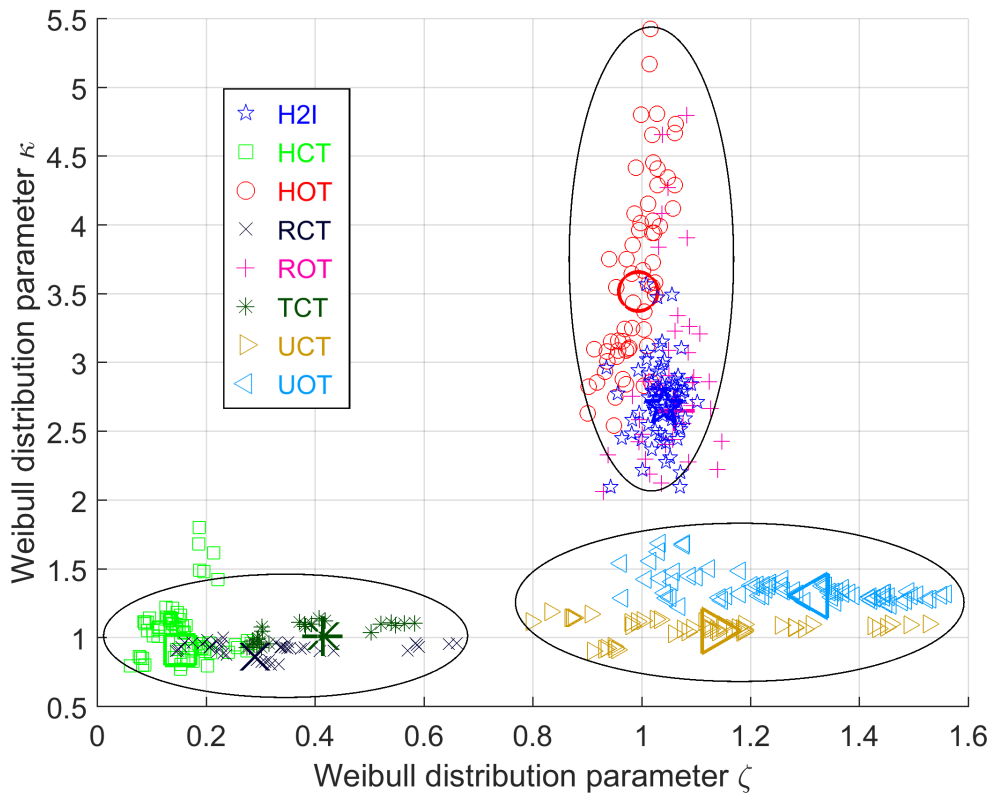


Figure 7.11: Distribution of Weibull parameters for relative Doppler occurrences per measurement (small marker) and per scenario (large marker).

Table 7.4: Mean square error of distribution fits.

Scenario	MSE_N	MSE_B	MSE_L	MSE_E	MSE_D
H2I	$1.84 \cdot 10^{-2}$	$1.35 \cdot 10^{-2}$	$2.7 \cdot 10^{-3}$	$34 \cdot 10^{-4}$	$14 \cdot 10^{-4}$
HCT	$0.96 \cdot 10^{-2}$	$0.61 \cdot 10^{-2}$	$1.9 \cdot 10^{-3}$	$7.3 \cdot 10^{-4}$	$8.6 \cdot 10^{-4}$
HOT	$1.39 \cdot 10^{-2}$	$0.70 \cdot 10^{-2}$	$1.6 \cdot 10^{-3}$	$6.2 \cdot 10^{-4}$	$20 \cdot 10^{-4}$
RCT	$0.51 \cdot 10^{-2}$	$0.34 \cdot 10^{-2}$	$1.7 \cdot 10^{-3}$	$5.7 \cdot 10^{-4}$	$3.1 \cdot 10^{-4}$
ROT	$1.61 \cdot 10^{-2}$	$0.89 \cdot 10^{-2}$	$2.4 \cdot 10^{-3}$	$7.5 \cdot 10^{-4}$	$11 \cdot 10^{-4}$
TCT	$0.29 \cdot 10^{-2}$	$0.14 \cdot 10^{-2}$	$0.9 \cdot 10^{-3}$	$17 \cdot 10^{-4}$	$5.5 \cdot 10^{-4}$
UCT	$0.41 \cdot 10^{-2}$	$1.08 \cdot 10^{-2}$	$2.3 \cdot 10^{-3}$	$4.5 \cdot 10^{-4}$	$0.9 \cdot 10^{-4}$
UOT	$0.82 \cdot 10^{-2}$	$0.61 \cdot 10^{-2}$	$2.7 \cdot 10^{-3}$	$3.6 \cdot 10^{-4}$	$1.8 \cdot 10^{-4}$
Mean	$0.98 \cdot 10^{-2}$	$0.72 \cdot 10^{-2}$	$2.0 \cdot 10^{-3}$	$11 \cdot 10^{-4}$	$8.1 \cdot 10^{-4}$

8 Scatterers at Urban Intersections

Urban intersections constitute an important safety-critical scenario for vehicle-to-vehicle communication. Since vehicular communication systems are predominantly envisioned in the 6 GHz band, propagation through massive obstructing objects is not possible and radio communication solely depends on scattering objects at and around intersections. In order to enhance vehicular communication at intersections, researchers focus on a better understanding of the communication at urban intersections and its underlying radio propagation process.

Related work was done in [22], where radio channels at street intersections were measured and channel properties characterized, whereas [50] compared radio channel properties between merging lanes and urban intersections. Both [22] and [50] showed that scattering objects in and around an intersection can account for a considerable part of the total received power. An analysis of building positioning at street intersection and corresponding clusters of representative intersection scenarios were presented in [51]. NLOS path-loss and fading model at street intersections were presented in [52] and [53]; the validity of the model in [52] was studied in [54]. Channel measurements at different intersection types with typical power delay profiles, pathloss and delay spreads are presented in [22]. It is shown that communication under NLOS conditions is problematic, but that roadside buildings can create important propagation paths. The scattering objects of the discrete MPCs were determined by drawing a scattering ellipse corresponding to the MPC delay at several time instances. A directional analysis of MPC in different scenarios, including an urban intersection, is introduced in [55]. It is found that in the absence of LOS, first-order reflections from a small number of scattering objects can account for a large part of the received power. Radio channel measurements are also being used for a validation of propagation models and simulations. Channel sounder data in [56] are aligned with results from a ray tracer by comparing channel gain and power delays profiles. Further, channel measurement results in [54] are compared with a propagation model derived in [52]. For a further improvement of the model, the authors of [54] suggest to include the number of and properties of the available scatterers at the specific intersection into the model.

8.1 Manual Localization of Scatterers

8.1.1 Measurement Setup and Data

This section presents detailed investigations of the radio wave propagation processes in a typical urban intersection. We focus on one time instance of the propagation process and set up hypothesis for locations of the scattering objects.

The position of the measurement vehicles is recorded with the GeneSys ADMA-G positioning system, which works reliably even in deep street canyons, where coverage of GNSS satellites is limited. The measurements were conducted in Berlin at the crossing of Pestalozzistr. and Schlueterstr.; more details and GNSS coordinates can be found in Table 10.1. This crossing is a 4-leg intersection with street widths of 21 m on the east-west street and 33 m on the north-south street. All four corners have buildings relatively close to the intersection center, a communication scenario that accounts for about 50% of German urban intersections according to [51]. The two corners on the east-side of the intersection have a regular rectangular shape, while the two corners on the west-side are truncated with a 45°-wall of around 4 m length. On the sidewalk in front of each building corner, there are on average three traffic signs that could act as scattering objects.

Naturally, two vehicles on collision course will at some point see each other and change from NLOS to the LOS. Since communication under LOS conditions yields a very high PDR and also the operability of other complementary vehicular sensors, we only consider the NLOS phase and take the NLOS/LOS transition line as our reference point. In Fig. 8.1 the transition line for each vehicle trajectory is marked as 0 m, while -30 m marks the distance to this reference point. The distance between the NLOS/LOS transition line and the crossing center is 32-38 m for the north-south road and 22-27 m for the east-west road. In order to validate the accuracy of the positioning system, we extract the strongest path under LOS condition (the measurement phase we disregarded for our results), translated the path delay into meters and compared the results to the ADMA positioning system results. A maximum difference of 2 m could be observed between the two independent systems, which gave us confidence in the accuracy of the positioning results. In order to avoid a complicated analysis w.r.t. the two-dimensional distance, as done in Chapter 10, to the NLOS/LOS transition line, we select measurement runs with similar speeds and similar distances to the center of the intersection for both vehicles and use the mean distance of both vehicles for further analysis. Fig. 8.1 shows an overview of the two investigated measurement runs: run A with the transmitter driving from the north towards the intersection and measurement run B with the transmitter coming from the south. The average vehicle speed was 30-38 km/h, i.e. around 10 m/s.

8.1.2 Results for Manual Localization of Scatterer

For the analysis of scattering points we focus on the propagation process at 30 m distance, a phase which can be viewed as a region where communication starts with a PDR level of around 50% for 802.11p systems (see Fig. 10.5). We take the delay time of the MPCs for both measurement runs (A1-A4 in Fig. 8.2 and B1-B4 in Fig. 8.3), computed the corresponding MPC travel distance and use a GoogleEarth™ tool called Path Ruler to test propagation hypothesis (lower left corner in Fig. 8.1). This method is basically equivalent to drawing a scattering ellipse. The visibility limitations for single-bounce reflections (dashed line in Fig. 8.1) led to the hypothesis of scatterer position A1, A3 and B1-B3 in Fig. 8.1. The possible scatterer positions of B1-B3 are straightforward and it can be observed that an MPC with a delay time larger than B3 has to be a double-bounce reflection path. The most likely path for B4 is a reflection at the north-west truncated corner and a second reflection at an object on the eastern part of the intersection as indicated with the continuous arrow in Fig. 8.1. The travel distance of A1 fits very well with the position of the south-west corner of the intersection. The most likely path for A2 is a double bounce reflection with incident angles equal to emergent angles at the eastern wall of the north-south road and the southern wall of the east-west road. This hypothesis is also supported by the delay dispersion in Fig. 8.2. The travel distance of A4 leads to a similar propagation path hypothesis as for B4, but mirrored on the east-west axis: a first reflection at point A1 and a second reflection at a scattering object in the eastern part of the intersection.

8.2 Semi-automated Localization of Scatterers

8.2.1 Wideband Delay Characteristics and Scatterer Properties

The sparsity of wideband channel data makes it feasible to distinguish individual MPC tracks, which is the prerequisite for a association of measured MPCs to their corresponding scattering sources. In addition to this essential property, the wideband channel data reveals unique MPC delay profile characteristics. The characteristic of a delay progression depends on the properties of a corresponding scattering object. Hence, a detailed understanding of the MPC delay characteristics can be highly beneficial, since it allows the verification or falsification of an association made between an MPC track and a scattering source. The combined delay progressions of the four MIMO channels (11, 12, 21 and 22) in Fig. 8.4 show several interesting insights. The groups of MPC tracks at the upper and lower part of the plot exhibit a fairly disordered behavior, whereas the two track groups in the center of the plot are better defined. For clearly defined MPC tracks, the delay

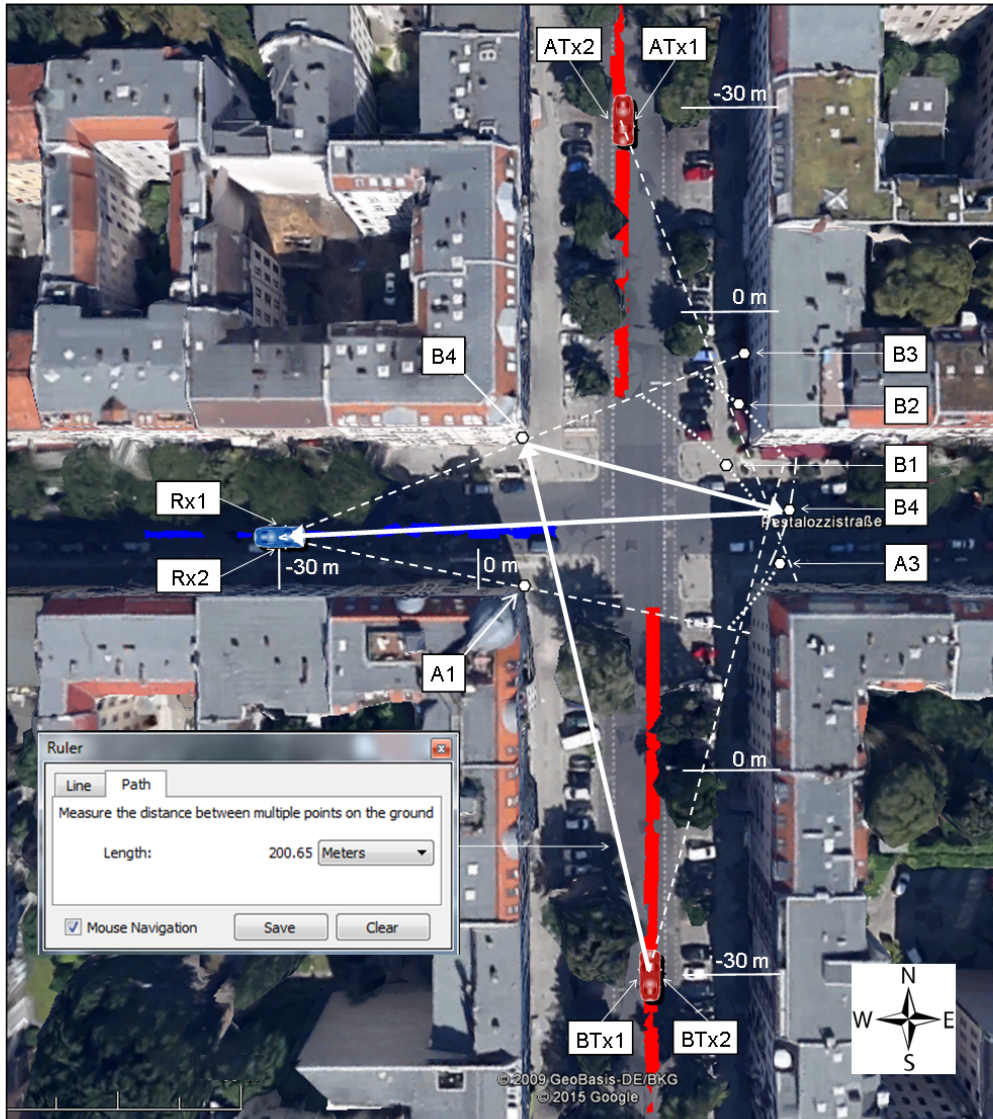


Figure 8.1: Overview of measurement runs and hypothesis of scatterer positions.

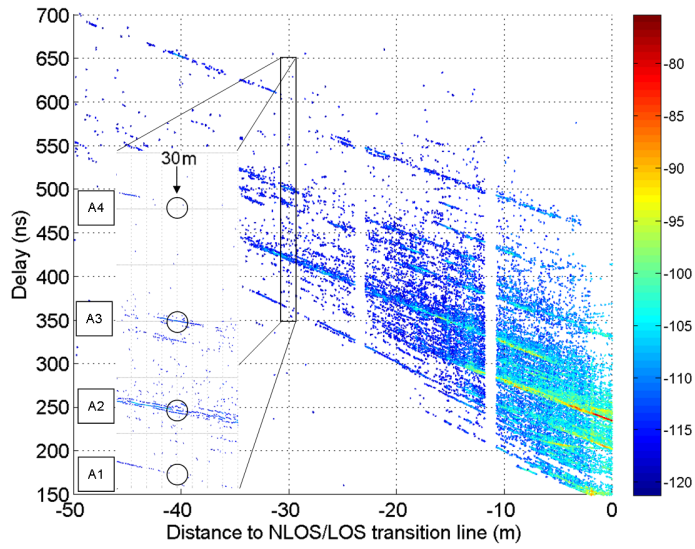


Figure 8.2: Delay of MPCs vs. distance of MIMO channel Tx1Rx1 in measurement run A (ATx1 to Rx1 in Fig. 8.1).

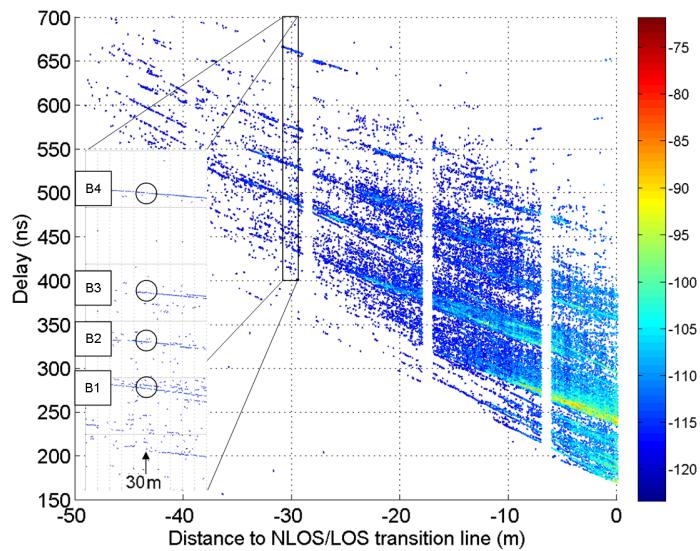


Figure 8.3: Delay of MPCs vs. distance of MIMO channel Tx2Rx1 in measurement run B (BTx2 to Rx1 in Fig. 8.1).

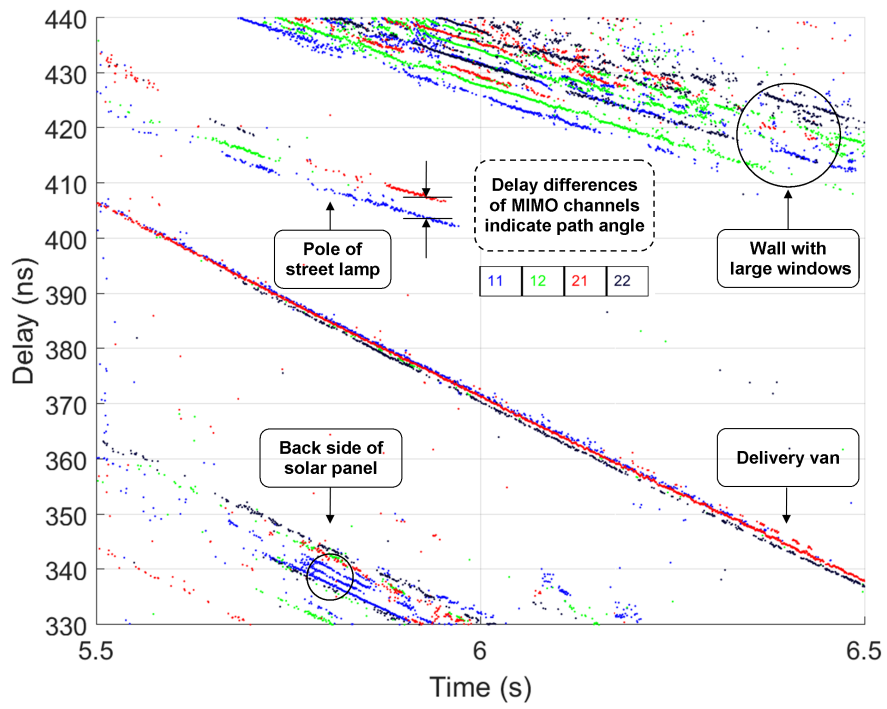


Figure 8.4: Delay characteristics of MPC tracks for different MIMO channels.

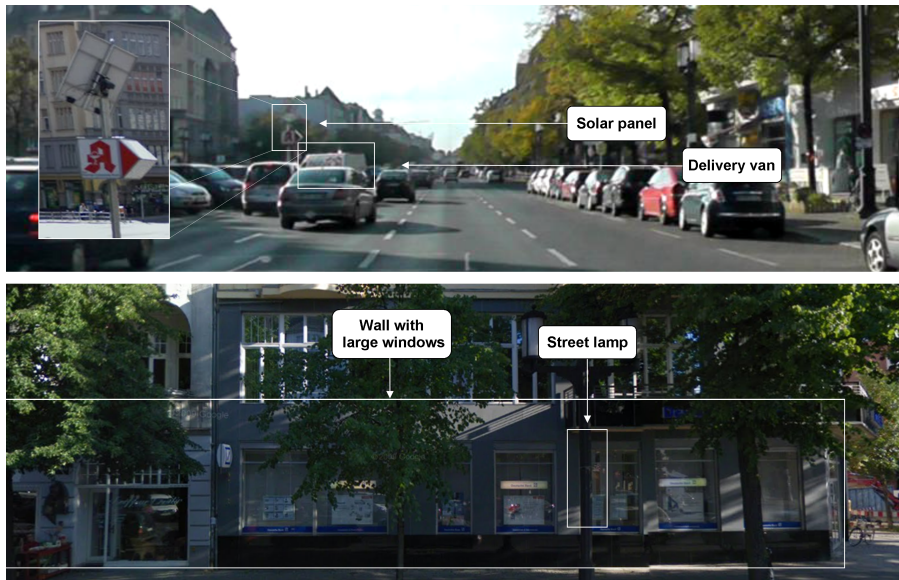


Figure 8.5: Scattering objects at investigated urban intersection.

differences from different MIMO channels give a good indication of the path angle (AOA or AOD). For example, the MPC tracks associated to the street lamp exhibit a delay difference of approximately 4 ns between MIMO channel 11 and 21. This delay difference in combination with a distance of 1.3 m between the Tx vehicle roof antennas leads to a path angle of approximately 65° left of the Tx direction of movement. This is in well accordance with the geometry at this time instance, as can be seen in Fig. 8.6. Furthermore, we can see in Fig. 8.4 that the slope of the tracks associated to the van or the solar panel are steeper compared to the slope of street lamp or wall. This relates also very well to the geometry in Fig. 8.6, where the steeper slopes (the higher Doppler shifts) coincide with a smaller angle between the scattering objects and the direction of movement. Based on estimates of delay, Doppler, path angle and the delay characteristic, MPC tracks can be associated to corresponding scattering sources with high trustworthiness. For instance, the flat surface of a delivery van (see Fig. 8.5 and Fig. 8.6) fits very well with an approximately linear MPC delay progression and the lifetime of more than 1 s in Fig. 8.4. Similarly, a street lamp pole leads to a linear MPC delay evolution, but with a significantly shorter lifetime. These types of delay characteristics can be described as linear MPC track. Quite differently, reflections on house walls result in a turbulent delay characteristic, due to the fact that the wall interaction involves numerous parts of the house wall, including doors, windows and different types of metallic objects. The 6 GHz wave perceives the wall as a rough surface, causing a dispersion of the MPC track. Moreover, the waves travel through windows into the house, causing additional interactions with other walls or objects inside the room. These types of delay characteristics can be described as dispersed MPC track. Apart from the distinction between linear and dispersed MPC tracks, the wideband channel data reveals further unique characteristics, which can be related to specific properties of the scattering objects. For instance, the delay distances of the three parallel short MPC tracks from the MIMO channel 11 in the lower part of Fig. 8.4 can be related to three metallic bars at the back of a solar panel in Fig. 8.5.

8.2.2 Measurement-based Ray Tracing

The manual identification of scatterers described in Section 8.1 is time-consuming and limits the scatterer estimation results, due to the fact that higher order reflections cannot be considered to their full extent through visual inspection. Compared to the manual identification of scatterers, the so-called measurement-based ray tracing method [57] is far more effective and efficient. This method aims essentially at the reconstruction of the channel measurement run in a computer simulation and the subsequent comparison of the ray tracing results with measured MPCs. In order to reflect the real-world conditions of the propagation process, the ray tracing simulation has to include all relevant geometrical circumstances of the con-

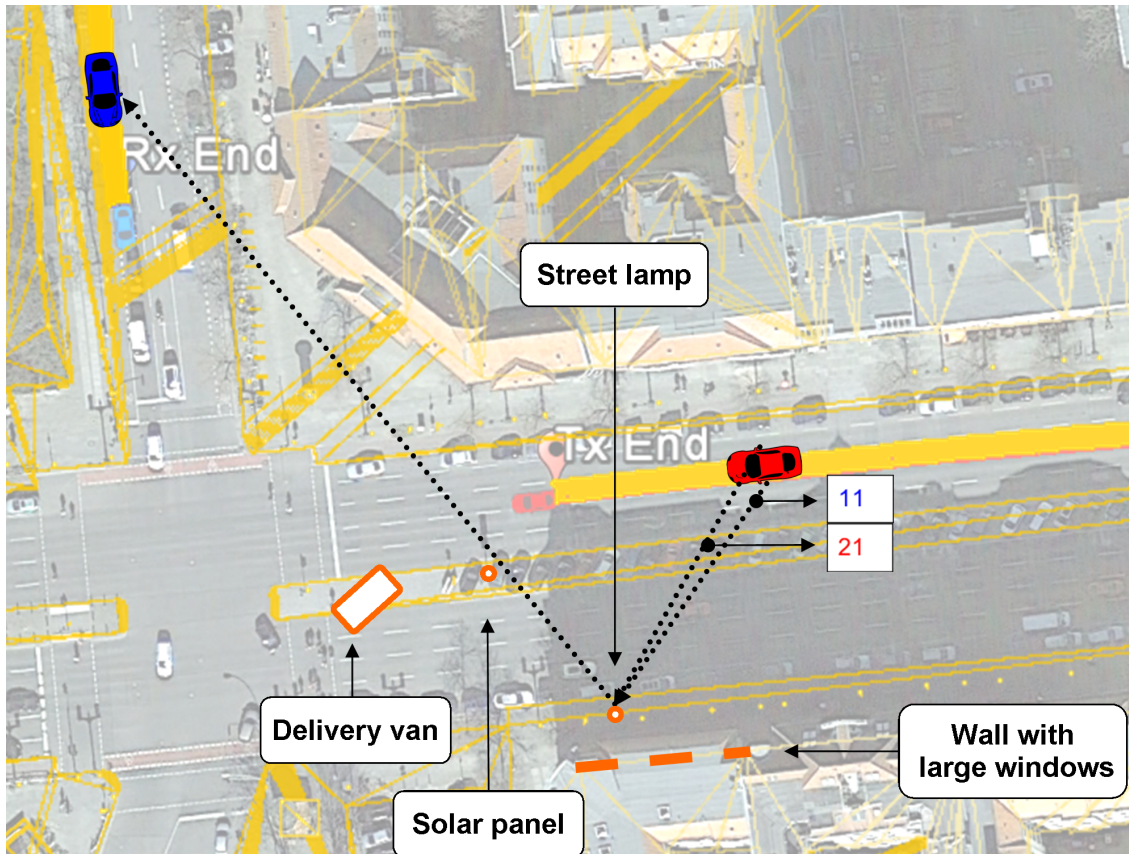


Figure 8.6: Overview of multipath geometry at intersection.

ducted measurement run. The reconstruction for our intersection geometry model is automatically derived from a data set provided by the city of Berlin, which includes the exact position of house walls, sidewalks and trees. In order to complete this geometrical model, all remaining relevant objects, for instance traffic signs or street lamps, have to be measured accurately with a laser distance meter on-site and included in the geometry model manually. The GNSS trajectories of the measurement vehicles are transformed from the geographic coordinate system (lat,lon) to the Cartesian coordinate system (x,y), where the origin of the Cartesian system is the crossing center. In order to accurately simulate the MIMO propagation channel, the positions of the simulated antennas are shifted accordingly.

In order to ensure the modeling accuracy and a high estimation reliability of the applied methods, we validate the consistency of the underlying data sets in two steps. First, we compare the delay of the LOS path with the Tx-Rx-distance estimates computed from the GNSS data. The difference between these distances after applied alignment measures is mostly below 1 m. In the second step, we superimpose a birds eye view picture of the real-world measurement run with the geometrical model including the transformed trajectories of the Tx and Rx vehicles. Fig. 8.6 shows that all elements of the geometrical model are well aligned with the real-world geometry. This can be observed when comparing the scattering locations (yellow dots) with the shadows of large objects, for instance the street lamp poles.

The ray tracing simulations are performed with the polarimetric 3D electromagnetic wave propagation simulator using the NVIDIA OptiX GPU ray tracing engine, an implementation developed at Fraunhofer HHI [58]. The association of MPC tracks and scatterer locations is based on a comparison of delay, Doppler, path angle estimates and the delay characteristic. It has been shown that the best approach for a dependable association is a so-called semi-automated reasoning method, which involves a limited number of automated suggestions and a subsequent human reasoning and decision. This means that for each measured MPC the automated algorithm part presents the human editor the closest ray tracing candidates in terms of the delay and Doppler distance. The geometrical positions of these scattering candidates are then compared with the estimated path angles (AOA and AOD). The lifetime of the measured MPC is compared with possible obstruction effects, due to the geometrical circumstances of the scattering candidates. Finally, the measured MPC and the simulated ray tracing candidates are compared in terms of their change of Doppler over time, which is directly related to the change of the path angles over time. Further details can be considered when comparing the delay characteristics and the properties of the possible scattering objects, as mentioned above. After each measured MPC was associated with a scattering object, concluding consistency checks can be applied. These verification tests involves a consistency check across the entire measurement run, across different MIMO channels and also across different measurement runs with similar Tx-Rx-coordinates.

The developed methods for a semi-automated localization of scatterers are successfully applied to data from intersection measurement runs, as the example above shows. The ultimate goal of the work described in Section 8.2.2 is a comprehensive analysis and the statistical description of relevant scatterers at urban intersections. The empirical result from this work will then be integrated in a GSCM of the V2V intersection scenario. Together with Lund University, approaches for an appropriate GSCM are initiated, in particular a geometrical power model of individual scatterers. In order to achieve the goal of a solid statistical foundation for the parametrization of a V2V intersection GSCM, more channel data from relevant intersections have to be analyzed (listed in Table 10.1). This work is not finalized yet and results are therefore not included in this thesis.

9 Evaluation of V2V Communications Performance

An ultimate goal of channel modeling is a communication performance evaluation based on a realistic representation of the channel. An alternative method for performance evaluation is the use of measured channel data, which implies a direct replay of the measurement run. This method can be used complementary to stochastic channel models and is beneficial for particularly demanding channel conditions not covered by the stochastic channel model. An advantage of communication performance evaluations based on replay channel data is the potential to investigate causes of packet losses in de facto occurring channels. A disadvantage of this type of communication performance evaluation is a narrow validity, if the available data set is not sufficiently large. In order to benchmark advanced receiver physical layer solutions, channel models or replay channel data can be used either in pure software simulations or in combination with channel emulator hardware. Section 9.2 and Chapter 10 introduce replay channel simulations using software only, with transmission simulations based on time-variant channel measurement data and an IEEE 802.11p physical layer transceiver implementation in MATLAB. The various communication models derived in these two chapters are beneficial for realistic simulations of basic V2V transceivers and were utilized in a commercial V2V plugin for a simulation platform that is used in the automotive industry for developments of advanced driver assistance systems.

9.1 Performance Evaluation based on Channel Emulator

An interesting application for industrial purposes is the performance evaluation of communication hardware implementations using a channel emulator (Fig. 9.1). This performance evaluation method involves the replay of a single measurement and the exact reproduction of particularly demanding channel properties. In order to ensure the fulfillment of these high demands on V2V communication reliability, a suitable testing method is required. A major event for testing V2V communication hardware is the annual ITS Plugtest hosted by the European Telecommunications Standards Institute (ETSI). The Heinrich Hertz Institute (HHI) took part in the

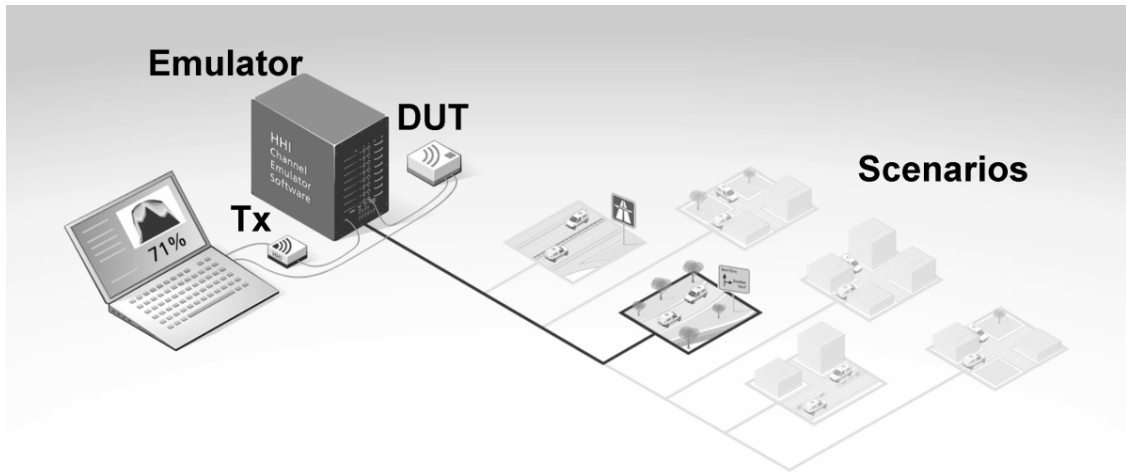


Figure 9.1: Performance evaluation of communication hardware using a channel emulator.

2015 event and provided two kinds of performance evaluation methods. The first evaluation is based on the ETSI ITS channel models, which are basically TDL models with 3-4 taps and corresponding power, delay and Doppler frequency values per tap. These models are defined for five communication scenarios, where the most demanding channel properties are found in the highway NLOS scenario. The outcome of this type of performance is a so-called waterfall curve, which expresses the response of the PDR to an increasing SNR or decreasing background noise.

The second kind of performance evaluation method conducted by HHI involves the replay of measured channel data. As mentioned earlier, a disadvantage of this method is a narrow validity. Nevertheless, the method permits a direct comparison of communication performance under challenging and de facto occurring channel circumstances. In addition, the potentials of implemented antenna diversity techniques can be evaluated based on entirely realistic MIMO channels. The results of this evaluation method for a highway oncoming traffic (HOT) measurement run are displayed in Fig. 9.2. It can be observed that the communication hardware from different vendors at the ETSI ITS Plugtest yield different average PDRs. These differences are slightly changed if receiver diversity techniques are applied, as the light-colored bars in Fig. 9.2 show.

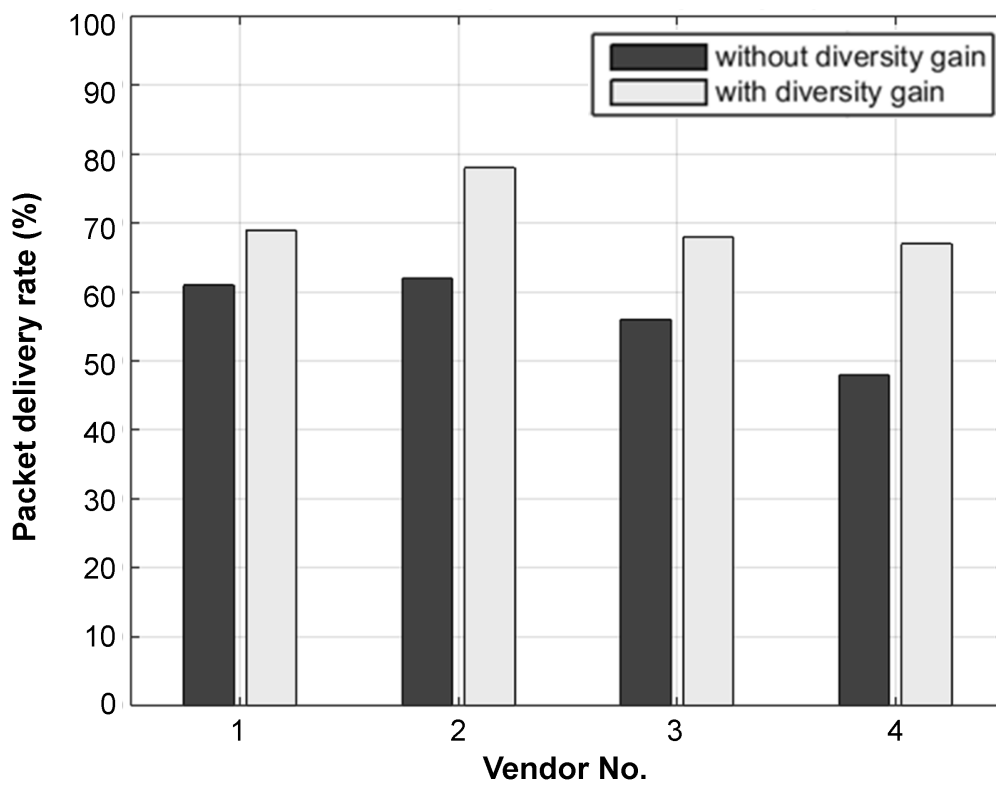


Figure 9.2: Communication performance of hardware implementations based on replay channel emulation.

9.2 Performance Evaluation based on Matlab Software

In this section, we introduce an IEEE 802.11p performance evaluation method based on realistic transmission simulations in Matlab. The vehicular propagation channel was measured beforehand using the wideband HHI Channel Sounder. We conducted channel sounder measurements of oncoming traffic at two different highway sections. The proposed method allows the execution of sample-based transmission simulations with full access to the receiver signal processing and all insights of wideband channel impulse responses. We compute mean PDRs for different packet sizes and discuss the effect of the time-variance in a vehicular propagation channel on the transmission success.

Several approaches are published for an 802.11p performance evaluation in vehicular communication scenarios, with packet error rate (PER) or PDR being the most common metrics. Some publications are based directly on measurements with 802.11p transceiver. Performance evaluations were conducted for an infrastructure-to-vehicle link in [55]. Studies in [56] showed that the major factors on the performance are the distance between transmitter and receiver and the availability of line-of-sight (LOS). Other publications follow a more theoretical approach. An analytical approach to retrieve the PDR is introduced in [54], with a channel model derived from Nakagami propagation model and with input variables: distance between transmitter and receiver, transmission power, transmission rate and vehicular traffic density. In [52], the communication distance is calculated using a two ray channel model. A third approach for a performance evaluation is the implementation of vehicular channel models. In [33] an 802.11p physical layer (PHY) performance evaluation was done based on TDL models from [34]. Simulation results are here expressed as PER over SNR for a highway (convoy) scenario. In this section, we introduce realistic sample-based transmission simulations with the potential to examine all possible causes of a packet loss.

9.2.1 IEEE 802.11p PHY in Matlab

We developed an object-oriented implementation of the IEEE 802.11p PHY in Matlab that involves all signal processing parts and is fully standard conform. Thereby, we can conduct extensive simulations and investigate in detail the behavior of the communication system on the physical layer level. Of special interest are the causes for packet reception failures. Reasons for a packet reception error can be found either in the radio channel or in the signal processing chain of the receiver physical layer. In fact, the reason for a packet reception error is the combination of both error sources, a demanding propagation channel in combination with a mismatched signal processing on the receiver side.

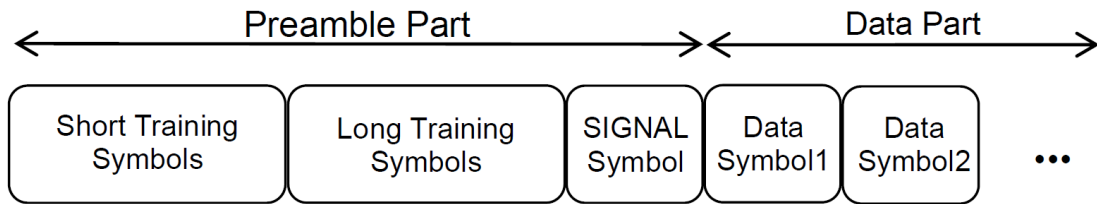


Figure 9.3: IEEE 802.11p Frame Structure.

For our simulation we use a QPSK modulation with coding rate $1/2$, resulting in a data rate of 6 Mbit/s. This data rate is comparatively low, but in return, reasonably robust and therefore a frequently chosen data rate (see [55]). In order to establish a realistic transmission simulation, a few more assumptions have to be made. We implemented a frequency offset of 1 ppm to account for transceivers with imperfect local oscillators. We choose a power class C (see page 31 in [22]) with a transmit power of 20 dBm. At both transmitter and receiver an antenna gain of 2 dBi is assumed. After the 802.11p signal passes the radio channel, white Gaussian noise is added to the signal with a power level of -94 dBm. The magnitude of the noise power is made up of the thermal noise power of -104 dBm for a bandwidth of 10 MHz and an estimated noise figure of 10 dB to account for the noise from the signal processing chain at the receiver. Finally, we choose a minimum SNR of 12 dB for the receiver to start detecting an OFDM frame, which yields a received signal sensitivity of -82 dBm. Since the signal power as indicator for reliable frame start detection is not sufficient, we implemented a frame-start detector that includes the detection of a sudden power rise and the detection of signal correlation, taking into account the structure of the IEEE 802.11p preamble. We checked the correct functionality of the frame-start detector and showed in numerous tests that the detection error rate at 12 dB SNR under NLOS conditions is below 10^{-3} . Downstream signal processing is according to the standard, including a Viterbi decoder with trellis termination and hard-decision.

The structure of an IEEE 802.11p packet frame can be roughly divided into a first preamble part, that lasts 40 μ s and includes two training symbols and a header symbol called SIGNAL, and a second data part that lasts between 88 μ s (for 50 Bytes) and 2016 μ s (for 1500 Bytes). The long training symbols in the second part of the preamble are used to estimate the current radio channel state. This information is required for channel equalization of the data part before the final decoding. IEEE 802.11 was originally developed for fixed wireless communication, where only slow changes of the channel states are expected. However, a particular attribute of vehicular communication is the time variance of the propagation channel, which means that the channel state can change over time. If the channel estimation becomes invalid during the duration of a frame reception, not all parts of the frame

can be equalized correctly and therefore the frame not decoded without errors.

9.2.2 Preprocessing of Channel Sounder Measurement Data

In order to use the collected channel sounder measurement data for sample-based 802.11p transmission simulations, some preprocessing steps have to be performed. The output of the HHI Channel Sounder is a time-variant channel impulse response (CIR) that includes a noise floor at around 135 dB attenuation. This noise floor has to be determined and discarded from the CIR before further processing. If this step was skipped, the noise peaks would be misinterpreted as many weak MPCs and if summed up, mislead to a substantial channel gain. In order to prevent this, we first set a noise threshold by adding a noise floor distance to the determined noise floor level. We empirically choose a noise floor distance of 6.5 dB. The CIR h is low-pass filtered and used to determine the beginning and the end of the signal part with MPCs. The beginning is set where the filtered h passes the noise threshold for the first time and the end is set where it passes the threshold for the last time. Finally, the identified noise part is set to zero. Fig. 9.4 illustrates the described operation.

During a channel sounder measurement, the radio channel is sampled with a snapshot rate according to the largest expected Doppler frequency. In the highway scenario, Doppler frequencies could rise up to 2500 Hz and therefore a snapshot period of 200 μ s was set. However, for sample-based transmission simulations the collected measurement data has to be interpolated in the time domain to a 10 MHz sample frequency, according to the IEEE 802.11p signal bandwidth. In order to save memory and speed up the processing, we interpolated the measurement data to a 1 MHz sample frequency, thus assuming that the radio channel stays constant during 1 μ s, and implemented the downstream processing accordingly. The interpolation was done with a one-dimensional FFT interpolation method. A prerequisite for this interpolation method is a periodic input signal. Therefore, a cosine roll-off windowing was applied to the CIRs in the direction of the time axis beforehand. The bandwidth limiting from the measured wideband channel of 1 GHz to the communication channel of 10 MHz (3 dB cutoff frequency) was carried out with a Kaiser window and a parameter value of 8.

9.2.3 Communication Models for Highway Oncoming Traffic Scenario

The highway oncoming traffic scenario is relevant for applications that use a store-carry scheme, where a message is transmitted to an oncoming vehicle, which stores and carries the message until a transmission is possible to a vehicle that drives in the same direction as the initial transmitter [19]. This scheme allows vehicles to

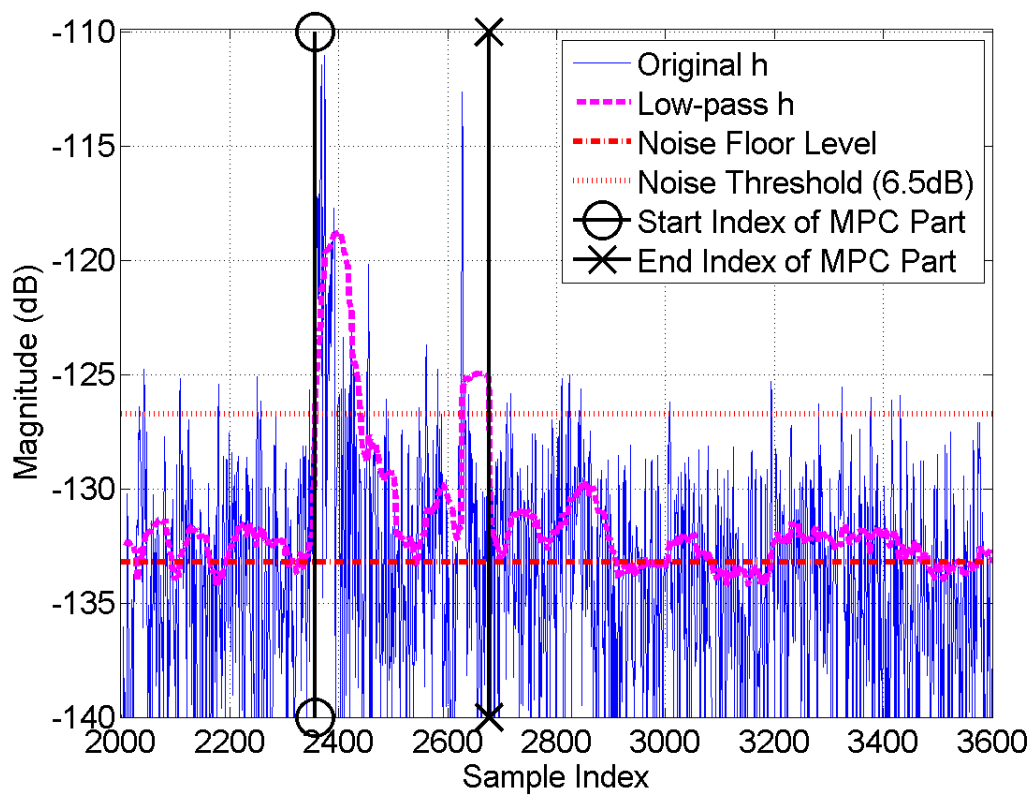


Figure 9.4: Identification of noise in a channel impulse response.

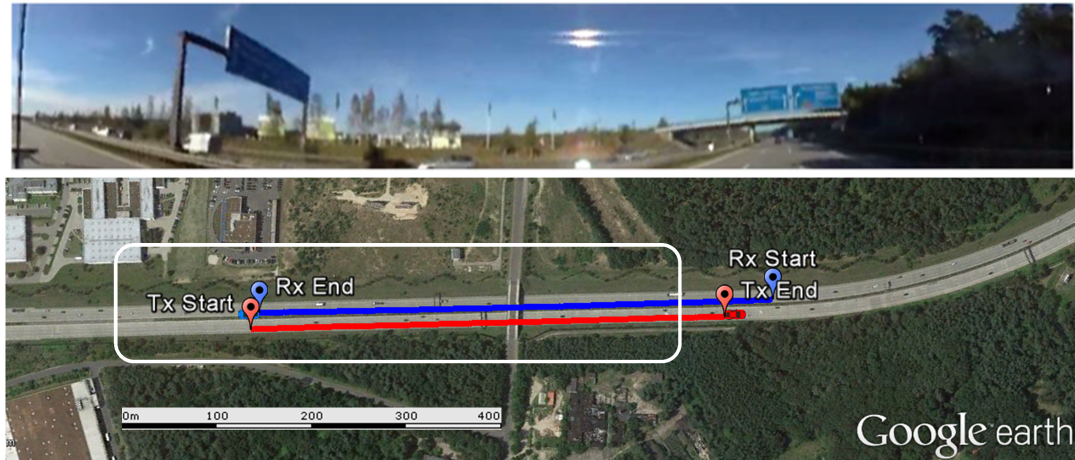


Figure 9.5: Typical highway A115 near Dreilinden/Berlin (upper part: 360° camera view during measurement, lower part: satellite view).

communicate with following vehicles, even if they are out of the wireless communication range. It is expected that for the highway oncoming traffic scenario, high relative velocity paired with a multipath channel can cause a demanding propagation channel for the 802.11p PHY. We conducted measurements at two different highway sections. The first section is a typical German highway called A115 east of Dreilinden/Berlin, with a speed limit of 120 km/h and a surrounding that is made up of dense vegetation and a few distant buildings. During measurements, the traffic density was fairly low. The measurement vehicles met with relative speeds of 200-240 km/h at various spots on the highway section, as indicated with a frame in the lower part of Fig. 9.5. The upper part of Fig. 9.5 shows a screenshot from the 360° video camera that was placed on the roof during measurements. The second highway section is the city highway A100 near Bundesplatz/Berlin, with a speed limit of 80 km/h and an urban surrounding. During measurement, the traffic was comparatively dense and included several trucks. The measurement vehicles met with relative speeds of 150-170 km/h at various spots on the highway section, as indicated with a frame in the lower part of Fig. 9.6. As in Fig. 9.5, the upper part shows a picture of the traffic situation during a measurement.

Both highway sections have 3 lanes in each direction and only a guardrail in the middle. Hence, a line-of-sight between two passing vehicles exists, if both vehicles drive on the left lane. During measurements, we used all lanes to achieve a realistic data set with larger diversity. We conducted a total of 11 measurements on each highway section, with a total recording time of 20 seconds per measurement. Each measurement was portioned into 20 parts, with a recording time of 100 ms for each



Figure 9.6: City highway A100 near Bundesplatz/Berlin (upper part: 360° camera view during measurement, lower part: satellite view).

part and a time interval of 1 s between these parts.

The PDR on the physical layer level is critical for every vehicular communication application. A packet reception failure on this layer level results inevitably in failure of adjacent higher OSI-layers. Here, we define a packet to be lost, if at least one bit is erroneous. As described above, a distinct attribute of the vehicular propagation channel is its highly time-variant behavior. In order to distinguish this influence from other influences of the propagation channel, we also conducted simulations with time-invariant channels. This was done by keeping the first channel sample of the CIR constant over the period of an 802.11p frame. In a time-invariant channel, the only relevant channel influences left are path loss and fading due to multipath propagation. We executed transmission simulations with several packet lengths between 50 bytes and 1500 bytes. The total number of simulated packet transmission per highway section varied between roughly 31,000 (1500 bytes) and 629,000 (50 bytes). The reason for this are the varying frame time durations (dependent on the number of transmitted bytes) that are "transmitted" over the constant time of the recorded radio channels. No remarkable differences could be observed between the four MIMO channels and so, the results of all MIMO channels were merged. The results of the transmission simulations can be found in Fig. 9.7 and in Fig. 9.8, where a negative distance was set in case of two approaching vehicles.

The first noticeable aspects in these diagrams are the remarkable valleys of the PDR curve at distances around 200 m. When comparing time-variant channels with time-invariant channels (marked with a "ti" in the legend of the diagrams), one can observe that the cause of this drop must lie within the time-variant behav-

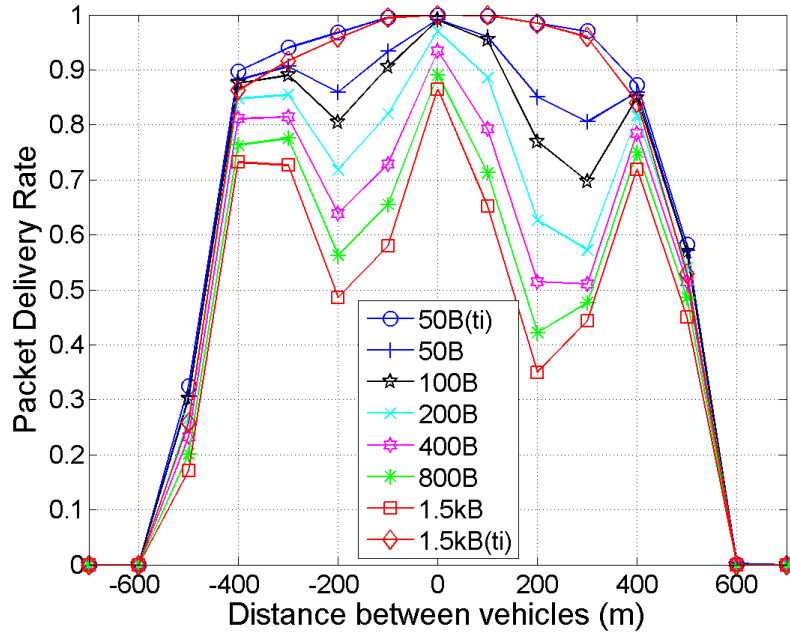


Figure 9.7: Transmission simulation results from a regular highway section (A115 - Dreilinden/Berlin).

ior of the propagation channel. The deviations between the two PDR graphs with time-invariant channels (50 bytes and 1500 bytes) are insignificant. In contrast, when comparing different packet sizes for time-variant channels, one can observe that the longer the frame duration, the steeper the valley. This can be explained by erroneous channel equalization. As mentioned earlier, the channel state is estimated at the beginning of a frame for subsequent channel equalization. The longer the frame transmission takes, the more likely this estimation becomes invalid and the channel equalization therefore insufficient for proper decoding.

At larger distances, the PDR of the highway section A115 Dreilinden (Fig. 9.7) rises again with a local maximum at around 400 m. In order to find out the reason for this behavior, we compared CIRs at distance around 200 m with CIRs at distance around 400 m. The apparent difference between these CIRs was the number of MPCs. Whereas most CIR at higher distances only indicated one path, most likely the LOS path, CIR at shorter distances exhibited multiple paths. Thus, the drop in the PDR graph at around 200 m is due to the time-variant behavior of the channel in combination with a multipath channel. Whereas the Doppler frequency of a single path can be corrected by the receiver signal processing, multiple paths with multiple Doppler frequencies lead to the so-called Doppler spread and a very challenging propagation channel.

Comparing the PDR graphs of the two highway sections, some similarities and

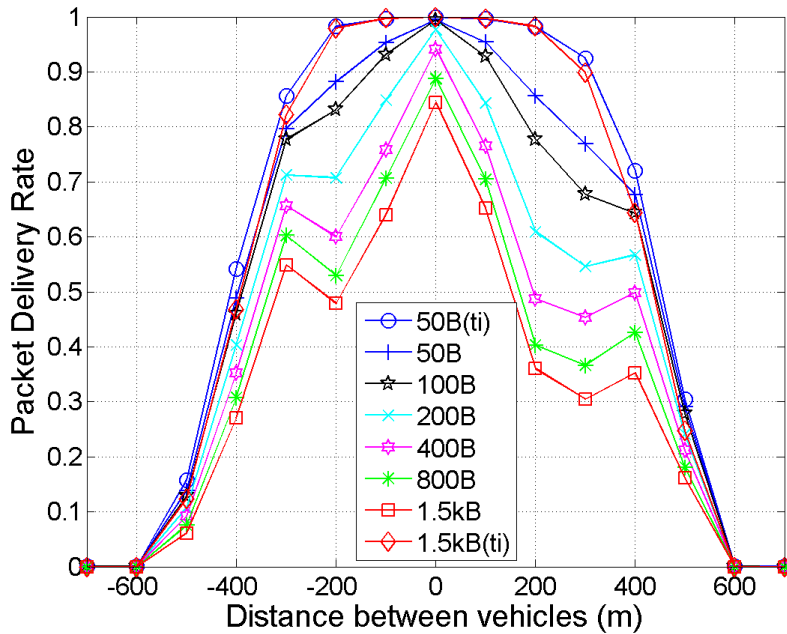


Figure 9.8: Transmission simulation results from a city highway section (A100 - Bundesplatz/Berlin).

some differences can be observed. In both graphs, the PDR dropped to zero at distances around 600 m. Apparently, the channel gain at these distances is too low for the 802.11p transceiver settings we choose. As described before, both graphs exhibit a drop at around 200 m. For both highway sections, these valleys are deeper at positive distances (vehicles driving away from each other) compared to valleys at negative distances (vehicles approaching each other). Unfortunately, no definite explanation for this behavior could be found. Some differences can be observed when comparing the graphs of the two measured highway sections. All PDR graphs around 400 m are noticeably higher in Fig. 9.7 compared to Fig. 9.8. In Fig. 9.7, even larger packet sizes achieve a high PDR. This can be explained with the lower traffic density during measurements for this highway section, therefore less shadowing and a higher probability of a LOS path. On the other hand in Fig. 9.8, the high traffic density during measurements combined with the slight bending of this highway section caused more shadowing, fewer LOS paths and a lower PDR at these distances. Although the average vehicle speed during measurements on the regular highway was approximately 30% higher, no severe effect on the PDR could be observed. Similarly, a clear effect of dense urban surrounding on the city highway and the resulting higher number of MPCs could not be identified. We computed the average PDR for different packet sizes for distances below 600 m and both highway sections (Table 9.1). These numbers can give a hint what packet

Table 9.1: Mean Packet Delivery Rates for HOT scenario.

Number of bytes	50	100	200	400	800	1500
Regular highway, low traffic density	82%	78%	72%	66%	61%	56%
City highway, high traffic density	71%	68%	60%	53%	48%	42%

sizes are suitable, when designing an application that transmits 802.11p messages under the described circumstances.

The results showed PDRs for different packet sizes and revealed the influence of the time-variant behavior of multipath channels on the packet reception success. This simulation framework opens the possibility for further statistical in-depth analysis of vehicular communication scenarios with demanding propagation channel and a performance evaluation of advanced signal processing methods.

10 V2V Communication Models at Urban Intersections

Future cross-traffic collision avoidance systems will depend on a reliable vehicle-to-vehicle communication link. Consequently, understanding inter-vehicle communication performance and the relationship to the corresponding intersection properties is vital for designing such a system. This chapter presents three intersection categories for non-line-of-sight communication performances, based on a large measurement data set. For each category, PDRs with respect to a two-dimensional distance are provided. These results can be used for network simulations or evaluation of collision avoidance systems.

Based on literature research, three categories for vehicular communication at urban intersections were developed and used to identify corresponding intersections on satellite images in the wider area of Berlin. It turned out that, after an evaluation of the simulation results, some exceptional intersections had to be included in Category 2. We defined the categories as follows:

Category 1 is characterized by an obstructing building between the two vehicles on collision course, without any large surfaces available for reflections from transmitter vehicle to receiver vehicle (see upper schematic in Fig. 10.5). This category also includes intersections where one of the vehicles drives in a street canyon, as long as there is no possibility for the waves to travel into the street canyon. According to [51], this category accounts for 4-12% of intersections with 4 legs. The Intersection-1 in [54] and the intersection called single building in [22] would be part of this category.

Category 2 is also characterized by a massive obstruction between the vehicles. Different to the previous category, both vehicles drive in street canyons allowing scattered waves to travel from transmitter to receiver (see middle schematic in Fig. 10.5). This category includes all intersections with buildings on four corners, which account for 70-90% of all 4 leg intersections according to [51]. Although it is shown in [59] that very large inter-building distances (streets widths) result in a higher received power and a higher reception rate, results in [54] show that the received power at smaller intersections can also be lower, depending on the scattering environment. Similarly, results in [60] showed a worse communication performance at a wide street intersection compared to a narrow intersection. Based on our analysis, no direct and clear relationship between intersection width and communication performance could be observed. Instead, we found 3 intersections which, accord-

ing to the definitions, should be in Category 1 but, due to the PDR results, were included in Category 2. These exceptional intersections require additional explanations, based on analyses of the corresponding wideband channel data and the intersections properties and are subject of the Results section.

Category 3 is best described with the absence of a massive object between the two vehicles (see lower schematic in Fig. 10.5). Instead, the optical LOS between the vehicles is obstructed by vegetation, parking vehicles, low walls and similar objects. This type of intersection is relevant for a collision avoidance system, due to the combination of an optical obstruction and permeable properties for electromagnetic waves. The influence of reflecting buildings or other scattering objects, as in Category 2, was found to be irrelevant for this category.

In total, we identified and measured 20 intersections. Each intersection was on average measured 8 times with distances to the crossing center of up to 200 m. The speed of the vehicles approaching the intersection varied between 30-60 km/h, depending on traffic circumstances. A continuous telephone link between the drivers ensured a collision course of the vehicles during measurement. A list of all measured intersections can be found in Table I, with coordinates of the crossing center, coordinates of the so called visibility vertex as depicted in Fig. 10.1 and the distance between these two points.

10.1 Transmission Simulation based on Channel Sounder Data

During measurement, a new channel impulse response was recorded every 716 μ s. However, for a sample-based transmission simulation, a higher channel update rate is required. We choose a sample frequency of 1 MHz and interpolated using a one-dimensional FFT interpolation. Then, the bandwidth of the channel was limited from the measured 1GHz bandwidth to the communication bandwidth of 10 MHz at 5.9 GHz, using a Kaiser window.

For realistic transmission simulation, we generated IEEE 802.11p communication frames (see Table 10.2 for details) and convoluted them with the preprocessed time-variant radio channels. The output of the transmission simulation is a PDR, where a packet was defined as delivered if all bits were decoded correctly. The time duration of one channel measurement run of 7 s and the transmitting time of 312 μ s for an IEEE 802.11p packet with 200 Bytes lead to more than 22,000 transmission simulation packets per measurement. This yields to a total number of 660 000 transmission simulations for Category 1, 720 000 transmissions for Category 2 and 1 800 000 transmission for Category 3.

Different from vehicular communication scenarios like oncoming traffic or convoy traffic, the inter-vehicle communication at street intersections is dependent on two

Table 10.1: Overview of investigated intersections.

Category	Name of Intersection	# of Meas	Crossing Center	Visibility Vertex	Distance (CC,VV)
1	Cauerstr/ Einsteinufer	12	52°31.152' 13°19.136'	52°31.142' 13°19.131'	19 m
1	Levetzowstr/ Hansa-Ufer	7	52°31.185' 13°20.257'	52°31.181' 13°20.240'	21 m
1	Rohrdamm/ Dihlmannstr	7	52°32.580' 13°15.696'	52°32.593' 13°15.709'	28 m
1	Nonnendamm- allee/Reisstr	7	52°32.188' 13°16.313'	52°32.183' 13°16.300'	17 m
2	Pestalozzistr/ Schlueterstr	2	52°30.455' 13°19.067'	52°30.451' 13°19.049'	22 m
2	Pestalozzistr/ Schlueterstr	2	52°30.456' 13°19.064'	52°30.463' 13°19.053'	18 m
2	Wilmersdorferstr/ Bismarckstr	5	52°30.697' 13°18.310'	52°30.704' 13°18.321'	18 m
2	Schlossstr/ Bismarckstr	3	52°30.664' 13°17.838'	52°30.676' 13°17.863'	36 m
2	Pestalozzistr/ Wielandstr	10	52°30.462' 13°18.963'	52°30.457' 13°18.953'	15 m
2	Augsburgerstr/ Rankestr	5	52°30.135' 13°20.008'	52°30.146' 13°20.004'	21 m
2	Luebeckerstr/ Turmstr	9	52°31.578' 13°20.721'	52°31.585' 13°20.731'	17 m
3	Fraunhoferstr/ Marchstr	11	52°30.872' 13°19.339'	52°30.880' 13°19.335'	16 m
3	Rohrdamm/ Dihlmannstr	7	52°32.581' 13°15.699'	52°32.579' 13°15.707'	10 m
3	Gierkezeile/ Zillestr	10	52°30.807' 13°18.187'	52°30.813' 13°18.195'	14 m
3	Fritschestr/ Pestalozzistr	9	52°30.477' 13°18.025'	52°30.472' 13°18.036'	17 m
3	Isoldestr/ Dreilindenstr	10	52°25.252' 13°11.321'	52°25.249' 13°11.328'	10 m
3	Wannseebadweg/ Kronprinzenweg	8	52°26.032' 13°11.363'	52°26.040' 13°11.365'	15 m
3	Augsburgerstr/ Rankestr	9	52°30.136' 13°20.010'	52°30.134' 13°20.034'	27 m
3	Levetzowstr/ Jagowstr	12	52°31.276' 13°20.021'	52°31.274' 13°20.005'	18 m
3	Turmstr/ Wilsnackerstr	14	52°31.583' 13°21.106'	52°31.577' 13°21.092'	19 m

Table 10.2: IEEE 802.11p transmission simulation parameters.

Packet size	200 Bytes
Data rate	6 Mbit/s
Transmit power	20 dBm
Antenna gain (each Tx and Rx)	2 dBi
Frequency offset	1 ppm
AWGN power	-94 dBm
Received signal sensitivity	-82 dBm

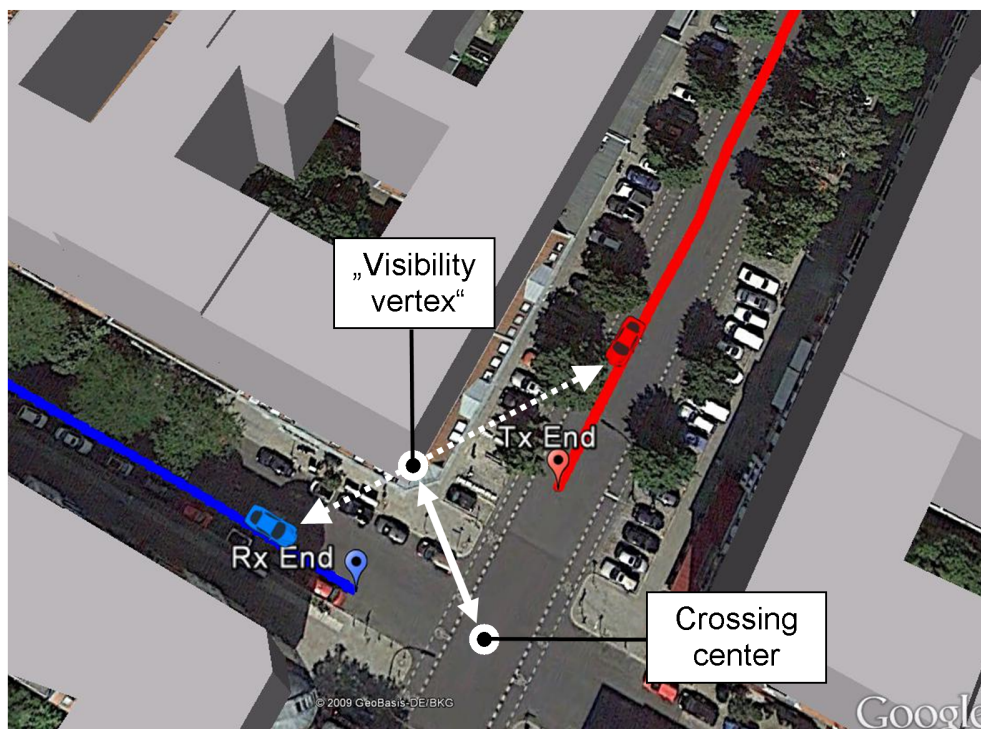


Figure 10.1: Vehicles on collision course (left) and transmission simulation results (right).

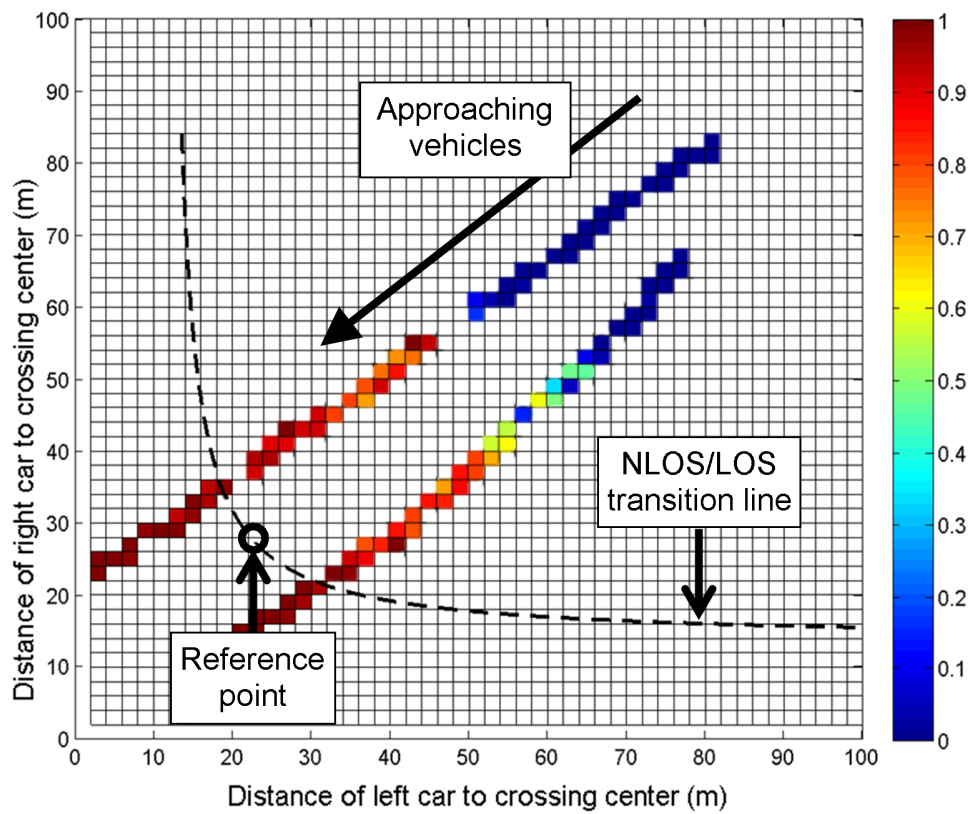


Figure 10.2: Vehicles on collision course (left) and transmission simulation results (right).

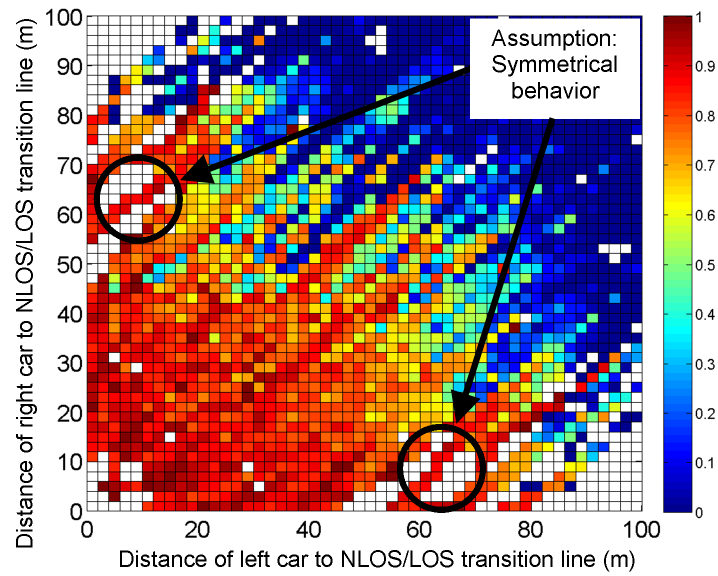


Figure 10.3: Superposition of Category 3 results (left) and a comparison between results and the estimated model (right).

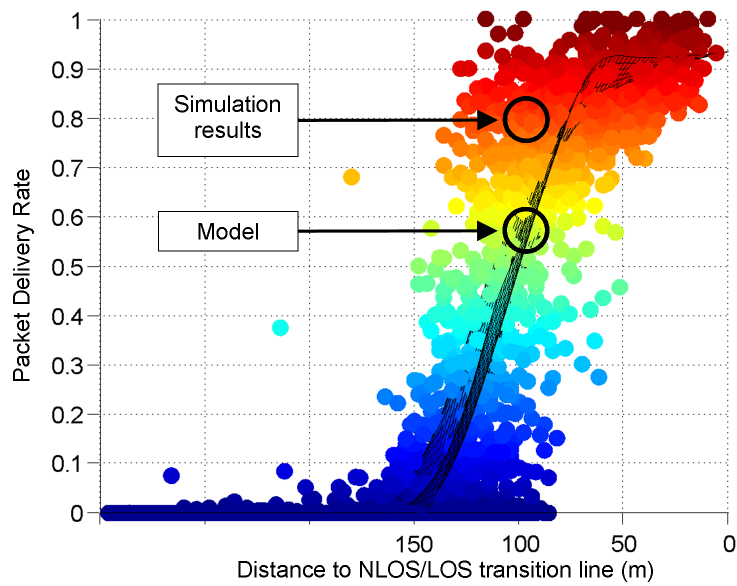


Figure 10.4: Superposition of Category 3 results (left) and a comparison between results and the estimated model (right).

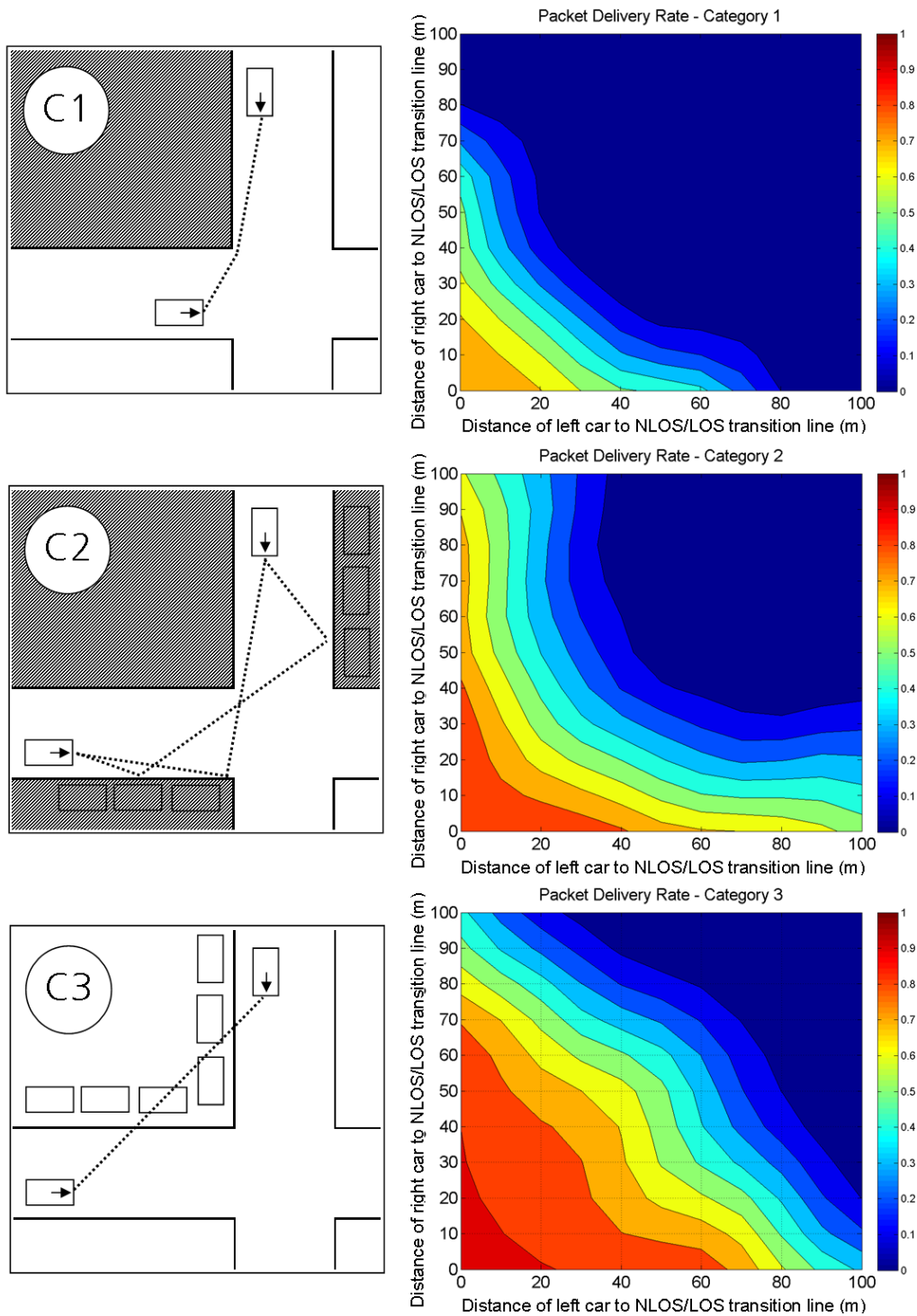


Figure 10.5: Schematics of intersection categories (left) and corresponding two-dimensional PDR model (right).

distances. Hence, our simulation results were evaluated with respect to a two-dimensional distance, as shown in Fig. 10.2. Here, each colored box represents the averaged PDR within a two-dimensional bin of 2 m x 2 m. This diagram shows the transmission simulation result of two measurements, with a low PDR (blue) at larger distances and a higher PDR (red) towards the end of the measurement. The dashed line represents the transition from NLOS condition to LOS condition. The shape of this transition line arises from the geometry of an intersection, while the position of the parabolic line depends on the size of the corresponding intersection. In fact, it depends on the distance between the crossing center and the visibility vertex, which is in this case the corner of the obstructing house. For measurements of Category 3, the visibility vertex was estimated using the recorded video sequences and Google StreetView™.

In our investigations, we focused on the NLOS case only, due to its relevance for cross-traffic assistance systems and the fact that results under LOS condition are virtually independent of location or category and always clearly above a PDR of 90%. One advantage of introducing a NLOS/LOS transition line is the ability to compare and merge street intersections with different sizes. In order to make all results within an intersection category comparable, we performed a coordinate transformation. This means a transfer of the reference point in Fig. 10.2 to the point of origin and a transformation of all other points from coordinates with distances to crossing center to coordinates with distances to LOS.

At this stage, the results were ready for a verification (or falsification) of the initially developed categories. To do so, we compared all intersection results and grouped similar results, disregarding the intended category. The criterion for this visual analysis was the location of the transition from blue to red, thus the change from no reception to packet reception. The analysis showed that, based only on communication performances at intersections under NLOS condition, three groups could be identified. These groups were used to derive corresponding PDR models, starting with a superposition of all simulation results within a category and an averaging of the PDR per two-dimensional bin. In order to obtain more supporting points, we filled empty bins with, if existent, its mirror-inverted counterpart result (see Fig. 10.3), which is based on the assumption that statistically, vehicular communication at intersection is symmetrical. Then, the PDR model was generated using a modified ridge estimator (a Matlab function called `gridfit`), where the bias is towards smoothness. An adequate smoothness parameter value was chosen, balancing between a questionable communication behavior (value too low) and an oversimplified model (value too high). We decided that a smoothness parameter value of 120 appears to be reasonable. Fig. 10.4 shows the 3-dimensional side-face of both the supporting points from the simulation results and the estimated model. Although substantial deviations of the PDR for a certain distance can be observed, the estimation result seems reasonable. The estimated results were finally averaged to bins of 10 m x 10 m width.

Intersection Schlosstr/Bismarckstr has no buildings on the north-western part, a cut building vertex on the north-eastern part and an east-west street with a very large width of almost 50 m. Due to the intersection geometry, transmitted waves from a vehicle in the northern leg of the intersection can travel far to a vehicle in the eastern leg, with single or double bounce reflections. This can be concluded from the course of the MPC. Summed up, the very wide street and the cut vertex result in the exceptional communication performance at this intersection. Intersection Augsburgstr/Rankestr has no building on the eastern part, but instead two metallic fences with vertical bars (vertical polarized antennas!) up to a height of around 2 m. In addition, the ground floor of the northern vertex is a shop-window and the western vertex has larger metallic elements. This corresponds to the CIRs, where a mixture of diffuse MPCs and a few specular MPCs could be observed. Intersection Luebeckerstr/Turmstr has no buildings on the southern part, but instead a park with numerous trees. However, the CIRs indicate that specular MPCs play a greater role, in particular a MPC with an excess distance of around 15 m. This can be explained with a comparatively large distance between a vehicle approaching from the west and the visibility vertex, a slight displacement of the 2 northern vertexes and many metallic elements at the north-eastern vertex (the opponent vehicle approaching from the north). The explanations for these 3 exceptional intersections exhibit the difficulty to derive general category definitions based on communication performances.

10.2 Communication Models

The final communication performance models are presented in Fig. 10.5. Since these results are shown with respect to the distance to LOS, an additional distance, or equivalent time, has to be added for a comparison of the so called time-to-collision. For our measurements, the median distance between the visibility vertex and the crossing center was found to be 18 m. This is in good accordance with 17.8 m distance from center to building vertex in the most prominent cluster (50% of all intersections), as reported in [51]. In case of both vehicles driving on collision course with the same speed, an additional (average) distance of about 13 m ($= 18\text{m}/\sqrt{2}$), equivalent to 1 s at a speed of 50 km/h can be estimated. This matches with the statement in [51] that for 90% of the intersections LOS is available 1 s before the crash. If one vehicle approaches the crossing center with a lower speed, the additional time reaches values above 1 s, due to an increased distance between NLOS/LOS transition and crossing center. The results show that the intersection characteristics of Category 1 allow NLOS communication at low distances only. Around 50% of the packets are delivered at distances of 20 m with both vehicles driving at the same speed, while there is no communication feasible at distances of 40 m. However, if one vehicle is near the intersection, communication availability

starts at around 70 m distance-to-LOS. Roadside units (RSU) installed at the intersection can support communication by re-broadcasting messages, However, it is likely that only selected intersections will be equipped, due to installation and maintenance costs.

The bended shape of the communication availability can also be observed in Category 2. With one vehicle close to the intersection, around 50% of the packets can be delivered up to distances of 100 m. This can be explained with scattering objects around the vehicle close to the center and scattered waves travelling into the street canyon of the distant vehicle. If both vehicles drive at equal speed, communication availability starts in Category 2 at around 50 m distance, while the PDR reaches 50% at around 30 m. The lack of a massive obstructing object in Category 3 leads to an almost parallel shape of the PDR levels and therefore to a PDR dependency of the cumulative distance of both vehicles. A conclusion from our results is that a combined distance to collision is reasonable only for Category 3. The bending of the PDR lines and the minor asymmetrical behavior can be attributed to the asymmetry of the collected data. In this category, communication availability starts at 70 m and rises to a PDR of 50% at distances of around 50 m. Also remarkable is the high PDR above 80% starting a distances of 30 m. The obtained PDR under LOS condition were averaged and resulted in 92% for Category 1, 98% for Category 2 and 95% for Category 3. The deviations between the categories could not be explained with the scattering environment and seem to be arbitrary; an average PDR of 95% for all categories could be reasonable. The PDR results are comparable to the reception rates reported in [59], where 4 types of intersections were measured: suburban, urban, urban wide and a worst case with buildings only at two corners. The reception rates in Fig. 6 in [59] show that at a distance of 60 m (equivalent to 47 m distance to LOS, if both vehicles approach with same speed) results within the intersection type urban and urban wide deviate between 55% and 95% reception rate, which is fairly higher compared to our results in Category 2. Intersection type suburban results at a distance-to-center of 60 m for both vehicles yield to reception rates between 10% and 20%, which is in good accordance to our Category 2 results. The exceptional results of intersection No. 9 in [59] fit well in our Category 3 results, both results show a PDR of less than 10% at 60 m distance to center and a PDR of around 70% at distances of 30 m. The investigations done on communication performances with vegetation between vehicles in [61] are only to some extent comparable to our Category 3 results, because here on of the vehicles was standing at a constant distance instead of driving on collision course. Distances of 30 m or 50 m resulted in PDR values between 80-100%, which is in accordance to our results.

This section presented PDR results for 3 intersection categories for non-line-of-sight communication performances. The derived models can be used to for network simulations and application evaluations. Considering the bended shapes of the PDR results, it becomes clear that a model based on a two-dimensional distance is more

comprehensive compared to a (cumulative) one-dimensional distance. The PDR results show that the communication performance mainly depends on the type of obstruction between the vehicles on collision course and availability of the large surfaces for reflections from transmitter to receiver. The validity of this categorization could be shown with the results from the transmission simulations. However, 3 out of 20 intersections exhibited unexpected communication performances. This shows that a categorization based on obvious intersection properties is not always valid. A closer look at the intersection properties including its vertexes and the corresponding wideband channel sounder data is needed.

11 V2V Communication in a Rural Overtaking Scenario

Reliable connectivity between vehicles is a requirement for efficient V2V warning systems, which is of particular relevance for collision avoidance systems during overtaking maneuvers on a rural roads. An example for the latter application could be a video-based overtaking assistant, where the overtaken vehicle transmits video-messages to the overtaking vehicle [62] [63] [64]. Alternatively, the vehicle to be overtaken exchanges CAMs with the vehicles driving in the opposite direction [65]. If vehicles in both directions are queueing, the vehicles leading these queues have the best opportunities to achieve LOS communication and should warn the vehicles following them. However, if the leading vehicle is not equipped with radio communication sensors, an apparent overtaking application alternative is simply the exchange of CAMs between the overtaking vehicle and the vehicles driving in the opposite direction. In each of the above mentioned application scenarios, the influence of large obstructing vehicles are most relevant since they block the view of the driver and possibly also radio waves.

There is related literature on V2V communication in rural environments. Work in [66] covers connectivity ranges based on measurements with an 802.11p transceiver, where one of the transceivers is kept stationary. The LOS obstruction in these measured rural environment scenarios is either due to a steep crest between the communicating vehicles or the vegetation in a curved road scenario. The power delay profile and the Doppler spectral density of an overtaking scenario is described in [67], where both Tx and Rx drive in the same direction with an obstructing truck between the measurement vehicles. The same setup is measured in [68], where the authors indicate power losses of 5-10 dB if the LOS is obstructed by a truck. Similar measurements are conducted by [69], where some of the antennas are also placed at different locations within the vehicle. Compared to the antenna mounted on the roof center, the inside-antennas yield to a gain of up to 20 dB for the obstructing truck scenario. To the knowledge of the author, no paper has been published on the propagation channel of a rural overtaking scenario with the communicating vehicles driving in opposite directions.

11.1 Measurement Setup and Environment

For this measurement campaign, we use an Audi Avant as a Tx vehicle and a Renault Scenic as Rx vehicle. Both vehicles are equipped with omnidirectional and vertically polarized antennas mounted on the roof at the left and right edges of the vehicle. In addition to the antennas mounted on the roof, we installed two vertically polarized antennas at different locations inside the receiver vehicle as shown in Fig. 4.5. The purpose of this experiment was to find out whether aftermarket transceivers with an in-cabin antenna serve their purpose and to evaluate which antenna location is more suitable in terms of a reliable connectivity.

In order to evaluate a worst case scenario, we searched for rural roads with a poor scattering environment. The rural road we selected is named Potsdamer Chaussee and located south of the village Seeburg near Berlin (N52.504, E13.123). Buildings of the close-by village are too distant for relevant scattering and the surrounding vegetation is expected to result in diffuse MPCs only. The selected road can be separated into two parts: a section with a straight road and a section with road bending of approximately 25° (see Fig. 11.1 and Fig. 11.6). We conducted measurement runs for these two kind of scenarios: a curved road scenario and a straight road scenario. In total we executed 7 runs with different obstructing large vehicles: 1 large goods vehicle, 2 coaches, 1 large caravan, 2 site vehicles of type Mercedes-Benz Actros 4146 and 1 van of type Volkswagen Type 2 (T3). The distance between the obstructing vehicle and the following measurement vehicle was in the range of 5-20 m. Depending on the traffic situation, the average speed of the measurement vehicles ranged between 60-100 km/h.

11.2 Curved road scenario

An overview of the curved road scenario is depicted in Fig. 11.1. The Rx vehicle is driving at an average speed of 82 km/h behind a site vehicle of type Mercedes Actros 4146 at distances of around 10-20 m, while the Tx vehicle is driving at an average speed of 83 km/h in the opposite direction. Visual inspection of multipath tracking results revealed that no significant specular MPCs could be observed, i.e. paths are either LOS or diffuse. Apparently, the path of the antenna mounted on the roof of the Rx vehicle (Rx1Out) bypasses or diffracts around the obstructing vehicle and establishes a specular path from both antennas of the Tx vehicle. In this measurement run, we observe that for distances between 450 m and 150 m the antennas mounted inside the vehicle yield to a higher channel gain¹, as can be seen in Fig. 11.2. In addition to this, the outside antennas experience a significant energy drop at distances around 300 m. Hence, we can conclude that antennas

¹Here, channel gain includes the antenna gains but not the cable loss

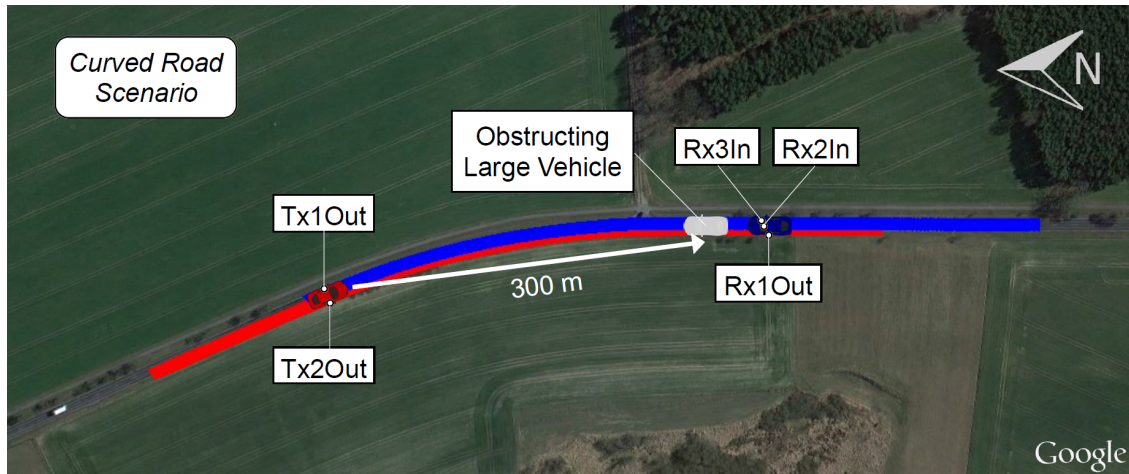


Figure 11.1: Overview of the measurement conducted on a curved road section.

mounted inside the vehicle would perform better with gains of up to 10 dB at most relevant distances in terms of a corresponding warning application .

Antennas mounted on the roof are probably in most V2V propagation environments beneficial compared to antennas inside the vehicle. However, if the radio channel is dominated by the LOS path and the ground-reflections, the inside-antennas might experience fewer ground-reflections and can overturn the advantage.

Although the channel sounder has a temporal resolution of 1 ns, multipath caused by two-ray ground-reflection with antenna heights of 1.5 m can only be resolved at distances below 15 m. For each measured time-variant channel of around 3 ms duration, we computed the Rician K-factor $K = 10 \log_{10}(P_s/P_r)$, where P_s is the power of the strongest path and P_r is the sum of the power of all paths except for the strongest path. The results in Fig. 11.3 indicate that the energy drop at a distance of 300 m is indeed due to the destructive ground-reflection. The antenna at the rear-mirror yields a progression similar to the roof antenna, yet with a smoother change of the K-factor and a less severe energy drop. The antenna mounted on the dashboard is apparently not affected by the ground-reflection and also has the highest channel gain.

Additional examples where inside-antennas should be favored are observed in two measurement runs conducted at this curved road section. As in the previously described run, the Rx vehicle is driving behind the obstructing vehicles - in this case a large truck and a large coach. Different to the previously described scenario, the driving direction of both measurement vehicles changed, i.e. the Tx vehicle is driving northbound at an average speed of 60 km/h (90 km/h in the second measurement) and Rx vehicle is driving southbound at an average speed of 65 km/h. Since the results of these two measurements are very alike, we computed

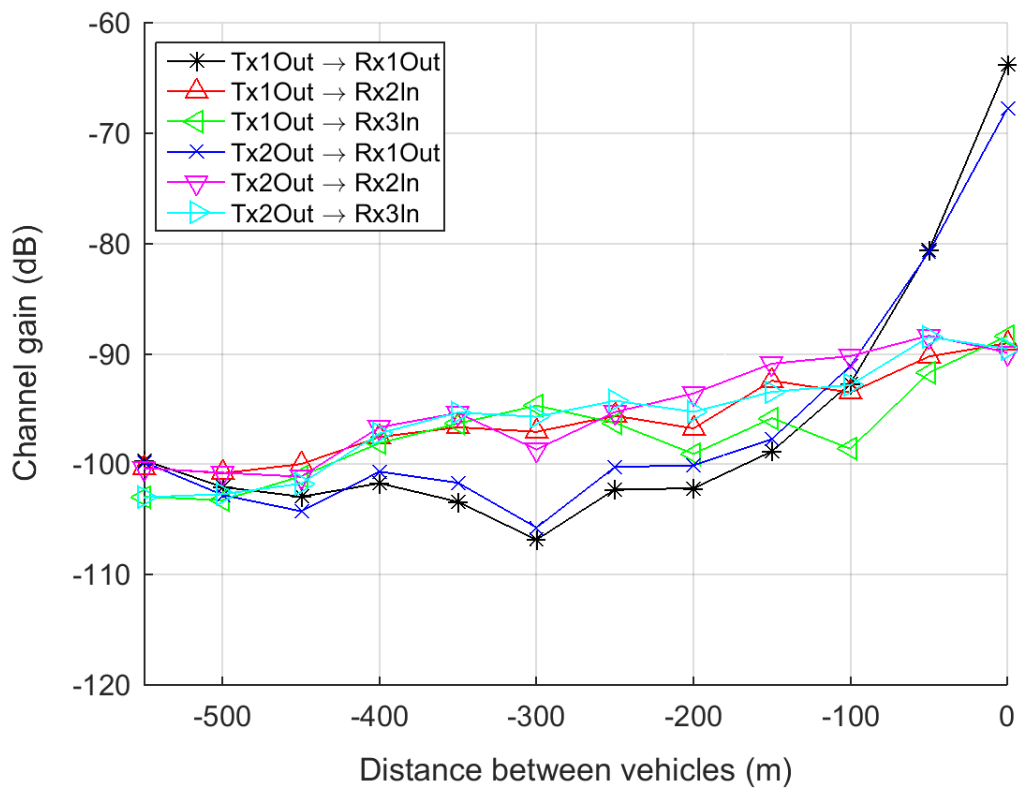


Figure 11.2: Channel gain of different antenna combinations on a curved road.

the average channel gain over distance of both measurements. As can be seen in Fig. 11.4, at distances of around 500 m the channel gain of all antennas is above -105 dB and reaches values of around -100 dB at distances of 350 m, with a slight gain of the inside-antennas. After a minor energy drop for all antennas at distances around 300 m, the differences between the antennas become apparent. At distances of 200-250 m, the channel gain of the antennas mounted inside the vehicle rise to values of around -90 dB, whereas the energy of the roof antenna stays at roughly the same level and then even falls again below -100 dB. One might assume that this effect is due to the transition from a right-curved road to a straight road and that a stronger obstruction of the Rx1Out antenna occurs because it is placed on the left hand side of the vehicle. Indeed, the starting point of the severe K-factor drop in Fig. 11.5 corresponds well to the position of the antennas in terms of left and right position: first the drop of the Rx1Out antenna mounted on the left edge of the roof starts at 250 m, then the drop of the Rx2In antenna mounted at the rear-mirror starts at 200 m and finally the drop of the Rx3In antenna mounted on the right hand side of the dashboard starts at 150 m. Moreover, we notice that the

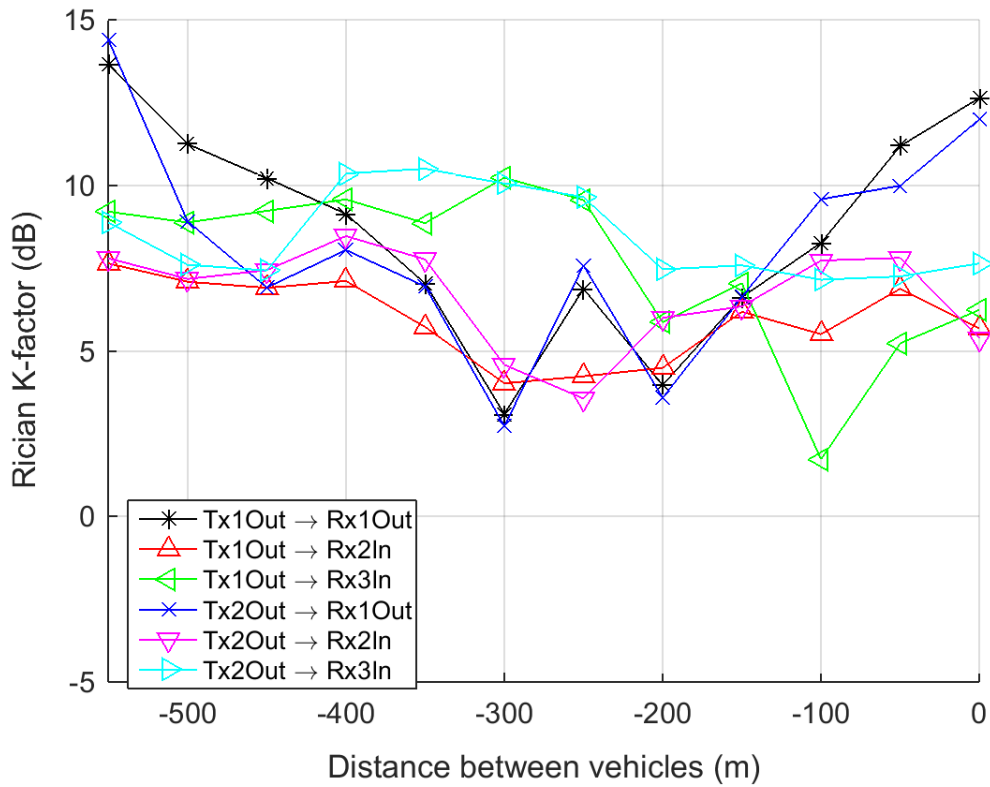


Figure 11.3: Rician K-factor for different antenna combinations on a curved road.

K-factor curves of the inside-antennas raise just before they decline, which might be due to the obstructing vehicle acting as a specular scatterer at the transition from a curved road to a straight road. This also explains the significant energy gain of the inside-antennas at a distance of 200-250 m. At a distance of 150 m, the higher channel gain of the Rx3In antenna is clearly due to its position on the right hand side, which can be concluded from the higher K-factor values at this distance. The obstruction is at its peak at distances of around 100 m, where the values of all antennas become more alike. We can conclude that the channel gain on the curved road section is often above -100 dB and that the inside-antennas usually yield a higher channel gain at distances relevant for an overtaking warning application.

11.3 Straight road scenario

Now, we study the scenario on a straight road section as depicted in Fig. 11.6. The obstructing vehicle drives at an average speed of 96 km/h and a distance of around 10 m in front of the Tx vehicle, while the Rx vehicle drives at an average

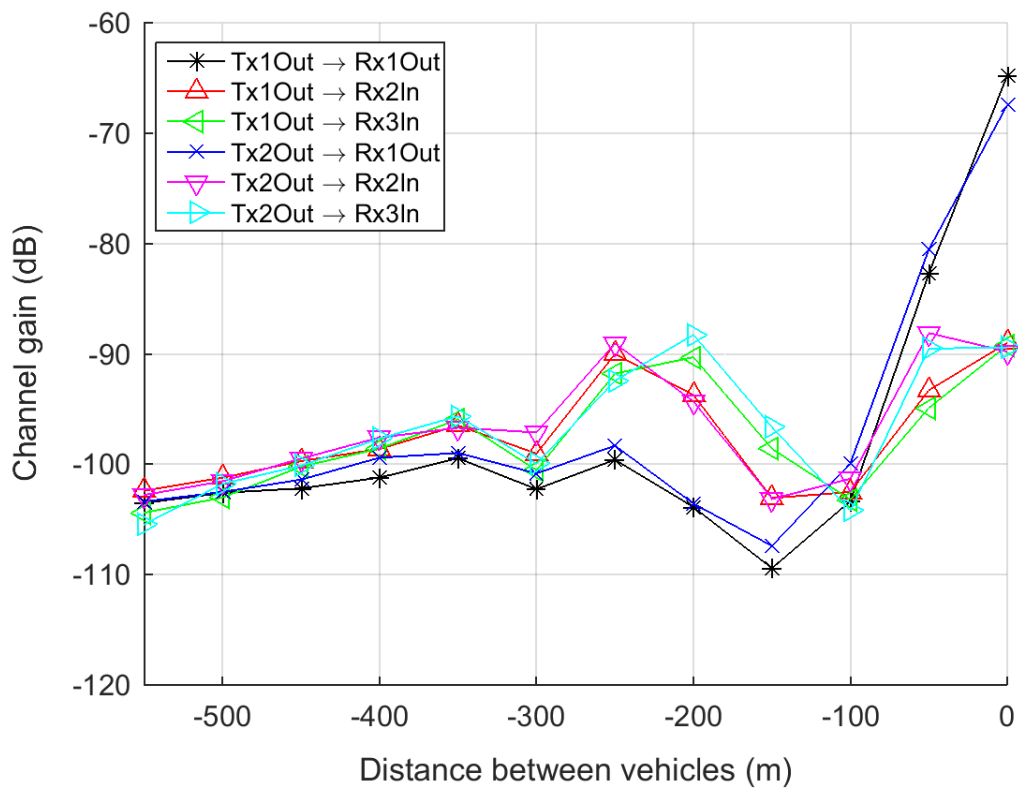


Figure 11.4: Averaged channel gain of two measurements on a curved road.

speed of 71 km/h in the opposite direction. Although the obstructing vehicle, a van of type Volkswagen Type 2 (T3) (see Fig. 11.7), is clearly not as large as the obstructing vehicle in the previously described results in Fig. 11.2, the obstruction effect in this case is far more severe. Results in Fig. 11.8 demonstrate that at a distance of 300 m the channel gain reaches values of around -110 dB only. On the other hand, we can observe that the antenna mounted on the left edge of the Tx provides a channel gain of nearly -100 dB at distances of 500 m. This is due to the fact that the measurement run starts as a curved road scenario and becomes a straight road scenario at a distance of around 300 m. This transition from LOS to obstructed LOS can be verified by corresponding K-factor curves and is the cause for the 10 dB channel gain drop of the Tx1Out antenna, as shown in Fig. 11.8. The large truck next to the van in Fig. 11.7 drove around 350 m ahead of the Rx vehicle and appears to have nearly no effect on the channel gain. We can conclude that a channel gain of -100 dB can only be reached at distances around 200 m and that inside-antennas usually experience a slightly higher channel gain.

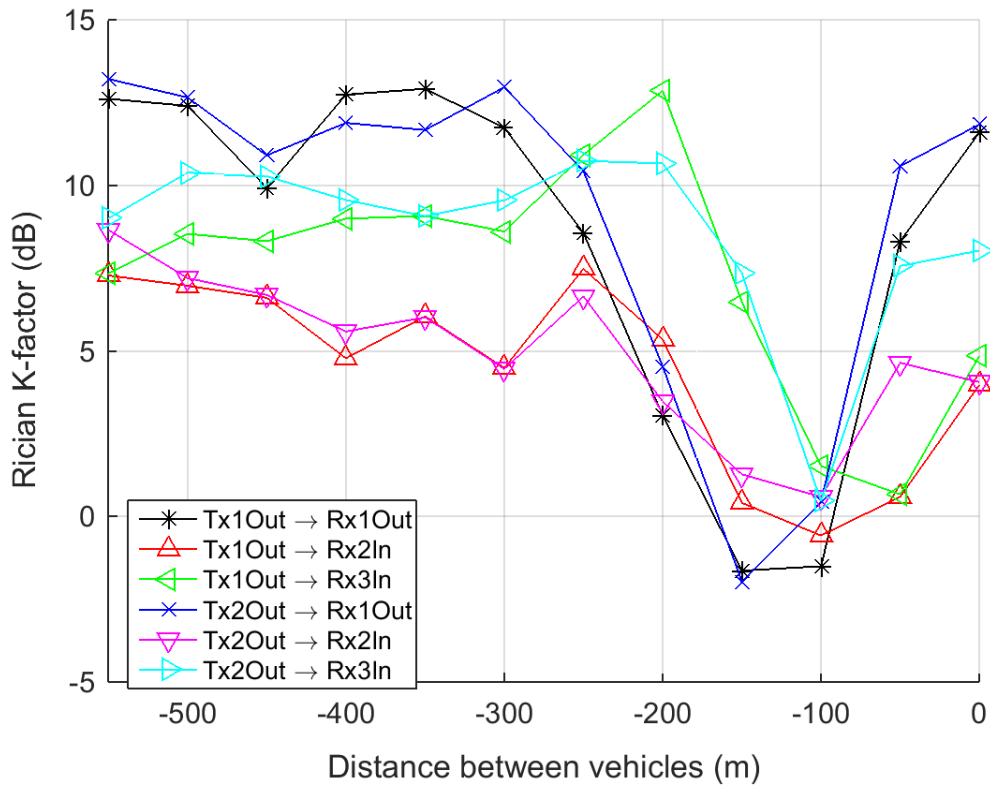


Figure 11.5: Averaged Rician K-factor of two measurements on a curved road.

Four measurement runs on this straight road section with different obstructing vehicles showed very similar channel gain progressions. In order to make a more general statement on achievable channel gains in this scenario, we computed the average of these runs, where the obstructing vehicle drove twice in front of the Tx vehicle and twice in front of the Rx vehicle. The obstructing vehicles were a large caravan, a large coach, a site vehicle of type Mercedes Actros 4146 and the Volkswagen Type 2 (T3) in Fig. 11.7. The distance between the obstructing vehicle and the following measurement vehicle is the range 5-15 m, whereas the average speed of the measurement vehicles ranges 70-95 km/h. As we clearly can observe in Fig. 11.10, the channel gain reaches a level of -100 dB not until a distance of 100 m. After the vehicles passed by each other, the channel gain differences can be explained with the fact that the antenna Rx1Out on the roof does not experience any obstruction, whereas the antenna Rx2In mounted at the rear-view mirror and even more the Rx3In antenna mounted on the dashboard (see Fig. 4.5) experience obstruction from various objects within the Rx vehicle.

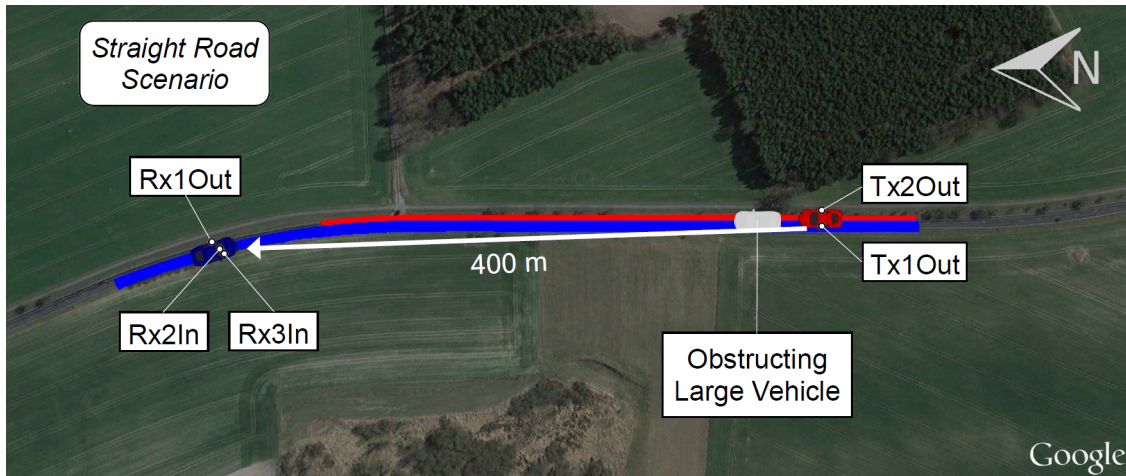


Figure 11.6: Overview of the measurement conducted on a straight road.



Figure 11.7: Video capture of the measurement conducted on a straight road.

11.4 Delay and Doppler spread

In order to examine the frequency and time dispersion of the measured channels, we extracted the RMS delay spread and the RMS Doppler spread for all 7 measurement runs and found that the delay spread is low with maximum values of around 20 ns. The only exception to this observation is the measurement run pictured in Fig. 11.7, where the delay spread is significantly higher than shown in Fig. 11.9. This can only be explained with MPCs from other present vehicles, e.g. the site vehicle behind the van in Fig. 11.7. The delay spread of the channel at antenna Tx1Out reaches its peak at a distance of 150 m, whereas for antenna Tx2Out the maximum value is found at a distance of 100 m. Also, it can be observed in Fig. 11.9 that the

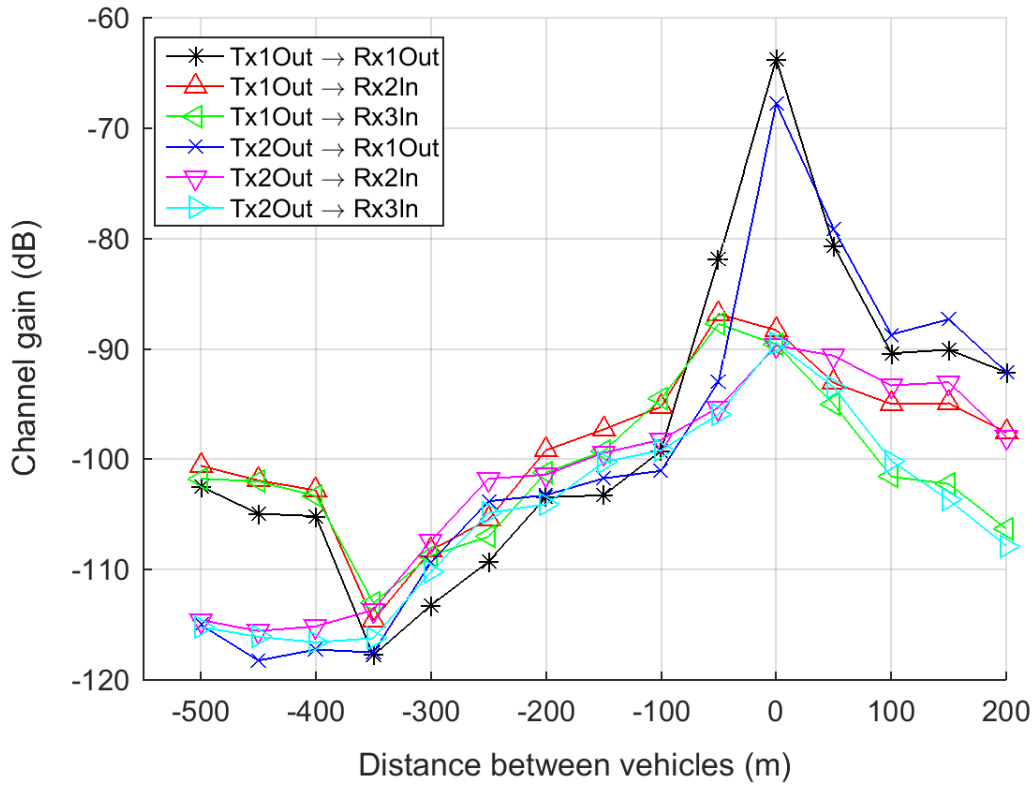


Figure 11.8: Channel gain of different antenna combinations on the straight road scenario depicted in Fig. 11.6 and 11.7.

delay spread values for inside-antennas are significantly higher compared to outside antennas with values up to 90 ns. The values of the RMS Doppler at distances above 400 m are usually below 100 Hz, while they can reach values of up to 400 Hz at smaller distances.

11.5 Potentials for V2V Communication

Before drawing conclusions, we give some preliminary considerations to an overtaking warning application. If we assume a reaction time of 2 s required for an overtaking warning system to work (see [65]) combined with a relative speed of 180 km/h of two vehicles heading in opposite directions, we can estimate a minimum distance of around 100 m for a V2V communication link. If we also take into account that the maximum transmit power of an IEEE 802.11p transmitter is 23 dBm (see page 31 in [8]) and that the minimum sensitivity is -82 dBm for a modulation and coding scheme of 6 Mbit/s with 10 MHz channel spacing (see page

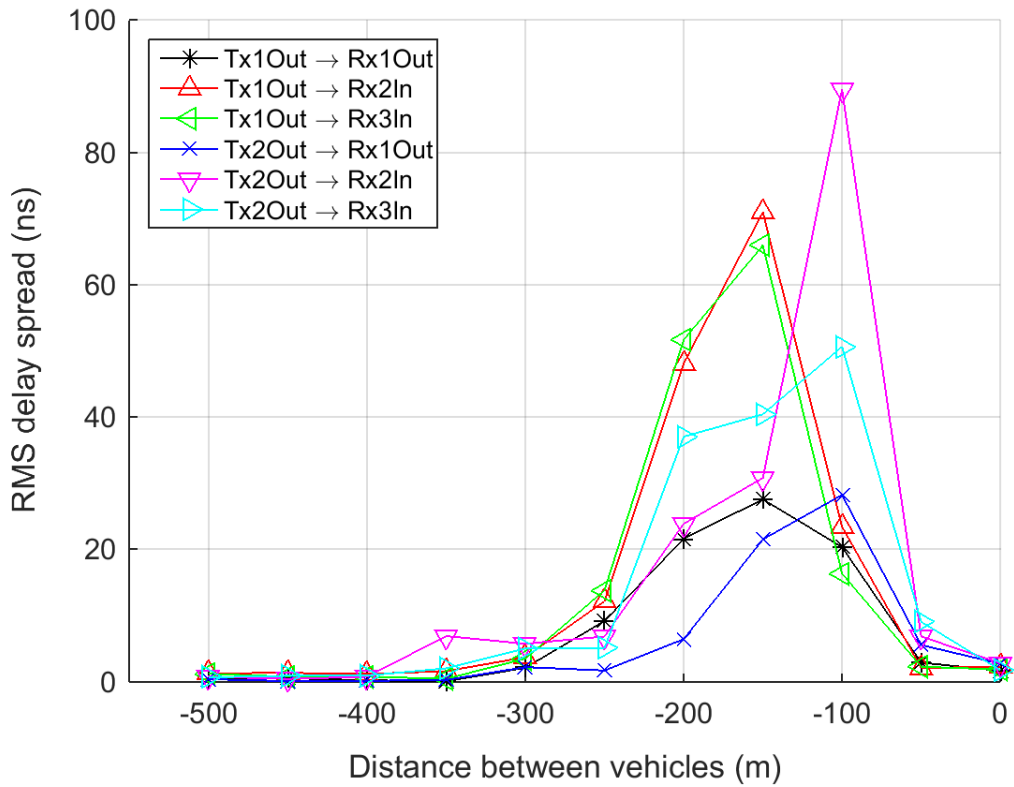


Figure 11.9: RMS delay spread of different antenna combinations on the straight road scenario as depicted in Fig. 11.6 and 11.7.

1612 in [9]), we can conclude that communication can only be established if the channel gain is above around -100 dB. Based on these considerations and the results presented in this chapter, we can draw several conclusions on the connectivity range for different measurements and antenna positions.

The channel gain of the inside-antennas in Fig. 11.2 achieve the required threshold of -100 dB at a distance of 400 m, whereas the antennas mounted on the roof cross this threshold only at a distance of 150 m. The gained distance of 250 m is remarkable and makes an advantage of antennas mounted within the vehicle apparent. Similarly, the results in Fig. 11.4 demonstrate that the channel gain of inside-antennas is above the threshold of -100 dB at a distances between 400 m and 150 m, whereas the channel gain of the roof antennas at these distances barely touches this threshold. We can conclude that for a curved road scenario in a rural environment, antennas mounted at the rear mirror or on the dashboard can significantly increase the connectivity distance and hence fulfill the prerequisites of a rural overtaking warning application.

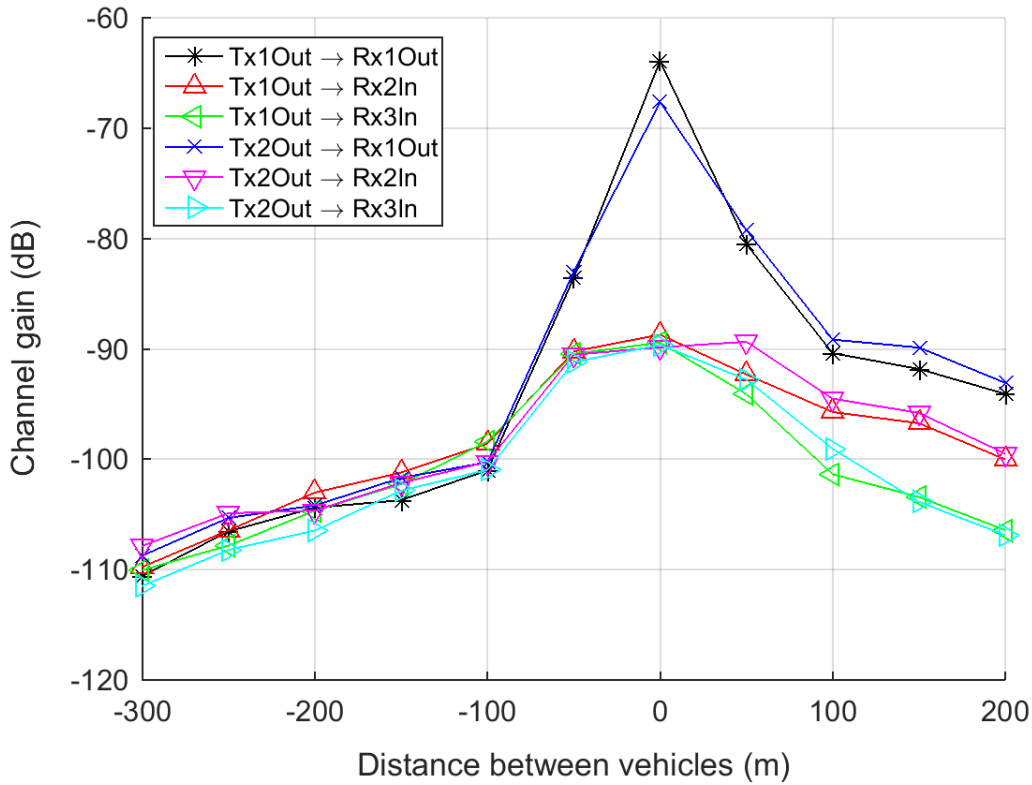


Figure 11.10: Averaged channel gain of four measurements on a straight road.

For the measurement results in Fig. 11.8, where the vehicles change from a curved road scenario to a straight road scenario, we could observe the advantage of antennas mounted on the edge of the roof. However, the channel gain of the Tx1Out antenna does not reach the threshold of -100 dB. We therefore conclude that in this case connectivity would start at distances between 200 m and 100 m. When looking at the averaged results from four straight road scenario measurements, we can clearly observe that on average and under the given measurement conditions none of the antenna position reaches the channel gain threshold of -100 dB at a distance of 150 m. This distance is very close to the previously estimated minimum distance of 100 m and leaves little time for a corresponding warning system.

Our results show that in the 6 GHz band only very little energy can be exchanged between obstructed vehicles on a straight road and that it is not recommended to count on the connectivity under the given conditions. This weakness should be significantly eased for frequencies of 700 MHz, as published work in [70] indicates. Also, different antenna positions can mitigate the obstruction effects. If the road is not perfectly straight, signals from antennas mounted on the edge of the roof can

diffract around the obstructing vehicle and increase the channel gain by around 10 dB. Furthermore, antennas mounted inside the vehicle appear to suffer less from the destructive effect of two-ray ground-reflections and can therefore increase the connectivity range significantly. Also noteworthy, in our experiments the inside-antennas never experience a disadvantage in terms of channel gain compared to antennas mounted on the roof. Therefore, aftermarket solutions with an antenna mounted on the rear-mirror or the dashboard can be serious complements to integrated installations.

12 Conclusions

This thesis illuminates various aspects of the V2V channel and the communication performance in several safety-related scenarios. It focusses on demanding propagation channels and highlights the potentials and limitations of V2V communication as vehicular sensor. Wide insights into the propagation process are revealed and statistical descriptions of channel aspects are established.

Wideband channel data is exceptionally beneficial for a detailed understanding of the propagation process in dynamic V2V channels. An efficient wideband MPC tracking algorithm with good tracking performance for short-term tracks is proposed and applied. In order to enable MPC tracking in longer measurement runs, two additional algorithms are developed. Based on these MPC estimation methods and 72 measurement runs in eight different vehicular communication scenarios, valuable information on the temporal behavior of individual MPCs is extracted and statistically characterized. Empirical distributions and stochastic models are presented for the number of, birth rate, lifetime, delay and Doppler of individual MPCs. A linear distance dependency of the Poisson parameter could be observed for the number of MPCs and the birth rate. For the Doppler distributions, three main groups are identified: the urban, the convoy and the oncoming traffic group. These findings are beneficial for a detailed modeling of the V2V propagation process, for instance in a V2V GSCM.

A geometry-based ray tracing method is developed and applied for a further parametrization of a V2V GSCM at urban intersections. This method enables detailed investigations on the geometrical propagation, including the localization of the relevant scattering objects. The wide measurement bandwidth reveals several unique MPC delay characteristics, for instance the distinction between linear and dispersed delay progressions, which can be used to improve the association of the MPC to the corresponding scattering object.

This thesis also introduces communication performance evaluation methods based on channel data, either using software or hardware equipment. V2V communication is essential for collision avoidance systems in NLOS scenarios. Work in this thesis show that the propagation channel at 5.9 GHz in the investigated rural overtaking scenario has limited potential for a timely V2V communication link. Differently, a reliable V2V communication link at urban intersection is possible at adequate distances. Dependent on the geometrical circumstances at the intersection, the communication performance can be categorized into three main V2V intersection NLOS communication models. The categorization shows that the communication

performance depends mainly on the presence of an obstructing building between the vehicles on collision course and on the availability of large surfaces for reflections from transmitter to receiver.

Future work in this research field could start with the application of the developed geometry-based ray tracing method on additional relevant communication scenarios, in order to achieve a complete parametrization of the V2V GSCM. A systematical analysis of more V2V channel data will reveal further insights into the V2V propagation process and the corresponding scattering objects. For a better estimation of the location of scattering objects, wideband channel data with direction-resolved MPCs would be beneficial.

The ultimate V2V communication system will be heterogeneous and operate at different frequencies, dependent on the particular application and communication scenario. For instance, a collision avoidance system for the rural overtaking scenario described in Chapter 11 could operate at frequencies below 1 GHz, while vehicles driving autonomously as a group on a highway could operate at frequencies above 10 GHz. Hence, V2V channel measurements and detailed investigations should be extended to other frequencies and additional scenarios, in order to initiate work towards the desired high dependability of a future V2V communication system.

Bibliography

- [1] Motorola. A legacy of innovation: Timeline of motorola history since 1928.
- [2] Bundesministerium fuer Verkehr und digitale Infrastruktur. *Verkehr in Zahlen 2015/2016*.
- [3] R. Johansson. Vision Zero—implementing a policy for traffic safety. *Safety Science*, 47(6):826–831, 2009.
- [4] World Health Organization et al. *WHO global status report on road safety 2013: supporting a decade of action*. World Health Organization, 2013.
- [5] T. Toroyan. Global status report on road safety. *Injury prevention*, 15(4):286–286, 2009.
- [6] TS ETSI. 102 637-2, Intelligent Transport Systems (ITS); vehicular communications; basic set of applications; part 2: Specification of co-operative awareness basic service. *ETSI, Sophia Antipolis Cedex, France*, 2010.
- [7] C. Bettisworth, M. Burt, A. Chachich, R. Harrington, J. Hassol, A. Kim, K. Lamoureux, et al. Status of the dedicated short-range communications technology and applications: Report to congress. Technical report, 2015.
- [8] IEEE Standard for Information technology— Local and metropolitan area networks— Specific requirements— Part 11: Wireless LAN Medium Access Control (MAC) and Physical Layer (PHY) Specifications Amendment 6: Wireless Access in Vehicular Environments. *IEEE Std 802.11p-2010 (Amendment to IEEE Std 802.11-2007 as amended by IEEE Std 802.11k-2008, IEEE Std 802.11r-2008, IEEE Std 802.11y-2008, IEEE Std 802.11n-2009, and IEEE Std 802.11w-2009)*, pages 1–51, July 2010.
- [9] IEEE Standard for Information technology—Telecommunications and information exchange between systems local and metropolitan area networks—Specific requirements Part 11: Wireless LAN Medium Access Control (MAC) and Physical Layer (PHY) Specifications. *IEEE Std 802.11-2012 (Revision of IEEE Std 802.11-2007)*, pages 1–2793, March 2012.

- [10] A. Benzin. Design and implementation of channel tracking algorithms for vehicular communications and IEEE 802.11p modem hardware design. *Master's Thesis, TU Berlin*, 2014.
- [11] S. M. Alamouti. A simple transmit diversity technique for wireless communications. *IEEE Journal on Selected Areas in Communications*, 16(8):1451–1458, Oct 1998.
- [12] M. Steinbauer. A non-directional, directional and double-directional point-of-view. *Dissertation, Technische Universitaet Wien*, 2001.
- [13] A. F. Molisch. Wireless communications. *Chichester, West Sussex, UK: IEEE Press-Wiley*, 2005.
- [14] A. F. Molisch. Ultrawideband propagation channels-theory, measurement, and modeling. *IEEE Transactions on Vehicular Technology*, 54(5):1528–1545, Sept 2005.
- [15] Simulation of rayleigh-faded mobile-to-mobile communication channels. *IEEE Transactions on Communications*, 53(10):1773–1773, Oct 2005.
- [16] G. Calcev, D. Chizhik, B. Goransson, S. Howard, H. Huang, A. Kogiantis, A. F. Molisch, A. L. Moustakas, D. Reed, and H. Xu. A wideband spatial channel model for system-wide simulations. *IEEE Transactions on Vehicular Technology*, 56(2):389–403, March 2007.
- [17] O. Renaudin, V. M. Kolmonen, P. Vainikainen, and C. Oestges. Non-stationary narrowband MIMO inter-vehicle channel characterization in the 5-GHz band. *IEEE Transactions on Vehicular Technology*, 59(4):2007–2015, May 2010.
- [18] L. Bernado, T. Zemen, F. Tufvesson, A. F. Molisch, and C. F. Mecklenbräuker. Delay and Doppler spreads of nonstationary vehicular channels for safety-relevant scenarios. *IEEE Transactions on Vehicular Technology*, 63(1):82–93, Jan 2014.
- [19] P. Paschalidis, M. Wisotzki, A. Kortke, W. Keusgen, and M. Peter. A wideband channel sounder for car-to-car radio channel measurements at 5.7 GHz and results for an urban scenario. In *Vehicular Technology Conference, 2008. VTC 2008-Fall. IEEE 68th*, pages 1–5, Sept 2008.
- [20] P. Paschalidis. The development of a wideband multiple-input multiple-output (MIMO) channel sounder and the measurement of the vehicular channel. *Dissertation, Institut für Nachrichtentechnik der Technischen Universität Braunschweig*, 2014.

- [21] O. Renaudin, V. M. Kolmonen, P. Vainikainen, and C. Oestges. Wideband MIMO car-to-car radio channel measurements at 5.3 GHz. In *Vehicular Technology Conference, 2008. VTC 2008-Fall. IEEE 68th*, pages 1–5, Sept 2008.
- [22] J. Karedal, F. Tufvesson, T. Abbas, O. Klemp, A. Paier, L. Bernado, and A. F. Molisch. Radio channel measurements at street intersections for vehicle-to-vehicle safety applications. In *Vehicular Technology Conference (VTC 2010-Spring), 2010 IEEE 71st*, pages 1–5, May 2010.
- [23] A. Richter. Estimation of radio channel parameters: Models and algorithms. *Dissertation, Technische Universitaet Illmenau*, 2005.
- [24] M. Z. Win and R. A. Scholtz. On the energy capture of ultrawide bandwidth signals in dense multipath environments. *IEEE Communications Letters*, 2(9):245–247, Sept 1998.
- [25] R. He, O. Renaudin, V. M. Kolmonen, K. Haneda, Z. Zhong, B. Ai, and C. Oestges. A dynamic wideband directional channel model for vehicle-to-vehicle communications. *IEEE Transactions on Industrial Electronics*, 62(12):7870–7882, Dec 2015.
- [26] L. Reichardt, J. Pontes, C. Sturm, and T. Zwick. Simulation and evaluation of car-to-car communication channels in urban intersection scenarios. In *Vehicular Technology Conference (VTC 2010-Spring), 2010 IEEE 71st*, pages 1–5, May 2010.
- [27] K. Ito, N. Itoh, K. Sanda, and Y. Karasawa. A novel MIMO-stbc scheme for inter-vehicle communications at intersection. In *2006 IEEE 63rd Vehicular Technology Conference*, volume 6, pages 2937–2941, May 2006.
- [28] I. Sen and D. W. Matolak. Vehicle channel models for the 5-GHz band. *IEEE Transactions on Intelligent Transportation Systems*, 9(2):235–245, June 2008.
- [29] G. Acosta-Marum and M. A. Ingram. Six time- and frequency- selective empirical channel models for vehicular wireless LANs. *IEEE Vehicular Technology Magazine*, 2(4):4–11, Dec 2007.
- [30] C. X. Wang, X. Cheng, and D. I. Laurenson. Vehicle-to-vehicle channel modeling and measurements: recent advances and future challenges. *IEEE Communications Magazine*, 47(11):96–103, November 2009.
- [31] A. F. Molisch, F. Tufvesson, J. Karedal, and C. F. Mecklenbräuker. A survey on vehicle-to-vehicle propagation channels. *IEEE Wireless Communications*, 16(6):12–22, December 2009.

- [32] D. W. Matolak and Q. Wu. Channel models for V2V communications: A comparison of different approaches. In *Antennas and Propagation (EUCAP), Proceedings of the 5th European Conference on*, pages 2891–2895, April 2011.
- [33] J. Karedal, F. Tufvesson, N. Czink, A. Paier, C. Dumard, T. Zemen, C. F. Mecklenbräuker, and A. F. Molisch. A geometry-based stochastic MIMO model for vehicle-to-vehicle communications. *IEEE Transactions on Wireless Communications*, 8(7):3646–3657, July 2009.
- [34] A. Theodorakopoulos, P. Papaioannou, T. Abbas, and F. Tufvesson. A geometry based stochastic model for MIMO V2V channel simulation in cross-junction scenario. In *ITS Telecommunications (ITST), 2013 13th International Conference on*, pages 290–295, Nov 2013.
- [35] M. Gan, Z. Xu, C. F. Mecklenbrücker, and T. Zemen. Cluster lifetime characterization for vehicular communication channels. In *2015 9th European Conference on Antennas and Propagation (EuCAP)*, pages 1–5, May 2015.
- [36] Z. Xu, M. Gan, and T. Zemen. Cluster-based non-stationary vehicular channel model. In *2016 10th European Conference on Antennas and Propagation (EuCAP)*, pages 1–5, April 2016.
- [37] R. Roy and T. Kailath. Esprit-estimation of signal parameters via rotational invariance techniques. *IEEE Transactions on Acoustics, Speech, and Signal Processing*, 37(7):984–995, Jul 1989.
- [38] R. Schmidt. Multiple emitter location and signal parameter estimation. *IEEE Transactions on Antennas and Propagation*, 34(3):276–280, Mar 1986.
- [39] T. Santos, J. Karedal, P. Almers, F. Tufvesson, and A. F. Molisch. Scatterer detection by successive cancellation for UWB - method and experimental verification. In *Vehicular Technology Conference, 2008. VTC Spring 2008. IEEE*, pages 445–449, May 2008.
- [40] R. J. M. Cramer, R. A. Scholtz, and M. Z. Win. Evaluation of an ultra-wide-band propagation channel. *IEEE Transactions on Antennas and Propagation*, 50(5):561–570, May 2002.
- [41] K. Haneda and J. I. Takada. An application of SAGE algorithm for UWB propagation channel estimation. In *Ultra Wideband Systems and Technologies, 2003 IEEE Conference on*, pages 483–487, Nov 2003.
- [42] C. Falsi, D. Dardari, L. Mucchi, and M. Z. Win. Time of arrival estimation for UWB localizers in realistic environments. *EURASIP Journal on Applied Signal Processing*, 2006:152–152, 2006.

- [43] J. Kaiser and R. Schafer. On the use of the IO-sinh window for spectrum analysis. *IEEE Transactions on Acoustics, Speech, and Signal Processing*, 28(1):105–107, Feb 1980.
- [44] B. N. Vo and W. K. Ma. The Gaussian mixture probability hypothesis density filter. *IEEE Transactions on Signal Processing*, 54(11):4091–4104, Nov 2006.
- [45] J. Salmi, A. Richter, and V. Koivunen. Detection and tracking of MIMO propagation path parameters using state-space approach. *IEEE Transactions on Signal Processing*, 57(4):1538–1550, April 2009.
- [46] M. Zhu, J. Vieira, Y. Kuang, K. Astrom, A.F. Molisch, and F. Tufvesson. Tracking and positioning using phase information from estimated multi-path components. In *Communication Workshop (ICCW), 2015 IEEE International Conference on*, pages 712–717, June 2015.
- [47] B. H. Fleury, M. Tschudin, R. Heddergott, D. Dahlhaus, and K. Ingeman Pedersen. Channel parameter estimation in mobile radio environments using the SAGE algorithm. *IEEE Journal on Selected Areas in Communications*, 17(3):434–450, Mar 1999.
- [48] B. T. Vo, B. N. Vo, and A. Cantoni. Analytic implementations of the cardinalized probability hypothesis density filter. *IEEE Transactions on Signal Processing*, 55(7):3553–3567, July 2007.
- [49] N. Czink, C. Mecklenbräuker, and G. Del Galdo. A novel automatic cluster tracking algorithm. In *Personal, Indoor and Mobile Radio Communications, 2006 IEEE 17th International Symposium on*, pages 1–5, Sept 2006.
- [50] T. Abbas, L. Bernado, A. Thiel, C. Mecklenbräuker, and F. Tufvesson. Radio channel properties for vehicular communication: Merging lanes versus urban intersections. *IEEE Vehicular Technology Magazine*, 8(4):27–34, Dec 2013.
- [51] T. Mangel, F. Schweizer, T. Kosch, and H. Hartenstein. Vehicular safety communication at intersections: Buildings, non-line-of-sight and representative scenarios. In *Wireless On-Demand Network Systems and Services (WONS), 2011 Eighth International Conference on*, pages 35–41, Jan 2011.
- [52] T. Mangel, O. Klemp, and H. Hartenstein. A validated 5.9 GHz non-line-of-sight path-loss and fading model for inter-vehicle communication. In *ITS Telecommunications (ITST), 2011 11th International Conference on*, pages 75–80, Aug 2011.
- [53] E. Giordano, R. Frank, G. Pau, and M. Gerla. Corner: a realistic urban propagation model for vanet. In *Wireless On-demand Network Systems and*

- Services (WONS), 2010 Seventh International Conference on*, pages 57–60, Feb 2010.
- [54] T. Abbas, A. Thiel, T. Zemen, C. F. Mecklenbräuker, and F. Tufvesson. Validation of a non-line-of-sight path-loss model for V2V communications at street intersections. In *ITS Telecommunications (ITST), 2013 13th International Conference on*, pages 198–203, Nov 2013.
- [55] T. Abbas, J. Karedal, F. Tufvesson, A. Paier, L. Bernado, and A. F. Molisch. Directional analysis of vehicle-to-vehicle propagation channels. In *Vehicular Technology Conference (VTC Spring), 2011 IEEE 73rd*, pages 1–5, May 2011.
- [56] J. Nuckelt, T. Abbas, F. Tufvesson, C. Mecklenbräuker, L. Bernado, and T. Kurner. Comparison of ray tracing and channel-sounder measurements for vehicular communications. In *Vehicular Technology Conference (VTC Spring), 2013 IEEE 77th*, pages 1–5, June 2013.
- [57] J. Poutanen, F. Tufvesson, K. Haneda, V. M. Kolmonen, and P. Vainikainen. Multi-link MIMO channel modeling using geometry-based approach. *IEEE Transactions on Antennas and Propagation*, 60(2):587–596, Feb 2012.
- [58] R. Felbecker, L. Raschkowski, W. Keusgen, and M. Peter. Electromagnetic wave propagation in the millimeter wave band using the nvidia optix gpu ray tracing engine. In *2012 6th European Conference on Antennas and Propagation (EUCAP)*, pages 488–492, March 2012.
- [59] T. Mangel, M. Michl, O. Klemp, and H. Hartenstein. Real-world measurements of non-line-of-sight reception quality for 5.9 GHz IEEE 802.11p at intersections. In *Communication Technologies for Vehicles*, pages 189–202. Springer, 2011.
- [60] H. Schumacher, H. Tchouankem, J. Nuckelt, T. Kuerner, T. Zinchenko, A. Leschke, and L. Wolf. Vehicle-to-vehicle IEEE 802.11p performance measurements at urban intersections. In *2012 IEEE International Conference on Communications (ICC)*, pages 7131–7135, June 2012.
- [61] H. Tchouankem, T. Zinchenko, H. Schumacher, and L. Wolf. Effects of vegetation on vehicle-to-vehicle communication performance at intersections. In *Vehicular Technology Conference (VTC Fall), 2013 IEEE 78th*, pages 1–6, Sept 2013.
- [62] C. Olaverri-Monreal, P. Gomes, R. Fernandes, F. Vieira, and M. Ferreira. The see-through system: A vanet-enabled assistant for overtaking maneuvers. In *Intelligent Vehicles Symposium (IV), 2010 IEEE*, pages 123–128, June 2010.

- [63] A. Vinel, E. Belyaev, and Y. Koucheryavy. Using of beaconing for robust video transmission in overtaking assistance applications. In *Vehicular Technology Conference (VTC Fall), 2012 IEEE*. IEEE, 2012.
- [64] E. Belyaev, P. Molchanov, A. Vinel, and Y. Koucheryavy. The use of automotive radars in video-based overtaking assistance applications. *Intelligent Transportation Systems, IEEE Transactions on*, 14(3):1035–1042, 2013.
- [65] A. Böhm, M. Jonsson, and E. Uhlemann. Adaptive cooperative awareness messaging for enhanced overtaking assistance on rural roads. In *Vehicular Technology Conference (VTC Fall), 2011 IEEE*, pages 1–5, Sept 2011.
- [66] A. Böhm, K. Lidström, M. Jonsson, and T. Larsson. Evaluating CALM M5-based vehicle-to-vehicle communication in various road settings through field trials. In *Local Computer Networks (LCN), 2010 IEEE 35th Conference on*, pages 613–620. IEEE, 2010.
- [67] A. Paier, L. Bernado, J. Karedal, O. Klemp, and A. Kwoczek. Overview of vehicle-to-vehicle radio channel measurements for collision avoidance applications. In *Vehicular Technology Conference (VTC 2010-Spring), 2010 IEEE 71st*, pages 1–5, May 2010.
- [68] M. Segata, B. Bloessl, S. Joerer, C. Sommer, R. Lo Cigno, and F. Dressler. Short paper: Vehicle shadowing distribution depends on vehicle type: Results of an experimental study. In *2013 IEEE Vehicular Networking Conference*, pages 242–245, Dec 2013.
- [69] D. Vlastaras, T. Abbas, M. Nilsson, R. Whiton, M. Olbäck, and F. Tufvesson. Impact of a truck as an obstacle on vehicle-to-vehicle communications in rural and highway scenarios. In *Wireless Vehicular Communications (WiVeC), 2014 IEEE 6th International Symposium on*, pages 1–6, Sept 2014.
- [70] H. Fernandez, L. Rubio, V. M. Rodrigo-Pearrocha, and J. Reig. Path loss characterization for vehicular communications at 700 MHz and 5.9 GHz under LOS and NLOS conditions. *IEEE Antennas and Wireless Propagation Letters*, 13:931–934, 2014.